THESIS FOR THE DEGREE OF LICENTIATE OF ENGINEERING

Dual Atmosphere Corrosion of 15-15Ti Cladding Material by Molten Pb and JOG Phases

Doğaç TARI

Department of Chemistry and Chemical Engineering

CHALMERS UNIVERSITY OF TECHNOLOGY

Gothenburg, Sweden 2024

Dual Atmosphere Corrosion of 15-15Ti Cladding Material by Molten Pb and JOG Phases
Doğaç TARI

Technical Report No: 2024:14

Department of Chemistry and Chemical Engineering
Chalmers University of Technology
SE-412 96 Gothenburg
Sweden
Telephone: +046 (0)31-772 1000

Cover:

Left: Reaction capsule components before assembly. *Middle:* Blueprint of the reaction capsule. *Top Right:* Blueprint of a cross-section on a drilled area. *Center Right:* SEM image of a cladding breach at 900 °C. *Bottom Right:* SEM image of a cladding breach at 1000 °C.

Printed by Chalmers Digitaltryck
Gothenburg, Sweden 2024

Dual Atmosphere Corrosion of 15-15Ti Cladding Material by Molten Pb and JOG Phases

Doğaç TARI

Nuclear Chemistry

Department of Chemistry and Chemical Engineering

Chalmers University Of Technology

Abstract

High temperature corrosion of cladding materials is still an issue hindering the deployment of Pb-cooled Generation-IV reactors. The combined effects of Heavy Liquid Metal coolant (molten Pb or Pb-Bi eutectic) and interaction with simulated fission products (JOG phases) have not been investigated thoroughly. In this work, the focus is on the corrosion of 15-15Ti cladding tube. The system was composed of molten Pb on the outer side of the cladding tube; while on the inner side, the selected JOG phase was Cs_2MoO_4. A reaction capsule was modified for experimental studies. The design minimized the excess oxygen ingress, and made sure that JOG phases and molten Pb were not in initial direct contact. The flow of the coolant and irradiation was disregarded at this stage, while the chemistry of the cladding corrosion was the focus. A notch geometry was introduced to thin the cladding in certain locations, mimicking a pre-damage scenario and simulating a cladding breach accident scenario; creating a controlled interaction of the HLM coolant and the JOG phases. The capsule was tested between temperatures of 600 °C to 1000 °C. The corrosion process was investigated as: the corrosion on hosting tube, cladding material (inner and outer side), and the pre-thinned surfaces of the cladding material. A kinetic model was drawn up to define the thickness losses and predict the limits of the capsule. Regarding the molten Pb side, a severe delamination effect was identified as one of the main reasons for thickness losses, which eventually led to cladding breach around thinned areas at $\geq$900 °C. Beneath the delaminated layer, intergranular attack was observed mainly as Fe-Cr spinel scales. Even though the characteristics of the spinel changed with the temperature, intergranular oxidation was identified as the eventual starting point for the cladding breaches. Around the breached locations, the interaction of molten Pb and Cs_2MoO_4 was seen but characterization of this interaction requires further study, and a more specific analysis campaign. On the Cs_2MoO_4 side, similar spinel scales were observed, while their intensity was much lower, and delamination was seen as a local event.

Keywords: Generation-IV Reactors, Cladding, Molten Pb, Fission Products, Cesium Molybdate, High Temperature Corrosion.

List of Publications and Manuscripts

This thesis is based on following papers and manuscripts:

Paper I (Published)

Tarı, D., Retegan Vollmer, T., & Geers, C. (2024). Reaction Capsule Design for Interaction of Heavy Liquid Metal Coolant, Fuel Cladding, and Simulated JOG Phase at Accident Conditions. *Journal of Nuclear Engineering*, *5*(1), 57-73.

Contributions: Conceptualization, D.T., T.R.V. and C.G.; methodology, D.T., T.R.V. and C.G.; formal analysis, D.T. and C.G.; investigation, D.T.; writing—original draft preparation, D.T.; writing—review and editing, D.T., T.R.V. and C.G.; visualization, D.T.; supervision, T.R.V. and C.G.; funding acquisition, T.R.V.

Paper II (In Manuscript)

Title: Chemical Aspects of Dual Atmosphere Corrosion by Molten Pb and Cs_2MoO_4 on 15-15Ti Cladding Tube

Authors: Doğaç Tarı, Teodora Retegan Vollmer, Christine Geers.

Contributions: Conceptualization, D.T., T.R.V. and C.G.; methodology, D.T., T.R.V. and C.G.; formal analysis, D.T. and C.G.; investigation, D.T.; writing—original draft preparation, D.T.; writing—review and editing, D.T., T.R.V. and C.G.; visualization, D.T.; supervision, T.R.V. and C.G.; funding acquisition, T.R.V.

Table of Contents

Abbreviations, Definitions, and Symbols

°C	Degree Celsius
A	Pre-exponential Factor
AGR	Advanced gas-cooled reactors
ALFRED	The Advanced Lead Fast Reactor European Demonstrator
at.%	Atomic Percentage
BSE	Backscattered Electron
BWR	Boiling Water Reactors
C_O	Dissolved Oxygen Concentration in Liquid Metal
dpa	Displacement per atom
E_A	Activation Energy
EDX	Energy-Dispersive X-ray Spectroscopy
EU	European Union
G	Gibbs Free Energy
G°	Standard Gibbs Free Energy
GCR	Gas-cooled reactors
Gen-IV	Generation-IV
GFR	Gas-cooled fast reactors
HLM	Heavy Liquid Metal
IAEA	International Atomic Energy Agency
JOG	Joint Oxide Gain (or Joint Oxyde-Gaine)
K	Kelvin
k	Rate constant
kV	Kilovolt (in Electron Beam Accelerating Voltage)
LBEFR	Lead Bismuth Eutectic-cooled Fast Nuclear Reactors
LFR	Lead-cooled Fast Nuclear Reactors
LME	Liquid Metal Embrittlement
MOX	Mixed-Oxide (Uranium, Plutonium) Fuel
MSFR	Molten salt fast reactors

MYRRHA	Multi-purpose Hybrid Research Reactor for High-tech Applications
PHWR	Pressurized heavy water reactors
PWR	Pressurized Water Reactors
R	Gas constant
RBMK	High power channel-type reactors
SCWR	Supercritical water-cooled reactors
SEM	Scanning Electron Microscopy
SFR	Sodium-cooled fast reactors
VHTR	Very high temperature gas reactors
wt.%	Weight Percentage
XRD	X-ray Diffraction

1. Introduction

The relevance of nuclear power is steadily growing as the harmful effects of fossil fuels become more apparent, while the transition to renewables is falling behind as supply issues and efficiency cannot keep up with the increasing electricity demand. A leap in fission-based nuclear power is thus necessary [1]. Generation-IV (Gen-IV) nuclear reactors are expected to be this next step, not as a replacement to Generation-II or III reactors, but as a supporting fleet of new reactors. Among the proposed Gen-IV technologies, Lead-cooled Fast Reactors (LFRs) are offering higher efficiency and safer operation, while enabling new features [2, 3]. The fast neutron spectrum allows the usage of recycled fuel, significantly increased uranium utilization, and overall improvements in nuclear waste management solutions [1]. Nuclear power is already an efficient electricity production method that can supply on-demand energy, independent of weather, sun-hours coverage or season. A new generation of reactors can help nuclear power become even more sustainable.

The work on Gen-IV reactors has been steadily growing in the last decades. In particular, ALFRED and MYRRHA reactors have gained attention in the European Union (EU) [4]. Both reactors are planned to be technological demonstrators initially and realize the technologies' full potential in later iterations [5]. They are cooled by different Heavy Liquid Metal (HLM) coolants; ALFRED with Pb, and MYRRHA with Lead-Bismuth Eutectic (LBE).

Currently, the corrosion of structural and claddings materials by HLM coolants remains an issue [6]. In addition, some of the phenomena related to the reactor core safety are not fully explained yet. Studies focusing on the corrosion phenomenon on cladding material and a possible cladding breach scenario is needed, especially at high burn-up and accident conditions [5, 7]. Current studies give a good understanding of molten Pb corrosion for operational conditions [8, 9]. However, the experimental work at elevated temperatures (>500 °C) has been insufficiently studied or even lacking. In addition, not enough focus has been given to the inner side of the cladding tube. For ALFRED and MYRRHA, the cladding of choice was 15-15Ti stainless steel tube [4]. In terms of corrosion, the cladding tubes are exposed to the fuel (from inner side) and coolant (from outer side), and cladding breach scenarios suggest that corrosion of both sides should be investigated simultaneously.

On the outer side of the cladding tube, the respective coolants of the reactors are the corrosive species. On the inner side; both reactor designs foresee Mixed-Oxide Fuel (U, Pu - Oxide or MOX) as the fuel choice, with high Pu enrichment (up to 25%). However, high burn-up situations dictate that accumulated fission products are the relevant corrosive species, also known as JOG phases [10, 11]. The accumulation of JOG phases have a complicated chemistry due to the high disparity of elements present and the variable oxygen potential in the fuel pellet [12]. Due to the extremely high temperature gradient of the fuel pellets in fast reactor operations, lighter fission products like Cs, Mo, I, Te tend to travel to the outer rim of the fuel pellets and eventually accumulate between the fuel pellet and cladding; while the heavier phases concentrate towards the center of the pellet. These JOG phases have been identified as oxidizing species. While some work has been reported on the corrosive properties of these fission products [13-16], literature is lacking studies on the dual environment corrosion: simultaneous impact of HLM and JOG phases.

The hazardous nature of fission product release from reactor core is already well known [17]. During reactor operation, an extreme event like a cladding breach can cause the JOG phases to leak into the reactor coolant system. Therefore, for reactor safety, it is crucial to have a deep understanding of cladding corrosion or any other event which can lead to a breach big enough to allow a release of JOG. This study is omitting irradiation effects due to the extremely high costs of an irradiation rig and lack of research reactors with appropriate neutron flux; also, assuming an elevated temperature condition and a high burn-up situation. A reaction capsule was built to investigate dual environment corrosion. 600 °C was considered as the lowest relevant temperature, while 15-15Ti stainless steel tube was exposed to molten Pb from the outer side and Cs_2MoO_4 from the inner side, which was chosen as the relevant JOG phase.

2. Background

2.1. Generation IV Reactor Systems

Gen-IV nuclear reactor systems are expected to be the next leap in fission-based nuclear power. While there are different systems proposed, the goal is similar; building a new fleet of reactors that are more efficient, environmentally friendlier, and more sustainable than their predecessors. Gen-IV systems do not aim to *replace* other systems (Gen II and III) initially; but rather they are designed to support these systems, consequently enabling the transition to greener electricity production. A comparison between these different generations of commercial nuclear reactors can be seen Table 1.

Table 1: Comparison between different generations of reactors, where the parameters for Gen-IV are highly variables between different proposed designs [2, 18].

Reactor Type	Generation	Fuel	Coolant	Temperature (°C)	Neutron Spectrum
Gas-cooled reactors (GCR)	I	Natural UO_2	CO_2	250 - 400	Thermal
Pressurized water reactors (PWR)	II	Enriched UO_2 or MOX	Water	290 - 325	Thermal
Boiling water reactors (BWR)	II	Enriched UO_2 or MOX	Water	280 - 330	Thermal
Pressurized heavy water reactors (PHWR)	II	Natural UO_2	Heavy water	270 - 310	Thermal
Advanced gas-cooled reactors (AGR)	II	Enriched UO_2	CO_2	340 - 635	Thermal
High power channel-type reactors (RBMK)	II	Enriched UO_2	Water	260 - 290	Thermal
Gas-cooled fast reactors (GFR)	IV	U-238, with U-235 or Pu-239	He	850	Fast
Lead-cooled fast reactors (LFR or LBEFR)	IV	U-238, with U-235 or Pu-239	Pb or LBE	480 - 570	Fast
Molten salt fast reactors (MSFR)	IV	UF in salt	Fluoride salts	700 - 800	Fast
Molten salt reactors (MSR)	IV	UO_2 particles in prism	Fluoride salts	750 - 1000	Thermal
Sodium-cooled fast reactors (SFR)	IV	U-238 & MOX	Na	500 - 550	Fast
Supercritical water-cooled reactors (SCWR)	IV	UO_2	Water	510 - 625	Thermal or fast
Very high temperature gas reactors (VHTR)	IV	UO_2 prism or pebbles	Helium	900 - 1000	Thermal

Gen-IV International Forum has designated six potential systems as candidate reactors to develop further [2]. Among these reactor types, Lead-cooled Fast Reactors (LFR) and Lead Bismuth Eutectic-cooled Fast Reactors (LBEFR) have been the focus of recent years. LFR and LBEFR reactor systems are also known as Heavy Liquid Metal (HLM) cooled reactors, along with Sodium-cooled Fast Reactors (SFR). LFR and LBEFR are proposed with similar generic designs (seen in Figure 1) which are subject to change depending on purpose and builders.

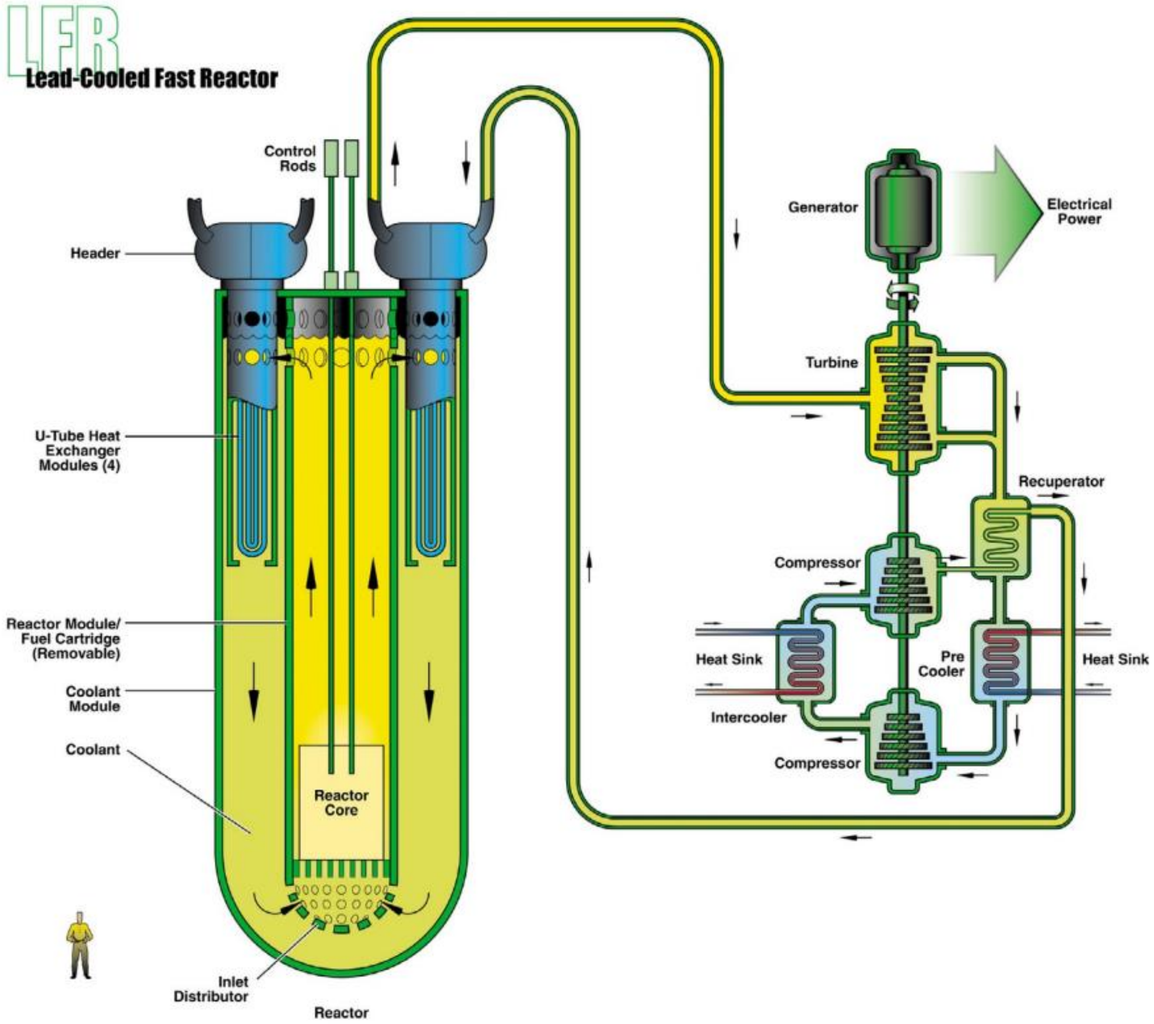

Figure 1: Lead-cooled Fast Reactor diagram with the components, reprinted from [2, 19].

LFRs take the "*fast*" name due to their fast neutron spectrum, where unmoderated fast neutrons drive the fission chain reaction, enabling new features. Water-cooled reactors use thermal neutrons (~0.025 eV), which are "slower" from the fast neutrons ($\geq$1 MeV). These fast neutrons used in LFRs can use the fuel more efficiently (>90%) compared to the <2% utilization in water-cooled reactors [2]. This efficiency comes from multiple sources. Fast neutrons enable the usage of minor actinides (Np, Am, Cm) as fuels, along with Pu [20]. All these are artificial elements with extremely low abundance in the world, e.g. Pu 10^{-15} mass % of the earth [21]. However, these also occur as by-products of regular reactor operation with thermal neutrons. In their current state, they end up in intermediate storage facilities, waiting to be disposed of in final geological repositories. Recycling of U, Pu, and Am allows us to decrease radiotoxicity of final repositories [22] and decrease uranium mining by utilizing these isotopes [23]. This can help us close the nuclear fuel cycle and increase the efficiency of nuclear energy. In addition, fast reactors can reach higher burn-up and could “burn” minor actinides, generating less toxic waste in the end, again contributing to the overall nuclear waste solutions [24, 25].

In the current development plans, all HLM-cooled reactors are of interest; including LFR, LBEFR and SFR [19]. In EU, there is more experience on the SFR technology, mainly thanks to the Rapsodie, Phenix and Superphenix reactors that were run and later decommissioned in France [26]. LBEFR were employed by the Soviet Union to power submarines, but some of them suffered from serious accidents. Details of the individual accident scenarios are inaccessible [27]. In US, TerraPower™ is preparing to build a SFR/molten salt storage combined system [28]. In the EU, ALFRED and MYRRHA lead the way for LFR and LBEFR, respectively [29]. While the discussion about the best system continues, certainly all systems have their merits. However, LFR technology does have some solid advantages over the other systems.

On the corrosion front; the issues still persist on all the HLM coolants (Na, Pb, LBE). Here, molten Pb and LBE have the advantage of non-violent reaction with moisture and oxygen; whereas Na reacts violently with air as well as water under release of hydrogen gas. In case of a leak, Na is definitively the more dangerous coolant. The disadvantage of molten Pb and LBE is their high density. A higher density puts higher mechanical loads to pumping systems and structural components, as well as increased risk in the case of a seismic activity.

Between Pb and LBE, neutronics of molten Pb is more advantageous as Bi to Po transmutation is mostly eliminated.

As for the thermohydraulic properties, natural convection of molten Pb can create a passive cooling loop that is considered beneficial against possible coolant pump failures. Pb melts at 327.5 °C and boils at 1747.8 °C, well above the expected operating temperatures of the reactors (400-500 °C) and even higher than melting point of the claddings (~1500 °C) [27, 30]. This virtually eliminates the possibility of a coolant loss scenario. Another advantage over water cooled reactors is the elimination of H_2 generation as hydrogen is only present as an impurity for oxygen control.

2.2. Fission Products and Joint Oxide Gain (JOG)

The abbreviation “JOG” is not new, but the use has been limited. One of the first publications to use the JOG abbreviation was by M. Tourasse et al. (1992), where the authors defined the fission product accumulation between cladding and fuel pellet as “*Joint Oxyde-Gaine*” or “*JOG*” [14]. In the most simplistic sense, JOG is an accumulation of fission products, and using the name “fission products” should work just as well. However, the situation in fast reactors demanded a new definition, as the burn-up is much higher compared to thermal reactors where fission product yield might not be enough for JOG formation.

Fission products are regular by-products of fission chain reactions and nuclear reactors. In nuclear power reactors, the fission chain reactions are sustained with neutrons. When a neutron splits a fissile nuclide, three main components occur; energy (in the form of heat), fission products and more neutrons. Neutrons are used to drive the fission chain reaction further, although not with 100% efficiency. The heat is transferred out of reactor core by coolants, while fission products remain in place, contained in the fuel pins. The relative yield can be seen in Figure 2, as compared between fast and thermal neutrons. The chemistry and yield of fission products has been studied extensively, and their amounts are usually a function of burn-up.

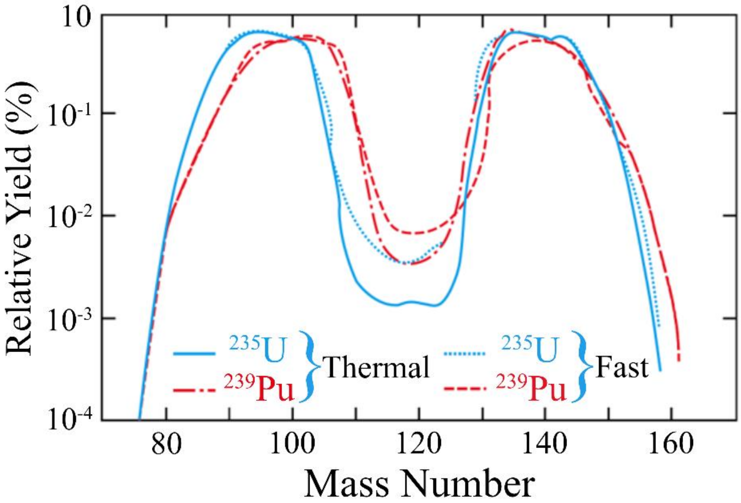

Figure 2: Relative yield of fission products, for ^{235}U and ^{239}Pu as fissile isotopes, in thermal and fast neutron fluxes, adapted from [31].

The final composition of the fission products has been defined before for fast reactors [10, 32]. However, the state of fission product depends on the temperature gradient of the fuel, local oxygen potential and even the longitudinal location in the fuel pin. For example, gaseous fission products like Br, Kr, I and Xe can escape the fuel pellet in case of a cracked pellet, later travelling to the higher parts of the fuel pin. Regardless of fuel composition, longer-lived radionuclides of Se, Kr, Rb, Zr, Tc, Pd, Sn, I, Cs, Sm, Mo, Te and Eu have been observed and reported [25]. The composition of elements is not limited to these; however, the list of elements is long, and not all of them are relevant to our study. As a result of the migration of fission products in the fuel pellets, their state can change drastically, as seen as a function of utilization (or burn-up) of the fuel, in Figure 3.

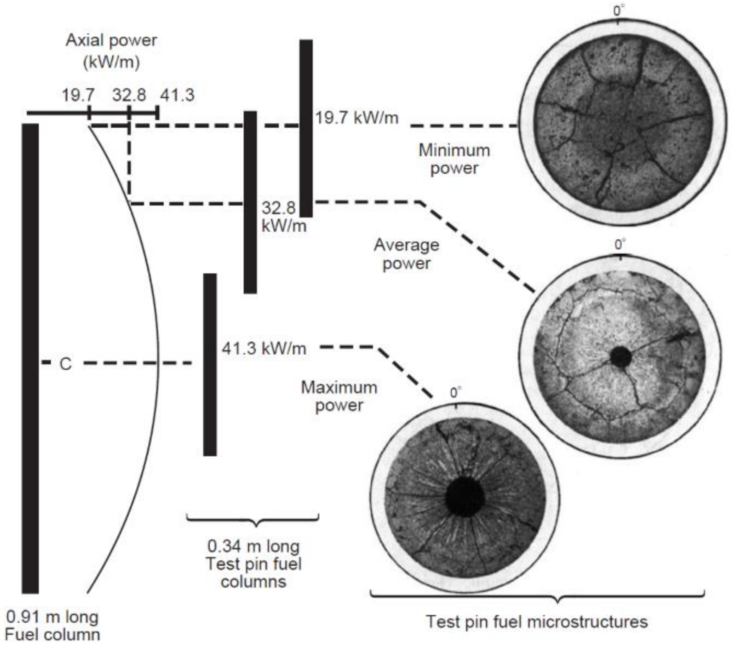

Figure 3: The restructuring of mixed-oxide fuel, in different heat rates, or burn-up, adapted from [33].

As stated before, JOG is the name given to the accumulation of fission products. In fast reactors, the thermal gradient of fuel pellet can be as high as ~450 K mm^{-1}, which causes some fission products to diffuse to the rim of the fuel pellet where it accumulates between cladding and fuel pellet [34, 35]. For MOX fuel, above 7% fission per initial metal atom (FIMA), JOG formation has been reported, studying irradiated fuels [36]. It has been reported that MOX fuels have reached >20% FIMA, and aim to reach even higher, highlighting the importance of studies on JOG formation and chemistry [37]. Due to the variable parameters of a fuel pin and the mix of fission products, there is no exact composition to be defined and studies have been dedicated to identifying the main components of the JOG phases. The migrating elements have been identified majorly as Cs, Mo, Te, I, Zr, Ba; while their location and oxidation states have important implications on the JOG composition [35].

2.3. Claddings and Corrosion Phenomenon

Corrosion on claddings is not a new field, and work continues on improving Zr-based alloys; even though, the choice of materials has not changed drastically in the last ~60 years. Currently, water-cooled reactors with their Zr alloy claddings make up the vast majority of commercial nuclear reactors [38]. However, Fe-based cladding tubes are being researched as an alternative to Zr alloys for accident tolerant claddings after the Fukushima accident [39]. In the case of planned Gen-IV reactors, Fe-based alloys (or steels in general) are foreseen as both structural and cladding materials. Different kinds of steels have been used as structural materials, for example, carbon steels in reactor vessels, but steels are still not the widely used material for claddings.

Claddings are an essential part of nuclear reactors and act as the 2nd barrier (after the fuel pellet) for the potential release of radionuclides as well as act as the protective cover for the fuel pellets. In normal operation, fuel pellets (U, Pu, minor actinides, fission products) should not come in contact with their respective coolants. The main purpose of the claddings is to hold the fuel pellets inside and keep them from being in contact with the coolant; highlighting the importance of their integrity. As fuel heats up due to fission reaction, claddings transfer this heat to the coolant. Therefore, claddings also work as a heat transfer medium between fuel and coolant. In most reactors, fuel is made up of cylindrical pellets of the fuel materials, stacked vertically on top of each other inside the cladding tube, which is usually ~1 cm in diameter, and several meters long in height. The dimensions are highly dependent on the reactor design. On the top and bottom parts of the claddings, there are supporting structures (end plugs, springs etc.) to keep the fuel elements in place, while the ends of the cladding tubes are sealed, and the volume inside filled with He. A generic version of a fuel pin can be seen in Figure 4, highlighting different components. Many fuel pins are wrapped together in what is called a “fuel assembly”. These assemblies hold the fuel pins stable and provide channels for the coolant to flow around the tubes. 10 to 100s of fuel assemblies make up the reactor core.

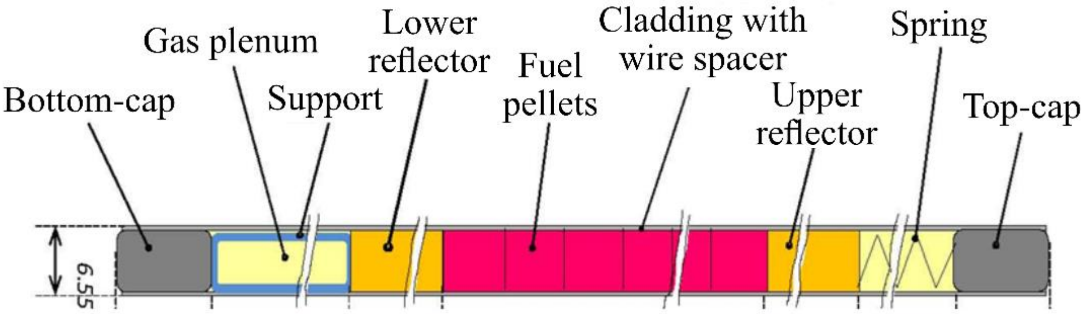

Figure 4: Generic vertical fuel pin design schematic, in horizontal orientation, with the components.

In general, during reactor operation, claddings are under the effects of chemical corrosion, mechanical strain and heavy irradiation field. The focus of this section is on chemical corrosion. Cladding tubes are under corrosive effect from two different sides; inner and outer side. On the outer side, the coolant is the main corrosive species, while fuel and JOG elements are the main inner side corrosive species. It is extremely important to consider the effects of both while talking about cladding corrosion as both can contribute to an eventual cladding breach. It has been reported that irradiation can enhance the corrosion process, accelerating time to failure and decreasing the lifetime of the fuel assembly [40], which will be explained in a later section. Subsequently, the combined effects of corrosion lower the economic viability of the reactor as refueling is an expensive process; both from an operational and material point of view. Here, the candidate steel cladding tubes of LFRs are at a disadvantage as there are no fully operational reactors that can mimic the in-situ reactor conditions. Instead, laboratory scale setups are used with some assumptions. Unfortunately, studies on dual environment corrosion have been severely lacking, but the simultaneous effects of these environments are important for breach scenarios. The release of radioactive fission products from the inner to the outer side is not a desirable situation. On the separated chemical fronts (inner & outer), the initial stages of the corrosion process can be considered separately. However, in the case of accident scenario research, especially for cladding breaches, the corrosion processes at opposite sides of the cladding wall would influence each other.

The separation of chemical fronts is not the only difference. Another important aspect is the curvature of the corroding surface. The inner side of the tube is concave, while the outer side is convex. The curvature of the surface can have an effect on the oxide growth, putting the oxide layer under tensile or compressive stresses [41]. Therefore, as important as studies made on flat surfaces (or more widely known as *coupons*), the tubular shape of the claddings cannot be ignored for corrosion research.

2.3.1. Corrosion by Molten Pb and LBE

Molten Pb and LBE are proposed coolants for some Gen-IV systems. In the case of ALFRED, molten Pb is the primary outer-side corrosive substance for cladding tubes. Even though molten Pb brings advantages such as natural convection and the (potential) ability to retain fission products, molten Pb is highly corrosive toward stainless steels. The intensity and characteristics of this corrosion process are highly dependent on the type of steel. The research on LFR has been advancing since the 1960s, where a variety of steels have been studied as candidate alloys for claddings or other structural materials [42]. Still, the corrosion issues, especially of reactor core materials still remain an issue, and limit the deployment of Gen-IV reactors [43]. Although good results have been obtained for extended amounts of operation time, material lifetime is still a limiting factor and most studies do not consider irradiation.

In terms of HLM induced corrosion, the main issues can be summarized as alloy dissolution (e.g., Ni leaching), liquid metal embrittlement (LME), oxidation and erosion of protective scales (native or coated). The corrosion intensity was affected by parameters such as oxygen concentration in HLM, temperature, static or flow conditions, steel's composition and even manufacturing methods. Corrosion by molten Pb and LBE act similarly, where dissolved oxygen in the molten metal is a key parameter. Most studies have managed to define a relationship between the dissolved oxygen in molten Pb and the protectiveness of oxide layers [44-46]. The components of the steel have the tendency to react with the dissolved oxygen to form oxide layers on the surface of the steel, which in turn can protect the bulk of the steel. Here, unlike most oxidation phenomena, oxygen is in a dissolved state. During the oxidation by HLM, the weight percentage of the oxygen in the HLM is the discussed parameter, instead of oxygen partial pressure. The goal is to keep the oxygen concentration in a balanced state, as too high or too low concentrations can cause issues. In the case of low oxygen concentration, the formation of an oxide layer can be hindered. This could mean that HLM can come in contact with bare metal, quickly causing dissolution of alloy components (Fe, Cr, Ni) [47, 48]. An oxygen concentration high enough can cause protective scales to form, such as Fe_2O_3, Fe_3O_4, Cr_2O_3 etc. If the oxygen concentration is too high, the oxide scales might form too fast, and their protective properties could be compromised due to issues like porosity and nonuniformity. In addition, a non-compact protective scale can be eroded away by the flowing coolant. The current envisioned strategy against HLM corrosion is to control the oxygen concentration by having a mixture of $Ar+H_2+H_2O$ cover gas. This control has been achieved by expensive and complicated laboratory scale setups [49-51]. The work continues to employ this method on an industrial scale. However, even a balance concentration cannot protect the steel against molten Pb attack during temperatures that exceed operational parameters (>500 °C) [52-54]. In the literature, molten LBE is the more researched coolant, due to its low melting point (127.5 °C vs. 327.5 °C of Pb) providing a less corrosive environment. Molten LBE corrosion has been investigated with austenitic and ferritic-martensitic steels in varying oxygen concentrations [49, 55, 56], as well as under the influence of mechanical stress [57-59].

2.3.2. Corrosion by Fission Products

Fission product corrosion is a less mature subject than corrosion by HLMs. Since burn-up and the subsequent fission product production is low in thermal reactors, the accumulation of fission products is much sparse compared to fast reactors. However, as explained before, JOG formation is well documented in fast reactors. Since JOG phases fill the gap between cladding and fuel pellet, at high burn-up conditions, they remain as the most important corrosive substance from the inner side of the cladding tubes. Several studies have investigated the most important and relevant JOG phases and reported Cs_2MoO_4 as one of the most important JOG phases [14, 35-37]. Figure 5 shows the clear accumulation of Cs and Mo in a high burn-up (>15% FIMA) MOX fuel pellet. More phases like Cs_2Te, CsI have been reported but Cs_2MoO_4 was chosen as the relevant compound for this thesis work. Many studies have investigated the Cs_2O, MoO_3, Cs_2MoO_4 system both experimentally and thermodynamically [34, 60-63]. These have been used as a starting point for both preparation and thermodynamic data acquisition for Cs_2MoO_4. Mo(VI) and Mo(IV) are known strong oxidizers, meaning their contact with steel components can result in a strong corrosion attack.

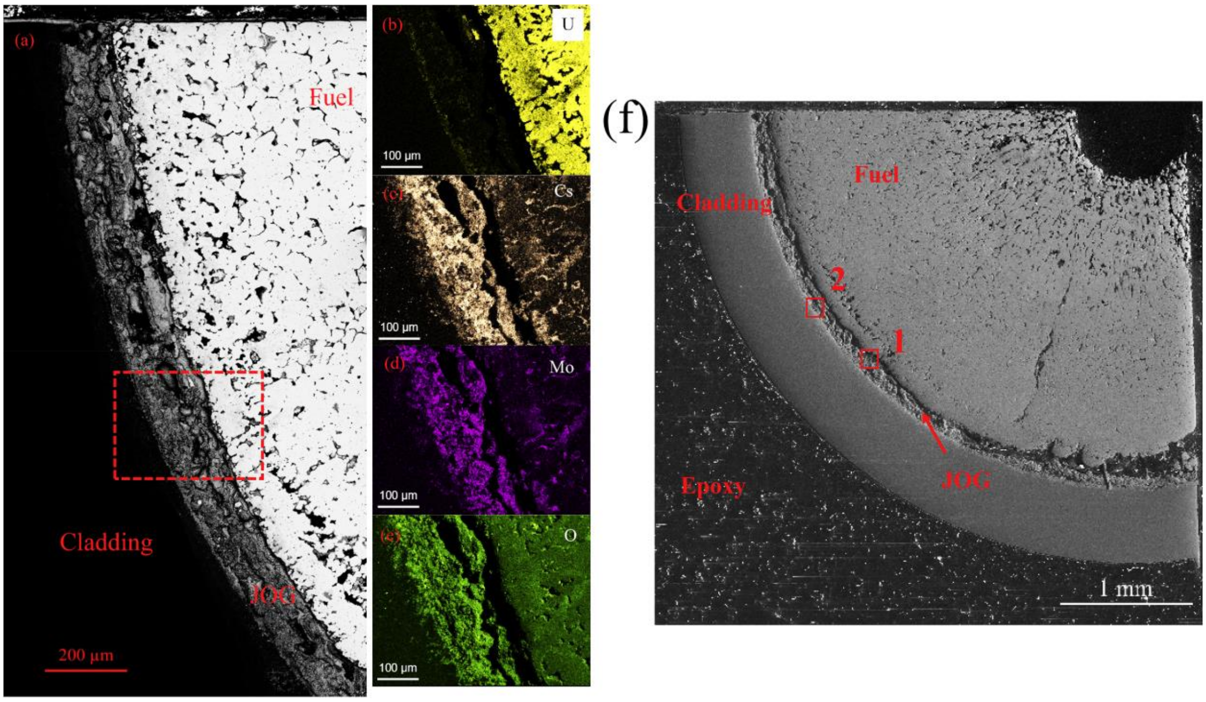

Figure 5: JOG formation on an irradiated MOX fuel pin at high burn-up (>15% FIMA). (a) BSE micrograph of cladding and fuel area, (b)-(e) respective EDX maps of the elements, (f) low magnification (100x) SEM overall image of the fuel pin cross-section. Reprinted from [35].

In this study, the chemical corrosion properties of MOX are not considered, for two reasons. Firstly, U and Pu are not chemically corrosive enough to be relevant as a so-called "corrosive species" [64]. Secondly, and arguably more importantly, the scope of the research considers a high burn-up situation where fission products are present widely. This means the formation of JOG phases has progressed enough that the interior of the cladding tube is in contact with the relevant JOG phases.

2.3.3. Irradiation Enhanced Corrosion

In order to calculate and compare the effects of irradiation, a measurement unit "displacement per atom (dpa)" has been introduced. Among the nuclear scientists, dpa is used as a normalized unit to define radiation damage, irrelevant of reactor type and irradiation source (neutrons, accelerated heavy ions etc.) [38]. When each atom is displaced from its lattice position once (on average), this is quantified as one dpa.

Irradiation is possibly the most difficult aspect of cladding corrosion to investigate. The effects of irradiation on thermal reactors are well documented: vacancy and defect formation, void swelling, microstructural changes; and these phenomena are leading to enhanced embrittlement, creep and corrosion [1, 40, 65]. HLMs can cause liquid metal embrittlement; and irradiation can have a synergistic effect with HLM to further increase the effects of this embrittlement [43]. The negative effects of irradiation are more evident in fast reactors as irradiation field increases drastically. In Pressurized Water Reactors (PWRs) and Boiling Water Reactors (BWRs), cladding materials can be subjected to ~10 dpa in their lifetime; while this value can increase to 150-200 dpa in LFRs [5, 38, 65]. Unfortunately, to our knowledge, there is no irradiation source or reactor in the world that can provide ~100 dpa in >600 °C conditions. Therefore, we are limited to discussing our results in relation to the already known effects of irradiation. An extremely heavy irradiation field will always be present in LFRs. Even if suitable materials are found and tested in laboratory conditions, the degradation of neutron flux should not be forgotten when discussing the results. This is one of the reasons why 15-15Ti was selected as a cladding material for ALFRED and MYRRHA; as the addition of Ti is expected to increase the resistance to irradiation induced void swelling [4, 5, 66].

3. Theory

Almost all metals have a tendency to go to their energetically favored oxidized state in contact with air, with the exception of noble metals. In most low temperature conditions, passivating layers can help metals stay unoxidized, owing to their slow and uniform growth. However, given the right conditions of oxidative environment, metals are prone to release their valance electrons. In corrosion science, these electron receiving elements can be hydrogen, carbon, nitrogen, chalcogens (6A group) and halogens (7A group) in their neutral state, or another more noble metal ion. For the purpose of explanations and relevancy to this thesis, oxygen will be considered as the main electron-receiving (oxidizing) element. Equation 1 presents the oxidation reaction of the reactant metal M with gaseous oxygen, where x and y are the stoichiometric constants.

$$xM(s) + \frac{y}{2}O_2(g) \rightarrow M_xO_y(s) \tag{1}$$

The Gibbs free energy (ΔG) can be written as Equation 2; ΔG^o is the standard Gibbs free energy, R is the universal gas constant and T is temperature in K. Here the activities of solids are 1, and the activity of oxygen can be written as its partial pressure (p_{O_2}). If we assume that the reaction is in equilibrium ($\Delta G = 0$), we can further rewrite as Equation 3.

$$\Delta G = \Delta G^o + RT\ln[\frac{a(M_xO_y)}{a_M^x \cdot p_{O_2}^{y/2}}] \tag{2}$$

$$\Delta G^o = RT\ln(p_{O_2}^{y/2})] \tag{3}$$

The dependency of oxide formation to oxygen partial pressure and temperature can be seen here. In Ellingham diagrams, this dependency has been plotted for various metals, assuming a 1 mole of O_2 per reaction [67]. Similar diagrams have been made for sulfides and nitrides as well. The Ellingham diagram can help us compare the relative stability of different oxides, as a function of temperature, O_2 partial pressure, and H_2/H_2O or CO/CO_2 partial pressures. The formation or the dissociation of the oxides can be determined using these parameters. As useful as the Ellingham-based diagrams are, in a corrosion system, the reality is not simple enough to consider Ellingham alone. In most of the high temperature application alloys, many components are present, further complicating the chemistry. However, even though the Ellingham diagrams are derived from thermodynamic calculations alone, they are still powerful tools to compare our oxide formation and/or dissociation assumptions.

The relative stability of oxides can help us determine suitable protective oxide layers, or which ones to avoid using. The lower the ΔG^o value of a metal oxide, its stability increases, placing it in the lower sections of the Ellingham diagram. In addition to thermodynamic stability; kinetic aspects like grow speed, continuity, diffusion of cationic and/or anionic species [68], porosity, resistance to breakaway, self-healing are important factors to classify an oxide layer as *protective*. Whether the oxide layer is native or coated, the ability to create a barrier between the corrosive environment and the metal can be invaluable for the long-term function of the metallic components. Eskolaite (Cr_2O_3) and α-Al_2O_3 are known and proven examples of such protective layers. But, in corrosion, any layer can be useless given the right circumstances. Protective oxide layers have limited application windows, depending on the atmosphere, stress and temperature.

This brings us to the case of corrosion by molten metals, in particular Pb (melting point; 600.65 K) and LBE (melting point; 400.65 K) [27]. These Pb eutectics are used in their liquid form; therefore, their ability to dissolve certain elements must be considered when discussing the chemistry of their corrosion on alloys. As oxygen was discussed recently, it makes sense to firstly explain the oxygen solubility in Pb and LBE. The dissolved oxygen in Pb and LBE is the main culprit when discussing the oxidation of metals in contact with molten Pb or LBE. The fact that Pb and LBE can be oxidized sets limits on oxygen solubility. In literature, the dissolved oxygen in the molten metals is actually reported as a function of concentration and has been reported with Pb- and Bi-oxides as limits. The upper limits of dissolved oxygen concentration (C_O, in wt.%) have been presented by Fazio et. al.; Equation 4 for Pb ($C_{O,Pb}$) and Equation 5 for LBE ($C_{O,LBE}$) [27], where T is temperature in K.

$$\log C_{O,Pb} = 3.23 - \frac{5043}{T} \text{ (for 573 K < } T \text{ < 1373 K)} \tag{4}$$

$$\log C_{O,LBE} = 2.25 - \frac{4125}{T} \text{ (for 673 K < } T \text{ < 1013 K)} \tag{5}$$

Corrosion protection is what determines the lower limit for the dissolved oxygen. Equation 6 was established as to limit the range of this concentration between PbO and Fe_3O_4 [27]. Since Bi_2O_3 is the lesser stable oxide, PbO was considered for LBE too.

$$2\Delta G^o_{PbO} > RT \ln p_{O_2} > 0.5\Delta G^o_{Fe_3O_4} \tag{6}$$

This balance has been presented in an Ellingham diagram in Figure 6, comparing the oxides of Fe, Pb and Bi, with dissolved oxygen concentration in wt.%. Figure 6-b shows the practical results of this oxygen concentration balance, which will not be discussed further in this work. The important part here are the consequences of lower concentrations of oxygen, as the liquid metal starts to selectively dissolve alloy elements, due to direct contact. In the presence of an oxide layer, this is not a big issue as oxide formation occurs faster compared to dissolution [27].

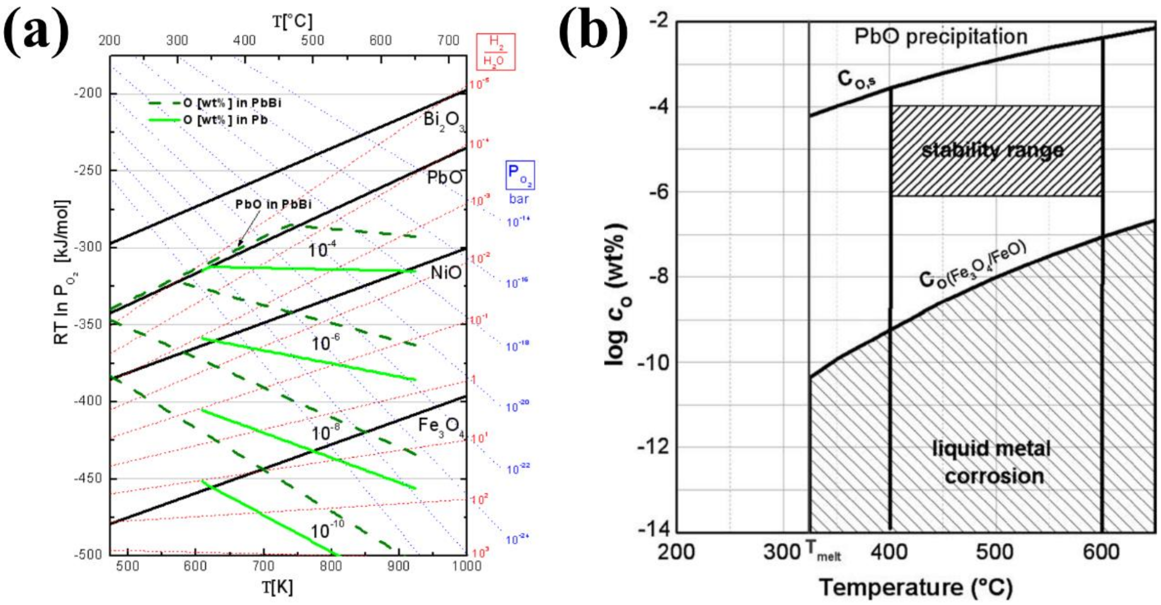

Figure 6: (a) Ellingham diagram of Pb, Bi and steel components oxides, reprinted from [69], colored version from [27]; (b) Oxygen concentration range of stable conditions in molten Pb loop, with PbO formation and oxide dissociation as the limits, reprinted from [69].

If the protective layers fail due to either thermodynamic or kinetic reasons, a direct contact between metallic components and the molten metal will be established; where dissolution of alloy will begin. The temperature dependent onset of selective element dissolution can be read off the phase diagrams in Figure 7. Ni and Cr are highly soluble in molten Pb, while Fe has low solubility in Pb and is therefore shown in a narrow phase diagram section. The temperature gradients in reactor can even result in reprecipitation of these dissolved components, causing plugging and clogs. Even though the liquid phase would be expected to reach a saturation level, the coolant volume is vastly greater than the structural components. Practically speaking, saturation is difficult to happen in hot regions of the reactor (e.g., core, around claddings). Here, the focus should be on the section closer to 100 at.% Pb.

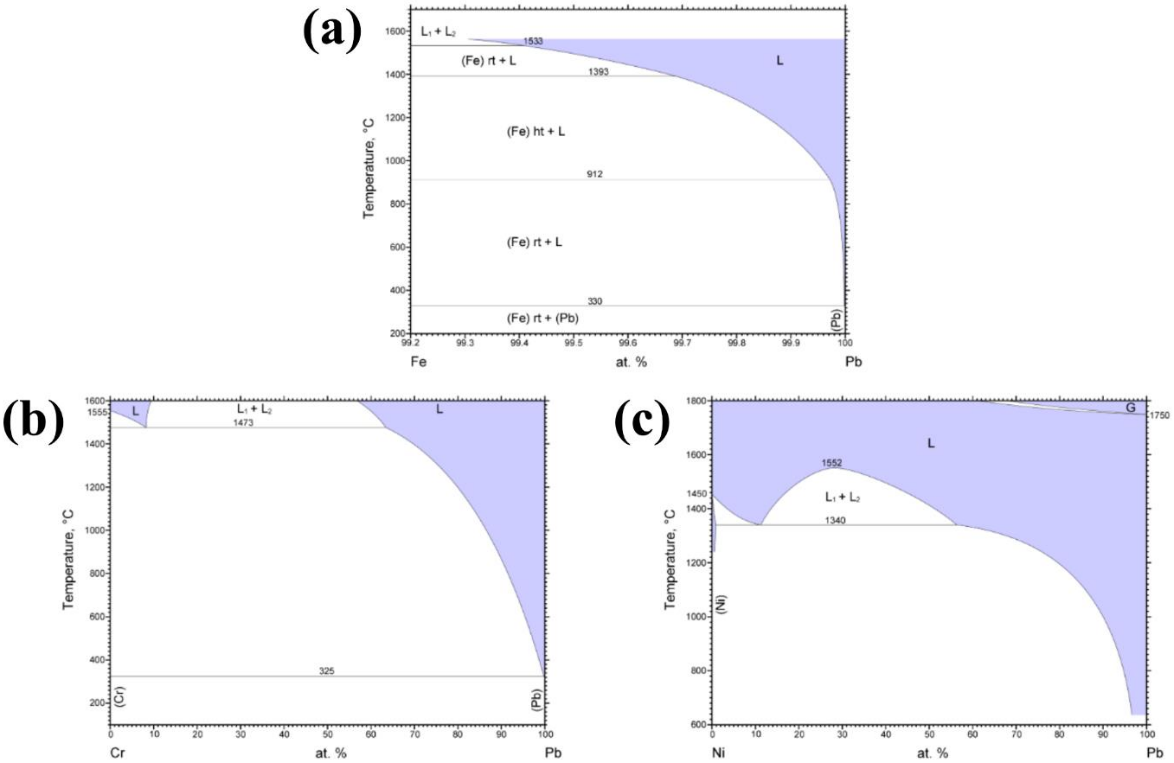

Figure 7: Binary phase diagrams of Pb with (a) Fe [70], (b) Cr [71], (c) Ni [72].

In this section, a summary of the theoretical phenomena behind the high temperature corrosion by molten Pb and LBE was explained briefly. Oxidation and dissolution simultaneously are the most pronounced corrosion processes occurring in these systems, and they cannot be considered separately from each other. Especially in our research, at elevated temperatures (so-called accident conditions) kinetic effects increase oxide scale growth and the viscosity of the molten Pb.

4. Experimental

4.1. Materials

The cladding tube 15-15Ti was received from Sandvik™ and used in two forms; as received tube (subject to drilled operations later) and in coupon form. 15-15Ti stainless steel is part of the steel alloy family of 316. The elemental composition of this alloy has given it its name, where both Cr and Ni are close to 15 wt.%, and ~0.5 wt.% Ti was added to improve irradiation resistance. The specification of the cladding tubes can be found on Delville et. al. [73]. As seen in Table 2, the elemental composition was further confirmed by EDX. In addition to the cladding tube in question, Swagelok™ stainless steel assembly parts of various kind were used, whose alloy composition can also be seen in Table 2 [74].

Table 2: Elemental composition of the capsule's components in weight percentage (n.s. = not specified, n.d. = not detected, n.q. = not quantified), EDX data collected with 25 kV.

Sample	Cr	Ni	Mo	Mn	Si	C
Swagelok (Alloy 316) – Advertised	17.08 - 19.00	12.5 - 15.00	2.5 - 3.0	Max 2.00	Max 1.00	Max 0.030
Swagelok (Alloy 316) – EDX	17.96	12.9	3.15	1.85	0.7	n.q.
Cladding Tube (15-15Ti) – Ref [73]	15.08	15.04	1.21	1.83	0.56	0.10
Cladding Tube (15-15Ti) – EDX	15.56	14.84	1.58	2.1	1	n.q.

Sample	S	Ti	P	Co	B	N
Swagelok (Alloy 316) – Advertised	Max 0.015	n.s.	n.s.	n.s.	n.s.	n.s.
Swagelok (Alloy 316) – EDX	n.d.	n.d.	n.d.	n.d.	n.d.	n.d.
Cladding Tube (15-15Ti) – Ref [73]	<0.001	0.49	0.013	0.02	0.0028	0.011
Cladding Tube (15-15Ti) – EDX	n.d.	0.41	n.d.	n.d.	n.d.	n.d.

Sample	Cu	V	Ta	Ca	Fe
Swagelok (Alloy 316) – Advertised	n.s.	n.s.	n.s.	n.s.	Bal.
Swagelok (Alloy 316) – EDX	n.d.	n.d.	n.d.	n.d.	63.3
Cladding Tube (15-15Ti) – Ref [73]	0.026	0.034	<0.005	<0.010	Bal.
Cladding Tube (15-15Ti) – EDX	n.d.	n.d.	n.d.	n.d.	64.5

For the coolant side, Pb powder (-325 mesh, ≥ 99% trace metal basis, Sigma-Aldrich, Lot #STBG5744V) was used. The powder was mostly handled in an Ar-filled glovebox, with a gas quality of 1 and 1.4 ppm oxygen. For Cs_2MoO_4, two different sources of powders were used. First was the off-the-shelf Cs_2MoO_4 (75 µm, 99.9% purity, GoodFellow), that was used without additional chemical treatment. Due to the hydrophilic properties of Cs_2MoO_4, the powders were either stored in air-tight desiccators employed with P_2O_5 desiccant or in an Ar-filled glovebox. The compound was controlled for side products via XRD. The second was the in-house synthesized powders, whose details will be given in section 4.6. For the synthesis, Cs_2CO_3 (99.9% trace metals basis, Sigma-Aldrich) and MoO_3 (≥99.5%, Sigma-Aldrich, Lot #MKBP3396V) powders were used, without additional chemical treatment.

4.2. Reaction Capsule

The aim of the project is to investigate the dual atmosphere corrosion on the cladding tube material, induced simultaneously by HLM coolant and JOG compounds at accident conditions (>600 °C) and high burn-up. Studies on molten Pb and molybdate corrosion have been previously reported, but the literature is lacking studies where dual effect of these chemicals was the focus. Both of these chemicals have different requirements of physical and chemical states, which would accurately mimic reactor conditions. Since it is difficult to keep them in these states simultaneously, a custom setup was built to investigate this complex corrosion process [75]. A similar setup was established before by Vigier et al. [76], using Swagelok™ parts with LBE and MOX pellet at 800 °C. The setup built for this work was an extension of that, with the aim of using either molten Pb or LBE, along with various simulated fission products.

Molten Pb is the chosen coolant to be used with 15-15Ti cladding tube; therefore, corroding the outside of the tube. Cs_2MoO_4 is a major species of JOG compounds, and it was chosen as a starting point for investigating the interaction between the inner side of the cladding and fission products. In a reactor operation, ideally, molten Pb and Cs_2MoO_4 would not come in contact, meaning that they stand on the opposite sides of cladding wall. This also means that they stand in different environments. Molten Pb would be in an oxygen-controlled state, and flowing to cool the reactor, covered by an Ar-H_2 gas mixture. Cs_2MoO_4 would accumulate around the rim of the MOX fuel pellet, a quite oxidizing environment due to the oxide fuel, but under an inert He atmosphere. Since they are not in contact, it is also important to start the experiment with separated molten Pb (or LBE) and JOG compound (Cs_2MoO_4 in this case). For our setup, we have utilized the original tube shape of the cladding. The appropriate Swagelok™ caps were used to seal the cladding tube with Cs_2MoO_4 inside with Ar, preventing excess oxidizing specie. In the future, the aim is to use this housing for other JOG compounds, like Cs_2Te, CsI, Cs_2TeO_4 etc. [34]. The chemistry of the molten Pb was not controlled actively, but the Pb powder was handled under Ar gas, maintaining an inert atmosphere. In addition, a bigger tube than cladding tube was used to seal the molten Pb housing.

The focus of this study was the corrosion process in accident conditions. In terms of temperature, this means >600 °C, but also to simulate an accident of cladding breach. A cladding breach is obviously not desired. However, in nuclear engineering, the research on simulated accident conditions is invaluable as the consequences of an accident are usually catastrophic, requiring pre-existing data to be obtained during reactor design phase. For our study, this means information about chemistry of coolant/fission product interaction, in the cladding breach conditions. In the present designs, the wall thickness of the cladding tube is ~450 µm. For experimental purposes, corroding through 450 µm of 15-15Ti is a long process. In addition, due to the random nature of a breach, it would be extremely difficult to pinpoint the breach locations, or to detect the existence. As molten Pb is opaque and completely solidifies at room temperature. Therefore, a notch geometry was introduced into the cladding tube to thin the tube in known locations. A significant decrease in exposure time was observed, also more options to investigate the breach were presented. Due to the shape of the notches (or drilled areas), a more controlled interaction of coolant and JOG could be observed.

The reaction capsule was the main experimental setup of this thesis. In the future, the capsule will be used with molten LBE as coolant. The use of different fission products is definitely wanted, but the relevance of fission products at the high burn-up conditions requires further consideration. I and Te shine as prime candidates due to their importance for environmental safety purpose; such as gaseous species at room temperature, long half-lives and decay products. The temperature limits of the capsule were well established as a result of this thesis, which is presented in results and discussion sections. Next sections will explain the design and other details of the reaction capsule, followed by the unique cross-section preparation.

4.2.1. Design of Reaction Capsule

The reaction capsule was made up of two main parts; the hosting tube assembly and the capsule tube assembly. The latter fits into the hosting capsule as shown in Figure 8. The hosting tube was made from the Swagelok™ steel (alloy 316), which was cut to 8 cm pieces from 22 mm outer diameter tubes with 2 mm wall thickness (Product Name: SS-T22M-S-2,0M-6ME). The fitting ferrule sealings and hosting tube caps (SS-22M0-C) were used to provided air-tight sealing of the reaction volume. The dimensions of the hosting tube were selected to accommodate the cladding tube assembly, and to house enough Pb. Even though a larger reaction capsule could be built, this would cause practical difficulties during the post-exposure characterization without providing a meaningful advantage.

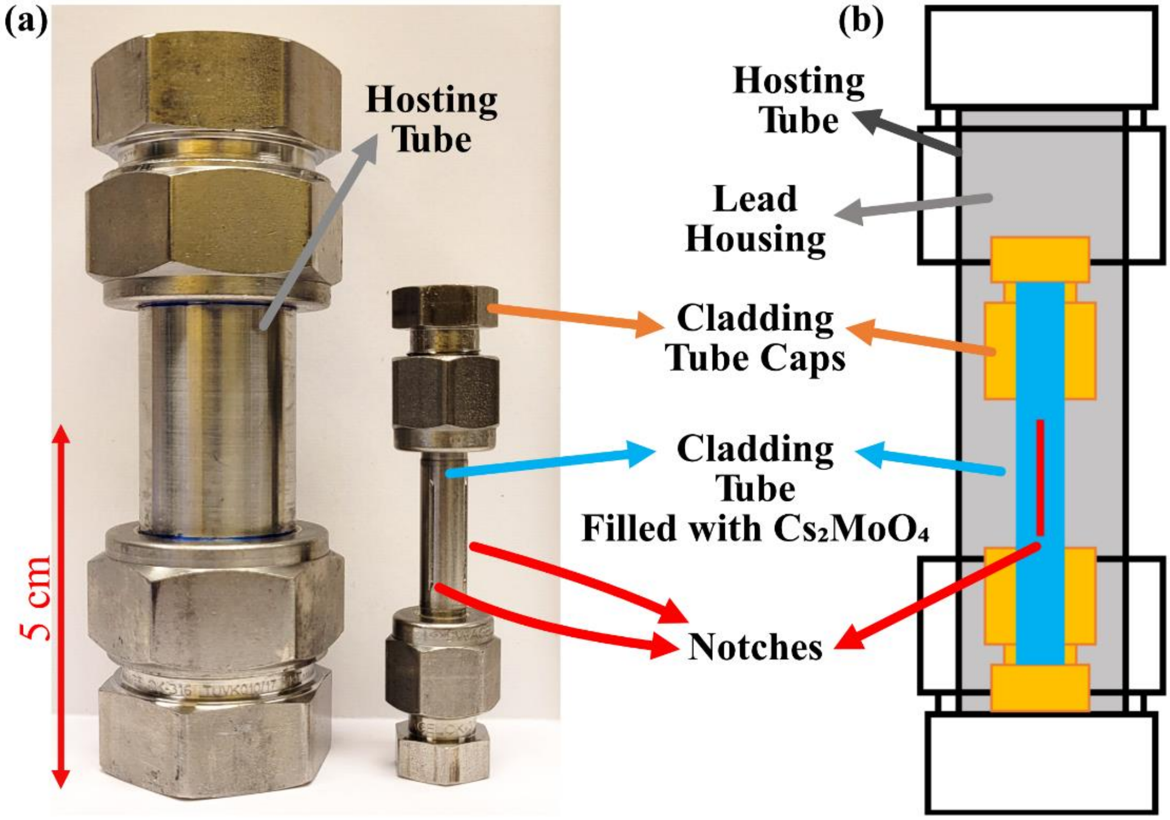

Figure 8: (a) Hosting and cladding tubes, assembled, (b) Blueprint of the reaction capsule.

The cladding tube in question was close in elemental composition to the hosting tube, but the specifications are different. Just like the hosting tube, the cladding tube needed air-tight caps; to separate the interior of the cladding tube (Cs_2MoO_4) from the molten Pb inside the hosting tube. The cladding tube (outer diameter = 6.5 mm) that was received from Sandvik™ cannot fit into any existing Swagelok™ caps. For this reason, a series of machining operations were performed. The cladding tube was cut into 50.4 mm long pieces, and 15.2 mm long sections from both ends were machined down to 6.35 mm (¼ inch) outer diameter to fit into “SS-400-C” Swagelok™ caps.

Notches were drilled lengthwise to the sides of the cladding tubes. 4 notches were drilled, at a 90° angle from each other. These “drilled areas” were important for the potential breaching scenarios, but the 450 µm wall thickness of the original cladding tubes makes it difficult to conform to precise machining. For this purpose, a simple setup was built from scratch to hold our cladding tube, as seen in Figure 9-a. The drilling was tested for 3 different depths. The consideration of shorter exposure times has made ~300 µm (Figure 9-c) and ~400 µm (Figure 9-d) deep notches more logical. However, the ~400 µm deep notch was too thin for the chemical corrosion to develop, and the cladding tube started to deform visibly due to the mechanical load of the drilling operation. In addition, the repeatability of the correct notch depth was not well. As a result, ~300 µm deep notch was selected as the optimized choice. In future studies, ~200 µm and ~400 µm can be used for exploring different aspects of the cladding tube.

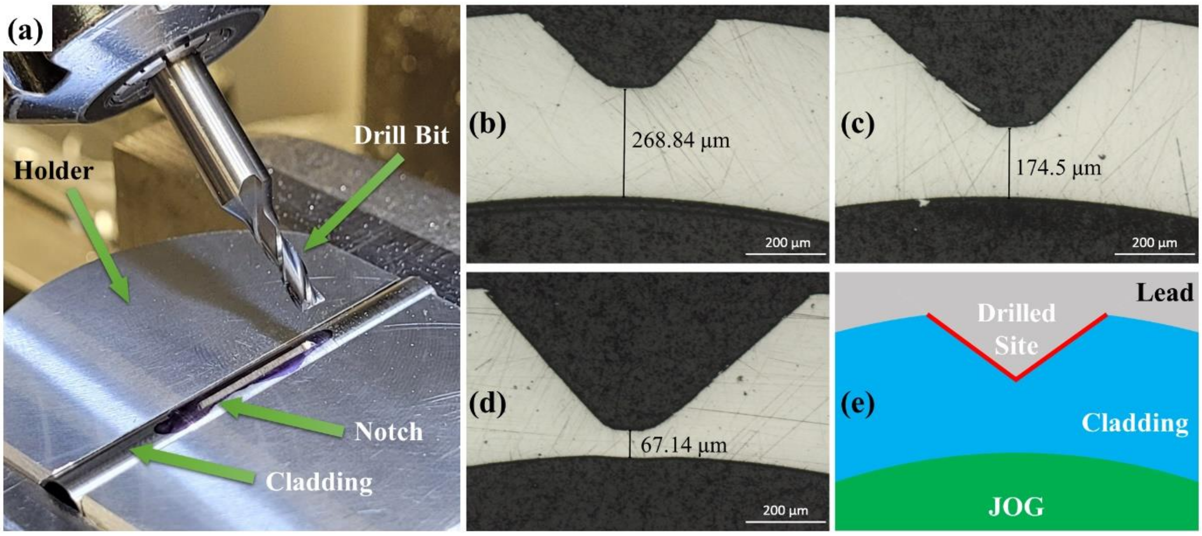

Figure 9: (a) Drilling setup for notches. Optical microscopy images of cross-sections showing drilled notches on non-exposed cladding tubes, with different depths; (b) ~200 µm, (c) ~300 µm, (d) ~400 µm, (e) Schematic of notch geometry cross-section.

4.2.2. Assembly

The initial assemblies of the caps to their respective tubes were done in air. After this, all the components were cleaned with ethanol, weighed and moved to an Ar-filled glovebox (1 - 1.4 ppm oxygen). In the glovebox, firstly the cladding tube assembly was filled with Cs_2MoO_4 powder, followed by the sealing of the assembly. The assembled cladding tube was put inside the hosting tube, which was then filled with Pb powder. The Pb powder was filled until it reached the top of the hosting tube. After Pb was loaded, the hosting tube assembly was also sealed. The sealed and ready reaction capsules were removed from the glovebox and taken to exposure step. After each powder loading and assembly stage, the pieces of the capsule were weighed. The weights of the Pb and Cs_2MoO_4 powders that were loaded can be seen in Table 3.

Table 3: Amount of Cs_2MoO_4 and Pb powder in the capsules for the exposure experiments.

Temperature (°C)	Cs_2MoO_4 Weight (g)	Pb Powder Weight (g)
600	2.11	77.44
700	2.34	77.10
800	2.40	74.95
900	2.72	75.26
1000	2.57	76.55

Due to being in powder form, the Pb volume was expected to shrink when melted, later during exposure. The shrinkage did occur, but the Pb level was still enough to cover the cladding tube completely, ensuring the interaction between molten Pb and the cladding tube. Figure 10 shows the verified level by a lengthwise cut through the middle of the upper section of the capsule.

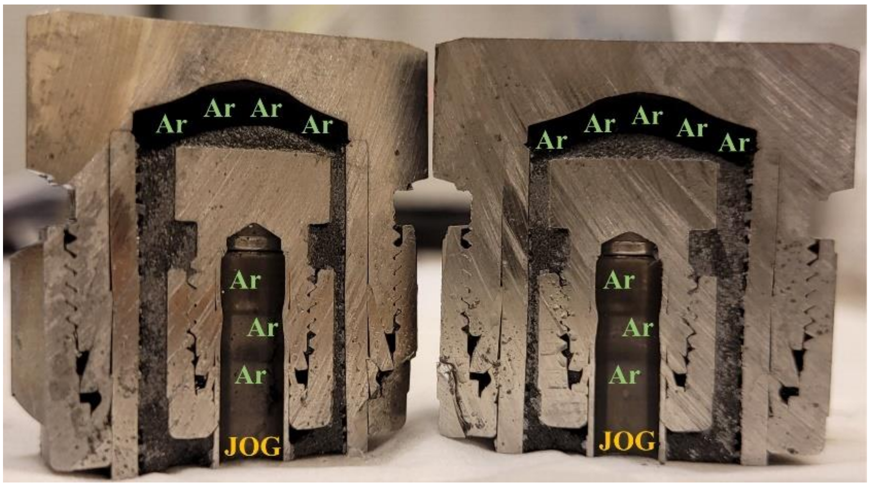

Figure 10: A lengthwise cut through the center of the upper section of a capsule, to verify the Pb level after shrinkage due to powder melting.

4.3. Exposure Experiments

The exposure experiments were conducted with assembled reaction capsules. After sealing the capsules, they were taken to a box furnace. The box furnace was a Lenton, UAF 14/10. The capsules were placed inside another container, standing upright, during the exposures. This served two purposes; to protect the furnace's refractory lining in case of a Pb spill, and to secure a thermocouple in place to calibrate and accurately read the temperature. The thermocouple was wrapped around the container and the tip was placed on to the capsule. A Type K thermocouple was used (Pentronic AB, Västervik, Sweden, Model 8102000, diameter = 2 mm) and it was considered as the actual measurement, instead of furnace's setting. Due to the extremely high latent heat input required by Pb, the Type K thermocouple in touch with the capsule was responding with a long delay to the temperature increase indicated by the furnace regulation.

Exposures were run in two main parts; pre-melting and main exposure. Due to the high latent heat needed to melt Pb, a 6 hour pre-melting stage at 345 ± 10 °C was introduced. Right after the pre-melting stage was completed, the capsule was heated to the main exposure temperature with the same heating rate of 2 °C/min. For the experiments presented in this thesis, all the capsule exposures were run for 168 h; except for the 1000 °C exposure, which was run for 52 h due to capsule limitations. The capsules were left to cool down inside the furnace, and they were removed after they reached room temperature. Cooled down capsules were moved to the cross-section preparation.

4.4. Confirmation Experiments

The confirmation experiments were introduced due to the characterization limitations of the capsule exposures. Due to the small features of the prepared cross-sections, phase analysis by XRD was not reliable. In addition, the interaction of 15-15Ti and Cs_2MoO_4 was not well studied in the literature. In order to acquire more data about this interaction and eliminate the possibility of molten Pb interaction, confirmation experiments were performed.

In these experiments, the 15-15Ti cladding tube material was flattened. The tube was cut from one side, followed by a repeating series of heating and flattening. After sufficiently flat, a pressing tool was used to hold the coupon in place, and heat treated at 850 °C in air. The tool was removed from the furnace after 2.5 h and let cool down to room temperature. An oxide film was formed, which was removed by polishing during the sample preparation step. The surface of the exposure was grinded with SiC paper down to size #4000 (using water as lubricant), followed by polishing with 3 µm and 1 µm diamond suspensions (using water-free lubricants). The prepared coupons were analyzed by XRD to check the structure and get a coupon background for the post-exposure analysis. The results can be seen in Figure 11.

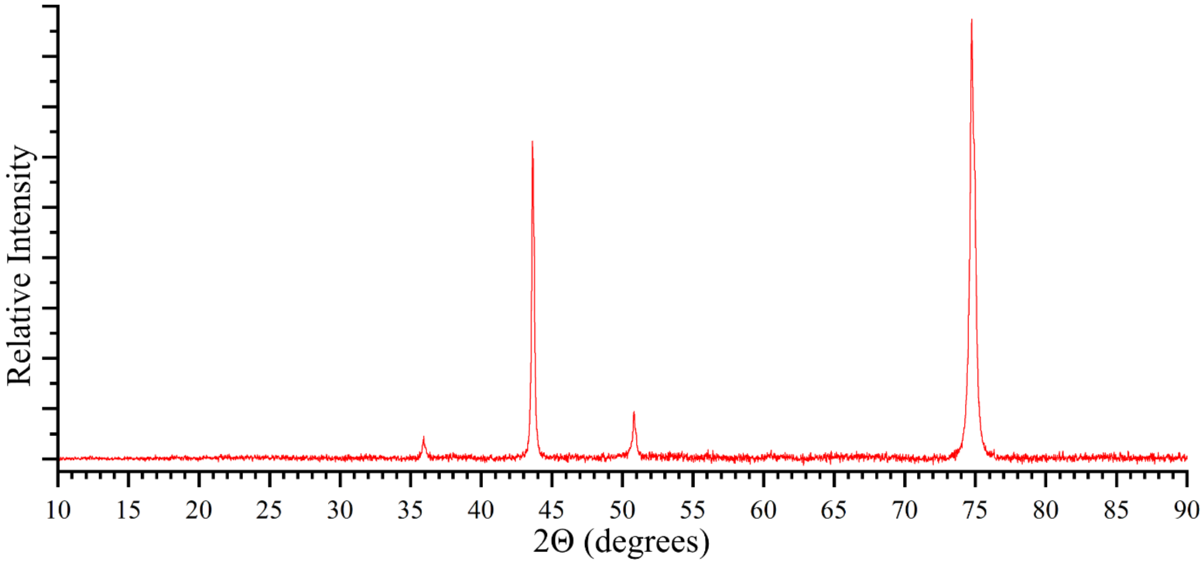

Figure 11: XRD pattern of the unexposed coupon used in the confirmation experiments.

The coupons were laid flat in cylindrical alumina crucibles with their polished sides facing up. In-house synthesized Cs_2MoO_4 powders were loaded in the crucibles until the powders covered the whole coupon surface. The crucibles were placed in an alumina boat for the ease of loading/unloading from the tube furnace. The tube furnace was heated up with the same heating rate as capsule exposures: 2 °C/min. Exposure duration was also the same at 168 h. In order to get the chemical conditions same as the capsule, the exposure was run under Ar gas flow of 80-110 ml/min. After 168 h was complete, the setup was let cool down to room temperature before removing it from the furnace. The leftover powders were collected and stored, and the coupons were put into XRD analysis. The coupons were later embedded in Bakelite for cross-section analysis; 2 mm from the embedded samples were cut to avoid edge-effects during investigation. The cut surfaces were then grinded and polished; first with SiC until size #4000, then with 3 µm and 1 µm diamond suspensions. During grinding with SiC paper, ethanol was used for cooling to avoid moisture, and water-free lubricants were used during polishing. For the same reason, the coupons and later prepared cross-sections were all stored in vacuum-sealed bags and only shortly removed for analysis or preparation steps.

4.5. Cross-section Preparation

The geometry and complexity of the capsule made the cross-section preparation step different than conventional methods. However, the aim was the same; to prepare a surface that correctly represents the sample. Several considerations have been taken into account due to different components of the capsule. As seen in Figure 12, the cross-section consists of multiple surfaces, which exhibit different problems and require different considerations. While the alloy (15-15Ti) and its corrosion products (oxide layers) work in agreement with the waterproof SiC grinding papers, Pb is soft and can smear during grinding/polishing. Similarly, Cs_2MoO_4 can smear as it is in powder form; moreover, Cs_2MoO_4 is a moisture sensitive substance, along with its corrosion products. Therefore, the prepared surface needed protection from air and water (e.g., using an oil-cooled saw). Lastly, both molten Pb (after solidification) and Cs_2MoO_4 are expected to create cavities and empty spaces, which requires separate consideration. A simpler method would be to remove the capsule caps and remove the cladding tube (by melting the Pb), but this would hinder our ability to inspect the outer side of the tube, as it would temper with the solidified Pb and associated corrosion products. At the end, this thorough but intricate method allowed important information to remain within the cross-section.

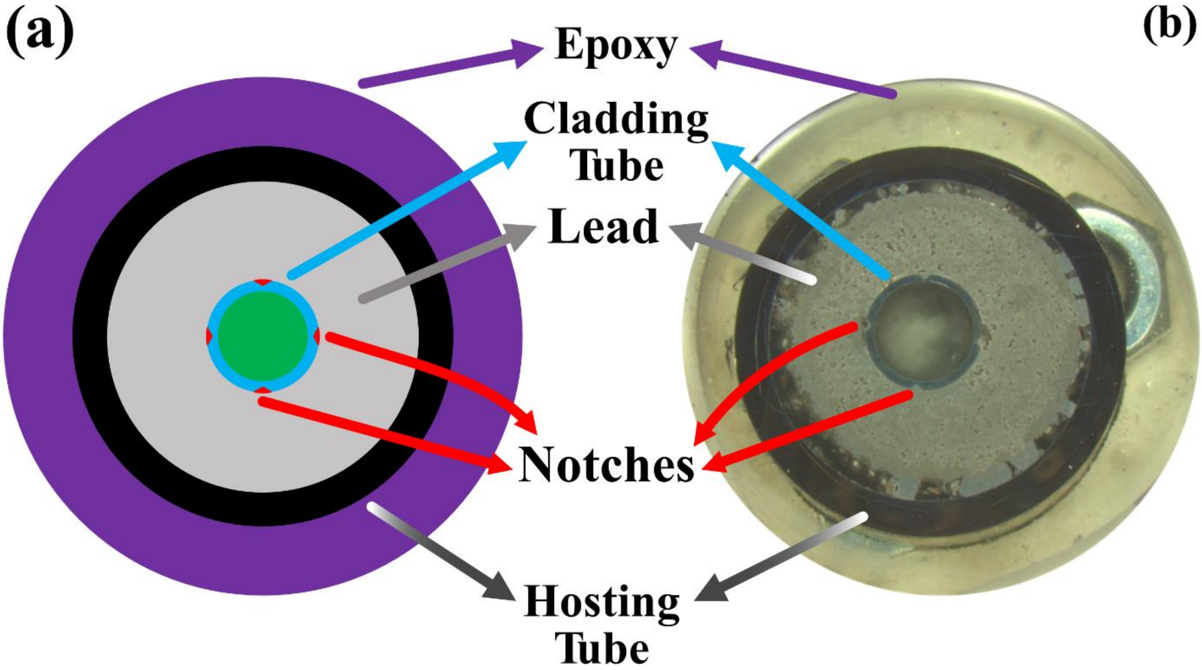

Figure 12: a) Schematic of the cross-section, b) Cross-section after an exposure (600 °C).

After exposures were completed, the capsules were left to cool down to room temperature. The first step was to cut off 8 mm from the top of the sample, with the intention of revealing the space that was housing the Pb, which is now heterogeneously solidified. Figure 13 shows the procedures, with the red-dashed line showing the cutting line for 8 mm cut. An oil-cooled saw was used for this step and onwards.

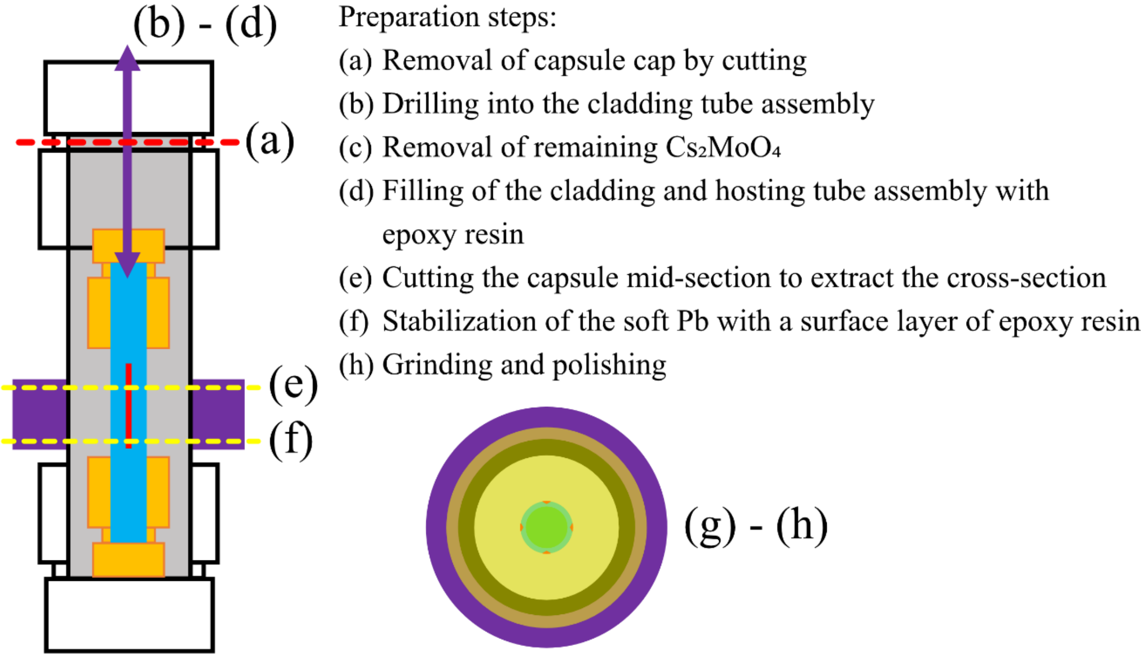

Preparation steps:
(a) Removal of capsule cap by cutting
(b) Drilling into the cladding tube assembly
(c) Removal of remaining Cs_2MoO_4
(d) Filling of the cladding and hosting tube assembly with epoxy resin
(e) Cutting the capsule mid-section to extract the cross-section
(f) Stabilization of the soft Pb with a surface layer of epoxy resin
(h) Grinding and polishing

Figure 13: Procedures for cross-section preparation.

The goal was to access the Pb housing, and the top of the cladding tube, and to drill a hole on it. As the cladding tube was holding Cs_2MoO_4, the powder had to be removed or stabilized to be able to make a cut from the middle (as shown with yellow lines Figure 13-e and -f. A hole (Ø = 3-4 mm) was drilled to the top of the cladding tube caps, without coolant to avoid contamination. To remove the remaining Cs_2MoO_4, the capsule was simply turned upside down, no additional cleaning methods or chemical was used, again to avoid contamination. Later steps showed that this removed the bulk of the Cs_2MoO_4; however, small amounts of Cs_2MoO_4 adhered to the inner side of the cladding tube. The amount was not enough to cause major issues during grinding/polishing, but it was still visible on SEM images. Earlier iterations of cross-section preparation did not have this Cs_2MoO_4-removal, but instead skipped to the next step of epoxy injecting into the capsule. This approach yielded unwanted results as the remaining Cs_2MoO_4 caused major issues like smearing across the surface and expanding due to moisture adsorption. After Cs_2MoO_4 was removed, the epoxy was injected starting from the inside of the cladding tube, which overfilled and covered the voids made by solidified molten Pb, residing between outer side of cladding tube and inner side of hosting tube. The whole capsule was put inside a vacuum chamber to discharge remaining bubbles and excess air, ensuring a better filling for the voids.

The epoxy was let to cure according to manufacturer's instructions. A section of the capsule with approximately 1.5 cm was cut out, with an oil-cooled high-speed saw (Figure 13-e, -f). This section was chosen from the lower part of the capsule, aiming to reveal the notch geometry from the middle of its vertical length and allowing an investigation from the downward side. The freshly cut out section was once again embedded in epoxy and put into vacuum, to fill the remaining void and cavities, either leftover from the exposure or the cutting process. Before applying epoxy, 3-4 pieces of 4.8 mm thick steel pieces were placed underneath the cut out piece to elevate it. This ensured that the bottom side of the prepared sample would be covered completely with epoxy and the remaining miniscule amount of Cs_2MoO_4 would be coated with epoxy. More importantly, this conductive material enabled electrical conductivity with the bottom and the embedded sample inside. Due to the low electrical conductivity of the epoxy, extra measures were needed for later SEM investigation stages.

The epoxy was again let to cure according to manufacturer's instructions. The excess epoxy on the top was cut and manually grinded to reveal the surface. For automatic grinding, SiC papers of different numbers were used until down to #4000 size, along with ethanol cooling. Afterwards, the surfaces were polished with 3 µm and 1 µm diamond suspensions, along with water-free lubricant. Even though bulk of the Cs_2MoO_4 was already removed, the integrity of the remaining layers and leftover powders were protected from excess humidity. In between every step, the surfaces of the samples were cleaned with ethanol, and additionally with acetone for grinding-polishing stage. The samples were then stored in a desiccator with P_2O_5 desiccant to protect the cross-sections from humidity, except when removed for analysis.

4.6. Cs_2MoO_4 Synthesis

Capsule exposures were conducted with off-the-shelf Cs_2MoO_4 (4.1). Confirmation experiments instead used in-house synthesized Cs_2MoO_4 powders. The synthesis method was based on Wallez et. al [60]. Cs_2CO_3 and MoO_3 were mixed in stoichiometric ratio. The mixed precursor powders were mortared to avoid clumps and ensure good mixture. The precursor powders were then transferred to an alumina boat. The synthesis followed Equation 7 below.

$$Cs_2CO_3(s) + MoO_3(s) \rightarrow Cs_2MoO_4(s) + CO_2(g) \uparrow \qquad (7)$$

For the synthesis, a tube furnace with constant O_2 flow (80 ml/min) at 700 °C was used, for 24 hours. The intermediate grinding step was skipped to avoid excess moisture in the Cs_2MoO_4 powder, as this substance is known to be highly hydrophilic. Due to the same reason, the powders were stored in a desiccator with P_2O_5 (moisture absorbing agent), unless they were in use.

4.7. Characterization Methods

A Zeiss (Model: Vert.A1) optical microscope was used for imaging, and a Nikon SMZ800 optical microscope (coupled with "DFK NME33UX264" camera and "IC Measure 2.0" software).

X-ray Diffraction (XRD) analysis was performed using a Brukar D8 Discover with CuKα (λ=1.54 Å) source, between 10° and 90° for 2θ.

For Scanning Electron Microscopy (SEM) and Energy-dispersive X-ray Spectroscopy (EDX) analysis; Phenom ProX Desktop SEM from FEI, Quanta 200 ESEM FEG from FEI or JEOL JSM-7800F Prime was used. The accelerating voltage for imaging and EDX spectra was changing between 15 kV to 25 kV. For the interpretation of EDX quantification, Aztec (Oxford Instruments, UK) software was used.

EDX analysis for this study was particularly difficult due to the overlap of energy levels. The problems encountered during EDX are complex and multifaceted intricate and have multiple features connected to it. Therefore, the methods used during the analysis require their own explanations. We hope that the information here helps whoever conducts similar studies in the future and runs into the same unique problems. As explained before, the capsule exposures have both Pb and Mo in the same setup. Even though the cladding tube assembly separates the chemicals, the aim of the setup is to induce a breach and their (Pb & Mo) mixture during a breach is all but inevitable. In fact, this is a desirable outcome of the thesis work. The problem first arises from the X-ray emission energies of Pb and Mo. Mo-Lα_1 and Pb-Mα_1 have less than 0.1 keV difference between each other [77]. As these are the primary (or strongest) peaks of the respective elements, it becomes increasingly difficult to differentiate the elements using the EDX spectra between 2 to 3 keV, even for the qualification. Where possible, the wider peak shape created due to the presence of Mo was used to qualify it. On the other hand, for a good balance between spectra range and good spatial resolution, it is recommended to stay within <15 keV range. For the Pb's case, the Pb-Lα_1 and Pb-Lβ_1 are still strong peaks that are ~10.5 keV and ~12.6 keV, respectively. Therefore, 15 keV accelerating voltage could still be good for qualifying Pb, but the signal strength would be lower than desired. Mo-Kα (~17.4 keV) and Mo-Kβ (~19.6 keV) have the same issue if the accelerating voltage were increased to 20 keV. As a result, 25 keV was selected as the most used accelerating voltage of this study. With this, it was still difficult, but not impossible to differentiate between Mo and Pb. However, the problem of electron penetration depth has become serious with the 25 keV, as the so-called "tear shape" of the electron signal depth increased with the accelerating voltage, severely decreasing the accuracy or the spatial resolution of the EDX analysis. A visual illustration of this increasing interaction volume can be seen in Figure 14.

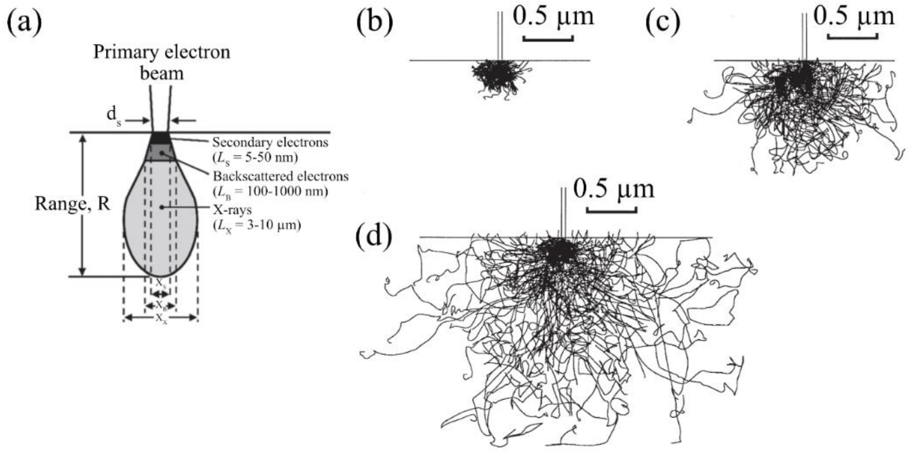

Figure 14: (a) Schematic of the "tear shape"; depicting interaction volume of depth, R; escape and information depths, *L*; and lateral probe size, *x*; for different signal types that are widely used in SEM-EDX analysis; adapted from [78]. Interaction volume in iron as function of beam energy of (b) 10 keV, (c) 20 keV, (d) 30 keV, where electron trajectories were simulated by Monte Carlo, adapted from [79].

Due to the proportional increase of interaction volume with accelerating volume, EDX point analysis was deemed accurate to only 1 µm. On some locations, this effect was seen to conflict the thermodynamics of the sample. Special considerations were made according to low resolution and difficulties to avoid smearing of components during cross-section preparation. On other locations, features of corrosion scales smaller than 1 µm were analyzed but the results were not completely reliable. In future studies, the voltage is planned to be increased to 30 keV, to get more accurate quantification of Pb and Mo mixtures, with the aim of defining their compounds, where spatial resolution will allow.

5. Results

5.1. Visual Inspection and Capsule Performance

The visual inspection of the capsules after 168 h exposure can be seen in Figure 15. The effect of increasing temperature can be seen easily, as Alloy 316 oxidizes rapidly at temperatures above 800 °C. The hosting capsule, which is made from Alloy 316, suffers visually and measurably. Here the outside of the capsule is exposed to furnace air as the corrosive environment. This resulted in spalling scales and nodular oxides which agrees with reported literature observations [80].

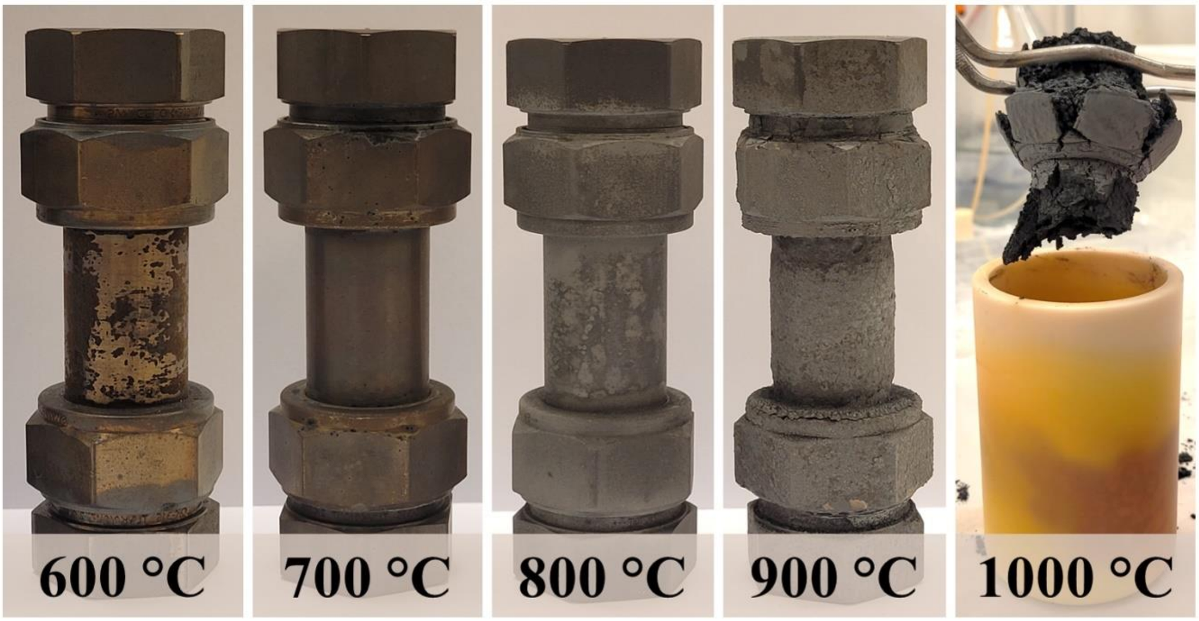

Figure 15: Assembled capsules after 168 h exposure in laboratory air at different temperatures.

The damage to the capsules reached a critical point at 1000 °C and resulted in catastrophic failure before 168 h have been reached, as seen in Figure 15. Firstly, exposure was conducted at 1000 °C, where the duration was limited to 52 h. This time limit was not set arbitrarily, but instead it was due to the limitations of the experimental setup. As it was mentioned before (4.3), the capsules were placed inside another vessel to secure a thermocouple and protect the furnace's refractory lining. At 1000 °C and 52 h exposure, this protective vessel was observed to be failing at the 48 h mark, which prompted an early cancellation of the exposure. Later, the 1000 °C exposure was conducted with alumina crucibles, with 168 h duration. The alumina crucibles were certainly a better protective vessel replacement, but the capsule suffered a catastrophic failure, as seen in Figure 15. The upper section of the 1000 °C exposure capsule was removed by hand, applying a small amount of force. Meanwhile, the alumina crucible served its intended purpose, and did an excellent job of protecting the furnace lining, while sacrificing itself. The color change around the alumina crucible indicates that it reacted with the contents of the capsule. In the current state of the capsule, no systematic investigation could be conducted. Therefore, the exposure at 1000 °C and 168 h was excluded from the further results. The experiment did help us understand the limits of the capsule, which is still invaluable to future experimental campaigns. For the detailed examination, only the capsules of 600 °C to 900 °C (168 h) and 1000 °C (52 h) exposures were taken into account.

5.2. Optical Microscopy Analysis and Thinning Effect

On both the hosting tube and the cladding tube, a thinning effect was observed. The thinning effect was investigated with optical microscopy to explore the severity of the situation.

5.2.1. Thinning of Hosting Tube

The prepared cross-sections showed a decrease of the hosting tube thickness proportional to the increasing temperature, predominantly at the lead exposed side (see Table 4). The optical microscopy measurements were done taking only metallic reflective parts into account. The oxide scales that are non-reflective were measured separately. Six individual sites were used for the measurements, taking the thickest and thinnest parts into account, given as ranges.

Table 4: Hosting Tube layer thickness values.

Temperature (°C)	Time (h)	Remaining Hosting Tube Thickness (mm)	Internal Oxidation (µm)	Outer Inhomogeneous Layer (µm)
600	168	1.92 - 2.02	5 - 18	4.2 - 6.1
700	168	1.89 - 1.90	x	50 - 64
800	168	1.82 - 1.88	x	216 - 277
900	168	1.36 - 1.72	15 - 32	80 - 114
1000	52	1.8 - 1.94	37 - 63	82 - 120

The hosting tubes in contact to molten Pb showed not only different scale thicknesses but also different scale appearances with increasing temperatures. Therefore, Table 4 also presents distinguishable corrosion layers observed on molten Pb exposed side of the hosting tubes, with their respective images in Figure 16.

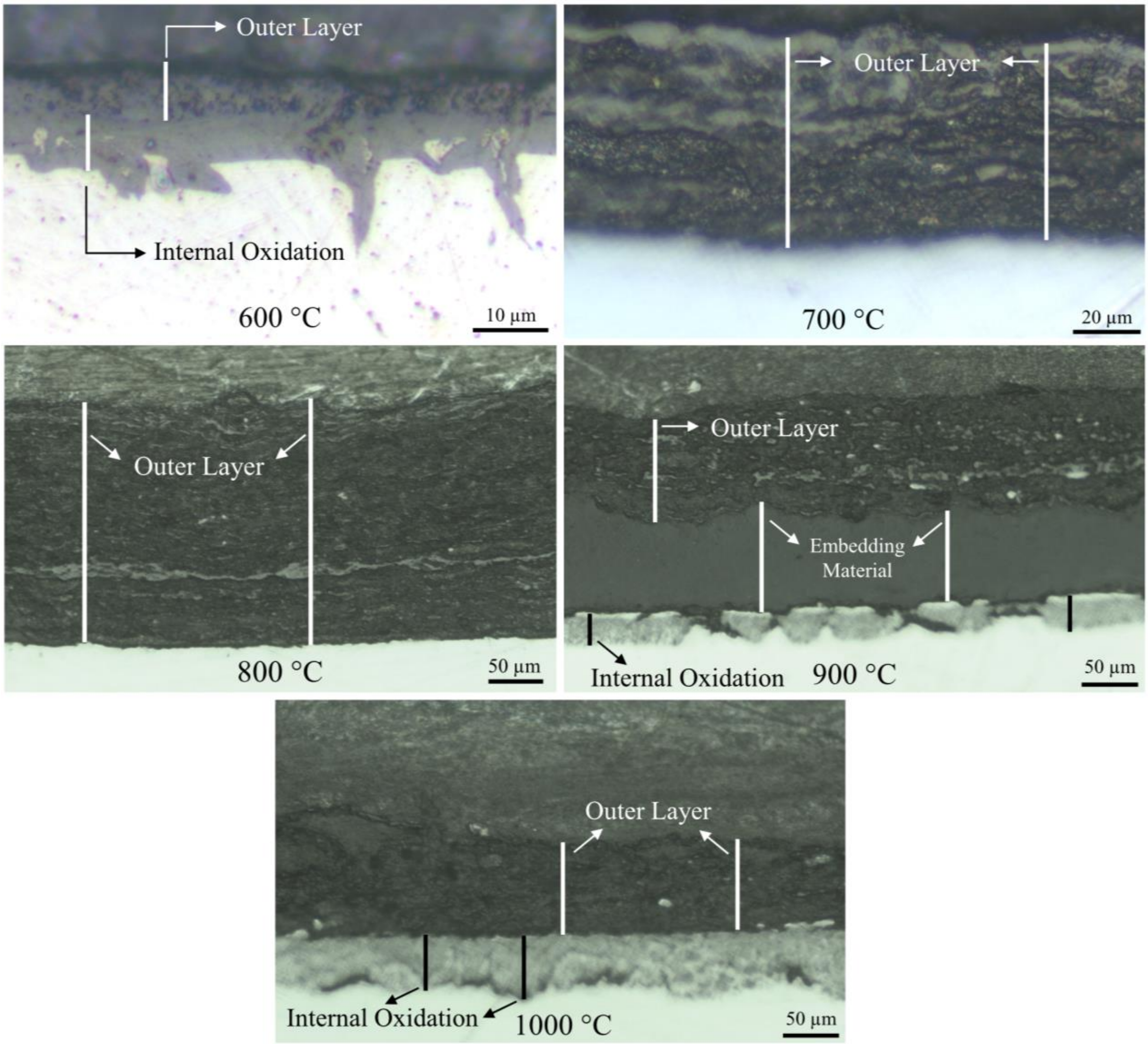

Figure 16: Representative optical microscopy (taken in Bright Field mode) images from Pb-side of hosting tubes (bottom side in images), all exposures for 168 h, except for 1000 °C (52 h).

5.2.2. Thinning of Cladding Tube

The 15-15Ti cladding tubes also suffered from a thickness loss that got more severe with increasing temperature. This wall thickness loss was investigated for 600, 700, 800, 900 °C (168 h) and 1000 °C (52 h) exposures. The tube was in contact with molten Pb on the outside and with Cs_2MoO_4 on the inside. Similar to the hosting tube, optical microscopy was used to determine this thinning effect through the cross-sections. Only free surfaces were considered as the drilled areas were already thinned (see Figure 9). ImageJ™ open-source image analysis software was used to measure the thicknesses. At least 35 thickness measurements from three different areas of the cross-section were used for the comparison in Figure 17.

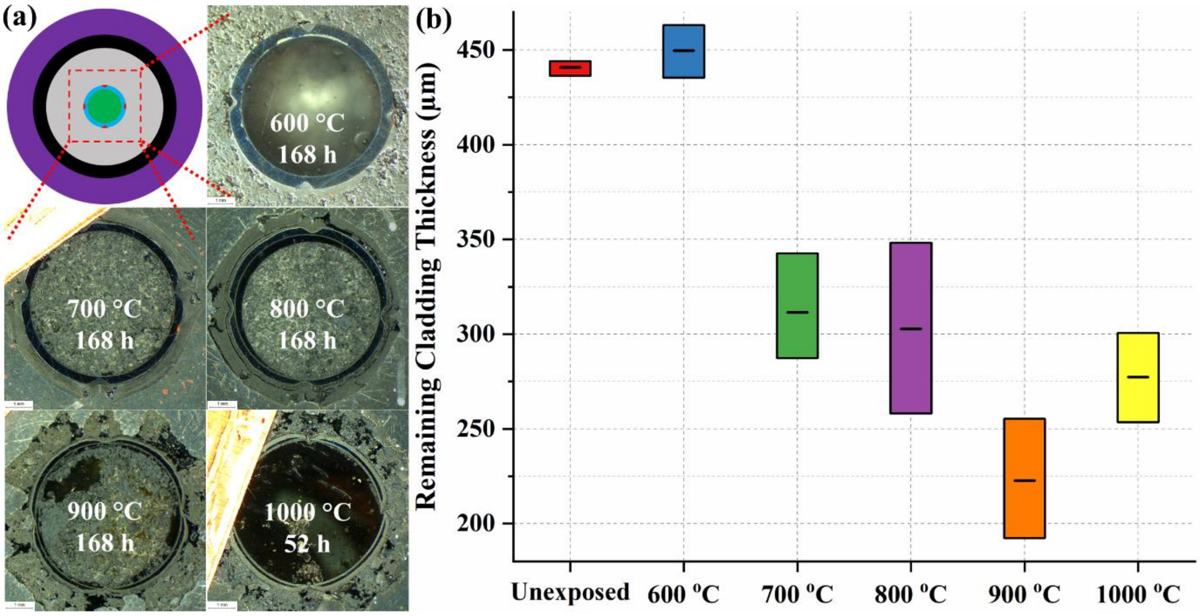

Figure 17: (a) Optical microscopy images of cladding cross-sections, with the schematic on top left. (b) Diagram for remaining cladding tube wall-thickness values after 168 h of exposure; average, minimum, and maximum values are used. The thickness values for the cladding exposed at 1000 °C are for 52 h.

All exposures, other than 600 °C, resulted in significant decrease in wall thickness. A slight increase of wall thickness was seen on the exposure at 600 °C. This increase might originate from the growth of corrosion layers or variations in the tube production margins. However, at 900 °C the remaining cladding tube wall thickness reached an average of 175 µm, less than half of the original 450 µm. With increasing temperature, alloy loss values spread in a wider range; the min/max range of thickness measurements for 800 °C and 900 °C are higher due to different local progression of corrosion fronts. A wave-like structure was observed at some of the metal-scale interfaces. The cladding material thinning at 1000 °C was reported in Figure 17 after only 52 h of exposure, since 168 h resulted in a catastrophic cladding failure (see Figure 15).

5.3. SEM and EDX Analysis of Capsule Exposures

Cross-sections were prepared (4.4) and investigated thoroughly with SEM and EDX analysis. Due to the tubular shape of the fuel claddings, a cross-sectional analysis scheme fits well into this study. SEM is a relatively easy and accessible analysis method that can give insight into cross-sections, while the coupled EDX can be a powerful tool to collect elemental data. Here the initial analysis with morphological data and the elemental data will be presented categorically. This data will be reviewed and argued holistically later, in Chapter 6 (Discussion).

5.3.1. 600 °C, 168 Hour Exposure

5.3.1.1. Overview of Drilled Areas

As seen in Figure 18, no breach was observed after the 600 °C exposure for 168 h. The molten Pb and Cs_2MoO_4 corrosion scales here are completely isolated from each other and even at the center of the drilled areas, the corrosive species (molten Pb and Cs_2MoO_4) are not interacting. In the context of a breaching scenario, the situation here is not completely representative as the corrosive species have not made contact.

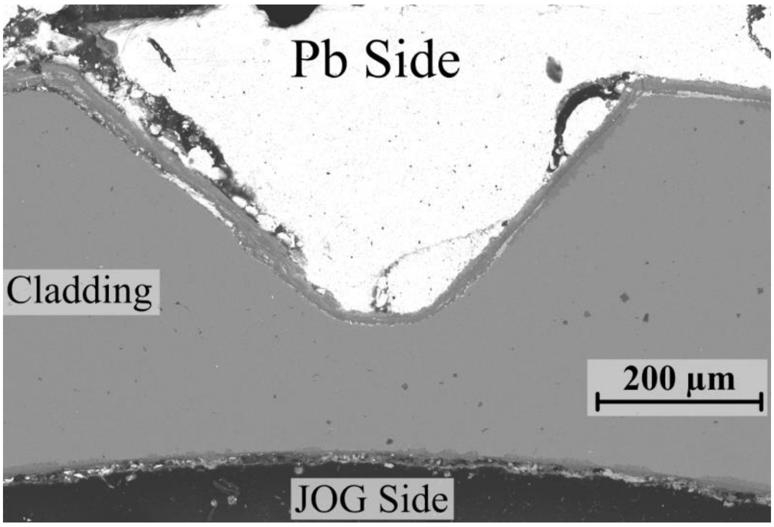

Figure 18: Center of a drilled area, after 600 °C, 168 h exposure (taken at 25 kV).

5.3.1.2. Delamination on Pb Side

In all the capsule exposures, a delamination effect has been observed, and it will be investigated in detail. Delamination is the result of the repeated detachment of the oxide scales that have formed as a result of impurity oxygen dissolved in molten Pb reacting with outer surface of the cladding tube.

Even though delamination was recognized as one of primary causes for loss of thickness, it was reported earlier (Figure 17) that 600 °C exposure suffered only localized thinning, and overall, the thickness was increased. Figure 18 supports this result as an outer scale is growing on the Pb side of the cladding surface. However, signs of delamination were still observed on this exposure. Here, delamination was limited to the notch areas, as shown in Figure 19. One of the drilled areas can be seen on Figure 19-b, in its entirety; with accompanying higher magnification images to focus on delamination. In both edges of the drilled area (where drilled areas converge with free surfaces) cracks can be seen. Similar cracks have been observed on other exposures too, due to growth stresses concentrating on these intersections. These will be discussed later in depth in the Discussion section. Figure 19-a shows the surface transitioning to free surface (from the drilled area), with a simultaneous and drastic structure change of the oxide scale. On the right side (Figure 19-a), the oxide scale can be seen detached from the cladding; while on the left side, a double oxide scale still remains attached to the cladding. Figure 19-c shows a higher magnification image of the detached scale (image tilted counter-clockwise), where delamination has begun. Molten Pb wetted the cracks successfully and managed to wet and detach the metal-oxide interface, resulting in delaminated layers, creating more cracks near the center of the same drilled area. More molten Pb can be seen between the delaminated layers and the cladding, indicating that if the exposure duration were increased, the process would repeat itself, resulting in significant damage to the drilled area. In conclusion, a clear difference of corrosion process on free surfaces and drilled areas is seen. In an in-pile condition, the same comparison between free surfaces and drilled areas could be made for cladding tubes that are undamaged (freshly installed) and damaged (irradiation, mechanical damage by creep etc.), respectively. It should be pointed out that only one compact delamination layer was observed for 600 °C in contrast to the following chapters.

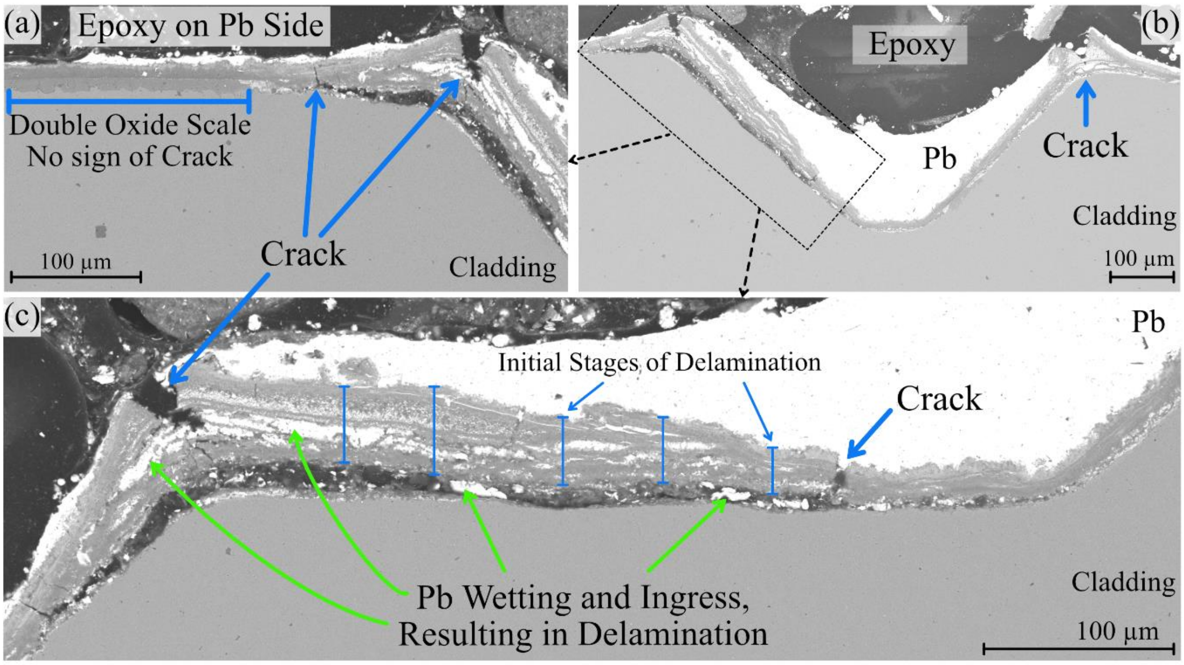

Figure 19: BSE image of delamination starting on the intersection of drilled areas and free surfaces, taken with JEOL at 25 kV, exposure at 600 °C and for 168 h.

5.3.1.3. Internal Oxidation by Molten Pb

Figure 20 shows the interface between the alloy and molten Pb, from two different locations, both far from (and therefore unaffected by) drilled areas. The images taken here reveal similar morphologies and scales for corrosion induced by molten Pb. Three different scales can be observed. Starting from the alloy side, we see an inward-growing scale, most likely internal oxidation clearly visible by the darker Z-contrast in BSE mode compared to the underlying alloy region due to its different contrast, marked Layer 1 in Figure 20. The layer is penetrated by long and thin grain boundaries growing towards the alloy, in a darker color, indicating a lighter phase with a higher oxygen content. Outside of the alloy, two different outer oxide scales can be observed; Layer 2 that is adhered to the inward-growing scale and another Layer 3 that is in contact with the solidified Pb. Layer 2 has a uniform morphology, a feature that is sought after on a protective scale. On the other hand, Layer 3 is more heterogenous in its structure, but consistent throughout the sample; although, the thickness of the layer is still heterogenous. Lamella-like growth (perpendicular to the alloy circumference) can be observed. The compositions of Layer 2 and Layer 3 hold important information regarding the oxygen and cation transfer to and from the alloy, respectively. The lack of thin and small (<1 µm) features made the investigation more consistent and thorough.

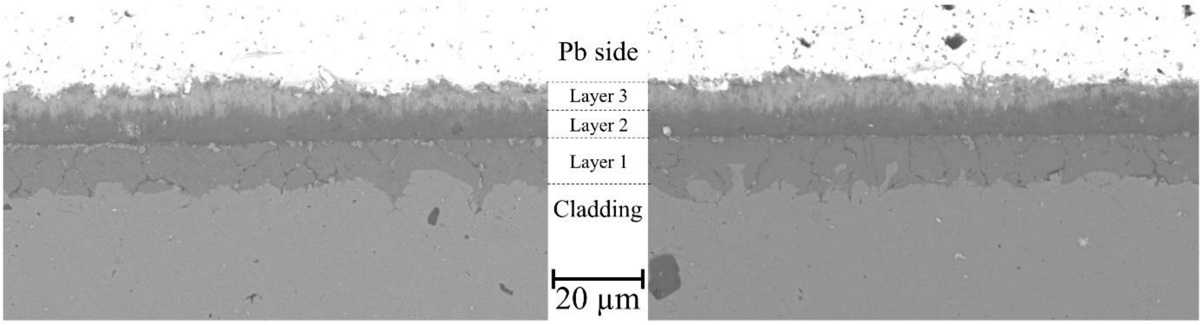

Figure 20: BSE images of 600 °C, 168 h exposure. From two different locations of free surfaces, on Pb side.

The thickness of the inner oxide scale (Layer 1 in Figure 20) was found to be 6 to 14 µm according to Figure 21. The bulk of the inner oxide scale was investigated mainly with EDX point analysis and it was determined as a spinel layer, consistent with the literature findings close to these experimental parameters [8]. The composition of this scale was identified from different locations and was determined as; 45-54 at.% O, 19-25 at.% Fe, 11-15 at.% Cr, 8-15 at.% Ni. The inner oxide scale consists of only one type of microstructure, but it hosts more irregular features inside. Namely, chromium oxide decorated grain boundaries and particles with brighter backscatter contrast; pointing towards Ni or Pb enrichment. The direction of the grain boundaries indicates that they are growing from outside the alloy and travelling to the inside. Coupling this with their darker backscatter contrast (lighter phase), these branches are possibly the main diffusion path for oxygen. However, the exact composition could not be identified separately due to the low spatial resolution of the EDX beam.

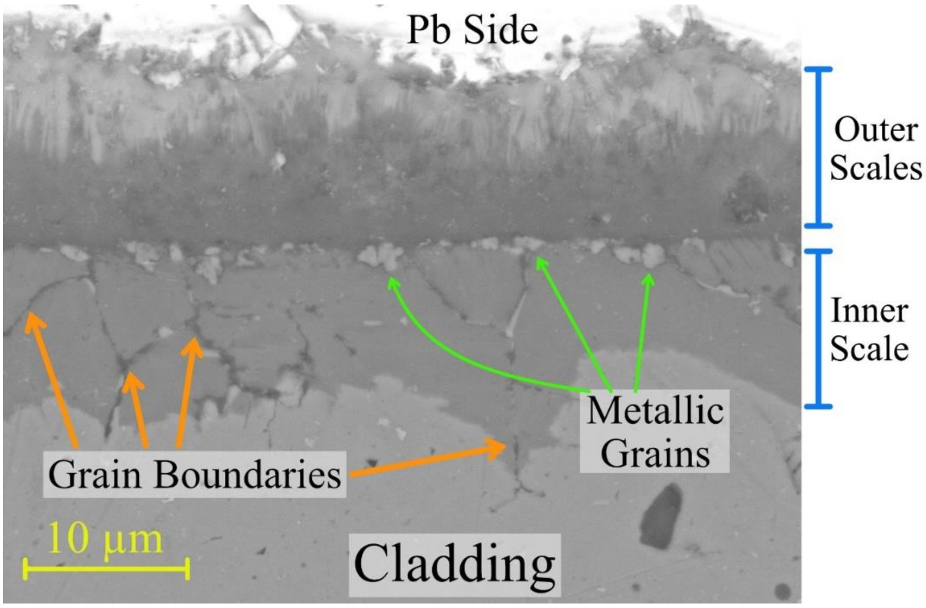

Figure 21: BSE image of 600 °C, 168 h exposure, Pb side on free surface.

The majority of the metallic grains were located between the inner oxide scale and outer oxide scale (Layer 1 and 2 in Figure 20, respectively). The compositions of the marked grains in Figure 21 are 45-46 at.% Fe, 17-19 at.% Cr, 29-31 at.% Ni. Compared to the initial alloy, a clear Ni enrichment is seen beneath the outer scale, which is due to Fe depletion caused by the outer Fe-rich oxide scale growth. The outer-growing oxide scale on top of these metallic grains has Fe-oxide as its main phase (62-68 at.% O, 27-34 at. Fe, 2-4 at.% Cr, 0.2-0.7 at.% Ni, 0.4-0.6 at.% Pb, 0.2-0.4 at.% Si). Due to its high concentration, and thermodynamically stable FeO has formed here with the reaction between Fe in the alloy and the dissolved O in the molten Pb. Cr has remained in the alloy and instead chose to react with the O that has diffused through the outer scale.

5.3.1.4. Corrosion on Cs_2MoO_4 Side

Corrosion by Cs_2MoO_4 was not affected by the molten Pb as none of the drilled areas showed any breach. Therefore, the chemical aspect of the corrosion on the JOG side of the cladding is only between a concave 15-15Ti surface and Cs_2MoO_4 powder. Since the cladding tube assembly was sealed in Ar, no excess oxygen but impurities were present. Here the corrosion scales showed a double oxide scale behavior, similar to the Pb side of the same exposure. As seen in Figure 22, the double scale had a comparable structure on different locations. While the outer scale is homogeneous, the inner scale is not. The brighter spots in between oxides (darker spots) indicate that the inner scale is not consistent in structure and spots of alloy that have not been oxidized remained between oxides.

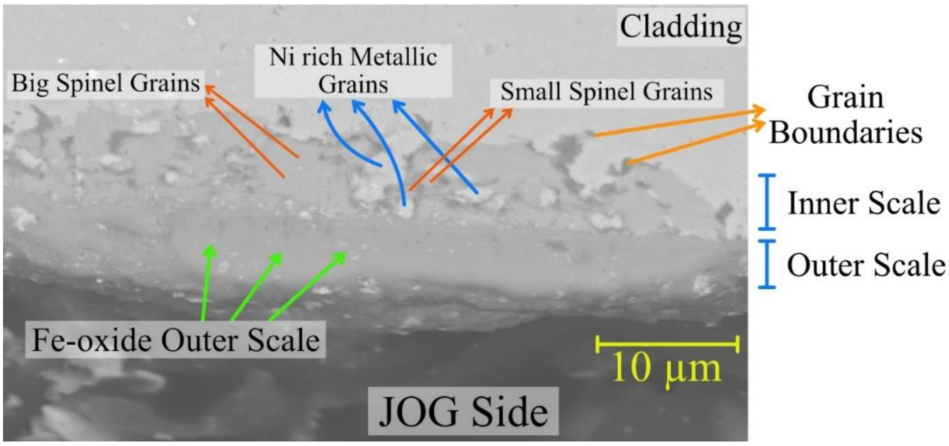

Figure 22: BSE image of 600 °C, 168 h exposure. Images from JOG-side presented from different locations of the cross-section.

The outer scale had irregular bright spots where Pb signal was present on EDX spectra, a common situation due to Pb smearing during cross-section preparation. It was established before that the cladding tube preserved its integrity, eliminating the possibility of Pb penetration during exposure. The outer scale (~5 µm) was investigated to discover a FeO scale with small amounts of Cr, Si and Mn. The EDX point analysis showed a composition of 48±1 at.% Fe and 50 at.% O (1 at.% Cr, 0.2 at.% Si, 0.3-0.4 at.% Mn).

The inner scale is 3-8 µm in thickness. The oxidized and metallic parts have remained in contact. The darker spots of oxidation are a mixed spinel with Fe, Cr and Ni. The oxygen percentage (44-49 at.%) of the spinel scale was similar in different locations, with no correlation between composition and distance to Cs_2MoO_4/cladding interface. However, the ratio of Fe, Cr and Ni is different between the oxidized grains. The bigger grains of spinel had ~50% more Ni compared to their smaller counterparts (12 at.% to 7±1 at.%). These more heterogeneous areas were a mixture of smaller spinel grains, oxidized grain boundaries (with darker contrast, and due to higher oxygen content) and metallic grains (as indicated by their lighter contrast). The Fe percentage (22-26 at.%) was similar on all of them, with variations on Cr (14-21 at.%).

An array of metallic grains remained inside the inner scale, which was otherwise mostly oxidized. Almost all boundaries of the metallic grains were covered by lighter elements, indicating that oxygen is more concentrated in these areas, compared to the spinel grains. The composition of the metallic grains correlates the results from the oxide grains. Compared to the initial alloy, 10 at.% Fe was lost in several locations; while Ni was highly enriched in all, as much as 50% in some locations. The Fe depletion is expected as the outer scale is made up of FeO, whose Fe would be supplied by the internal oxidation scale. As the remaining main alloy components, Cr and Ni have become enriched. Ni is more enriched, which also correlates to the lower Ni amount in the spinel grains and that Cr has more affinity to oxygen in this temperature. Therefore, while some (yet) unoxidized spots remain, their composition was still influenced.

5.3.2. 700 °C, 168 Hour Exposure

5.3.2.1. Overview of Drilled Areas

The exposure at this temperature did not show signs of cladding breach on any of the drilled areas. Compared to 600 °C, the severity of the corrosion process has increased dramatically. This was evident on Figure 17 due to the measured thickness loss, and the comparison of Figure 18 with Figure 23 supports this argument. Molten Pb and Cs_2MoO_4 are still ~90 µm apart from each other, even though delamination can be clearly seen in Figure 23-a. Multiple Ti(C,N) precipitates can also be observed, as it is a characteristic feature of this steel. Since no breach was observed, the results of outer (molten Pb) and inner (Cs_2MoO_4) side can be examined independently of each other.

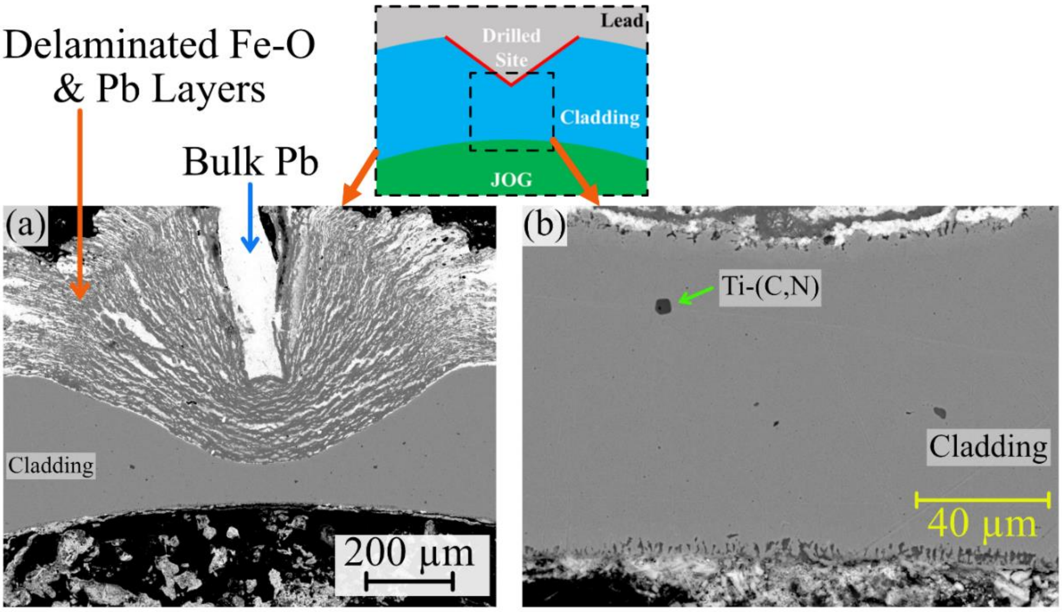

Figure 23: BSE images of two different drilled area centers of the exposure at 700 °C and 168 h (taken at 25 kV). (a) Low magnification image of a drilled area center, (b) higher magnification image of center of a different drilled area.

5.3.2.2. Delamination on Pb Side

700 °C shows us the most likely scenario for a delamination phenomenon, due to its proximity to accident conditions, and the fact that 600 °C did not show a meaningful delamination apart from the drilled area. As important as drilled areas are, they are mechanically altered locations with irregular shapes, and are therefore more prone to corrosive effects of molten Pb. In this exposure (700 °C, 168 h), the delamination can be seen both in drilled areas (Figure 23-a), and on free surface such as Figure 24.

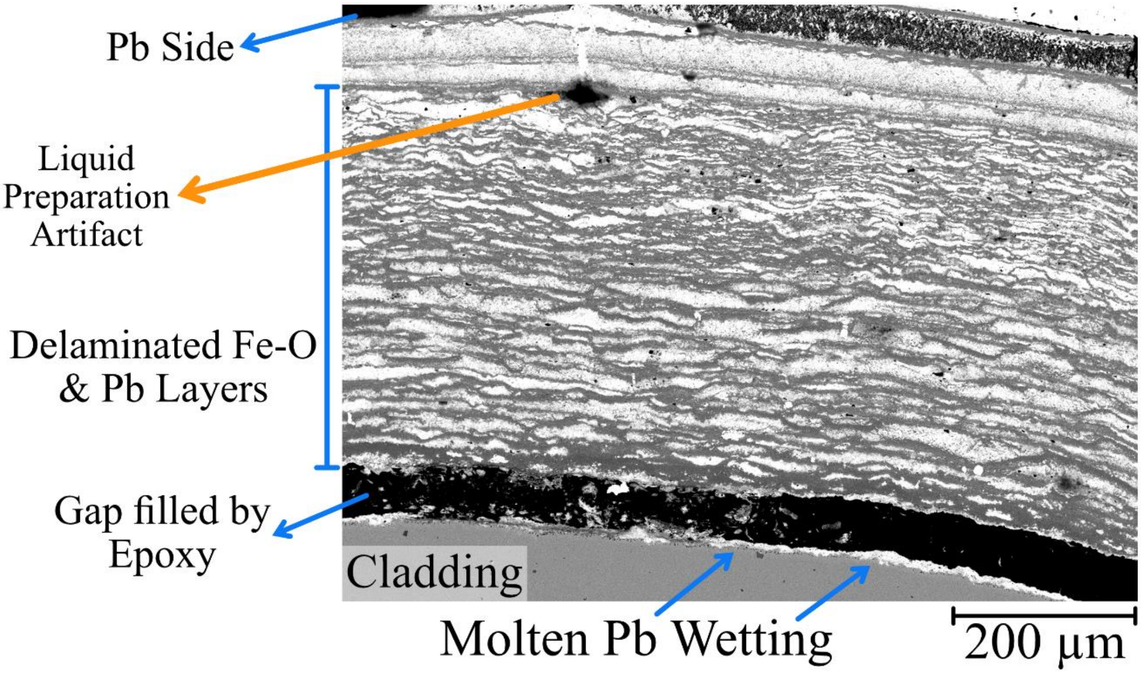

Figure 24: BSE image of free surface for the exposure at 700 °C and 168 h.

Delaminated layers were identified to be repeating layers of Pb and Fe-oxide. On Figure 25, an EDX map of the free surface is presented, where delaminated layers and remaining alloy can be seen. Delaminated layers were separated from the alloy during solidification, causing a gap to appear, which was later filled with epoxy during cross-section preparation. On top of the epoxy gap, Fe, O, and Pb maps can be used to determine that Fe and O are together, while Pb is located in between; confirming the repeating delaminated layers. Ni is following the Pb layer pattern, with highest enrichment at the alloy-Pb interface, pointing towards a metallic dissolution phenomenon. Cr map indicates that it was removed alongside Fe and O; however, more detailed quantification is needed to determine how much. EDX point analysis made on 4 different locations of the Fe-oxide component of the delaminated layers revealed a composition of 60-62 at.% O, 28-33 at.% Fe (3-6 at.% Cr, 2-4 at.% Ni, 0.3-1.8 at.% Pb).

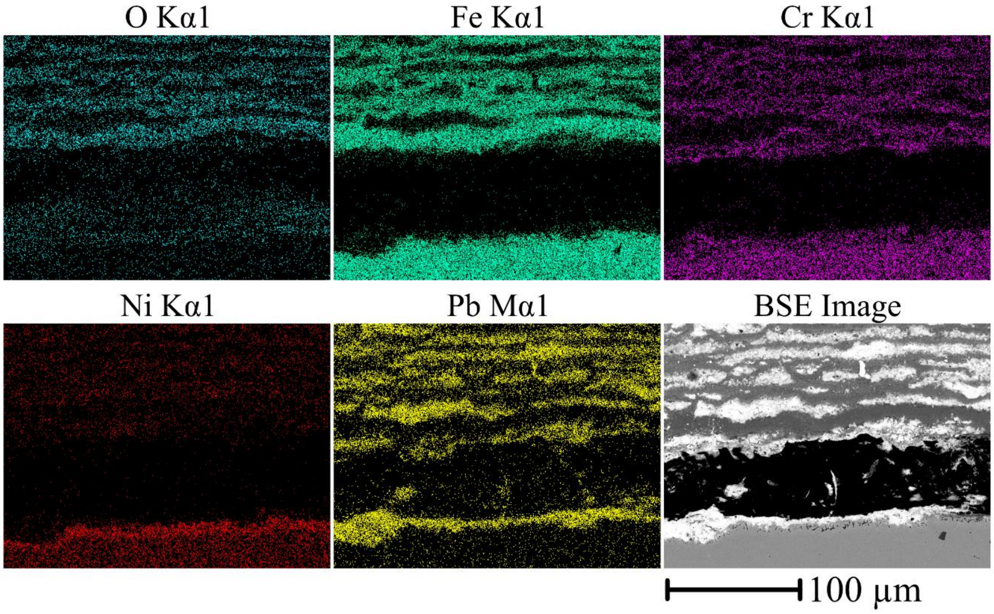

Figure 25: BSE image and the EDX map of a free surface location where alloy and delaminated layers are separated by epoxy (black area). Exposure at 700 °C, 168 h. Same scale for all images.

5.3.2.3. Internal Oxidation by Molten Pb

The cross-section for this exposure did not allow for an extensive investigation of internal oxidation scale caused by molten Pb. Most of the surfaces were delaminated and stripped away, or they were covered by solidified Pb as seen in Figure 26. The remaining internal oxidation scale can be identified by the darker contrasted branch-like structures on the remaining alloy, all of whom reside below the solidified Pb. These dark branches were analyzed by EDX point analysis; 49 at.% O, 17 at.% Fe, 10-11 at.% Cr, 13-16 at.% Ni, 4-7 at.% Si (<1 at.% Mn, Ti, Cs, Mo, Pb). The internal oxidation behavior is similar to 600 °C. A mixed spinel composition with close amounts of Fe, Ni and Cr was observed; along with Ni enriched metallic grains between the oxidation branches (45 at.% Fe, 39 at.% Ni and 10 at.% Cr).

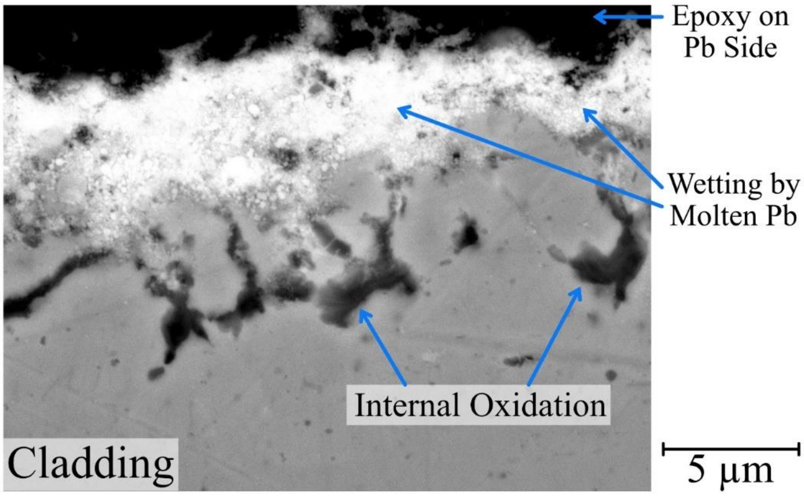

Figure 26: BSE image of a free surface location of exposure at 700 °C and 168 h, where solidified Pb and internal oxidation scale has remained adhered during cooling.

5.3.2.4. Corrosion on Cs_2MoO_4 Side

The corrosion caused by Cs_2MoO_4 on this exposure was a single corrosion scale, unlike the double scale of 600 °C exposure. The scale was not continuous, but instead the morphology shape resembles an intergranular oxidation path. The thickness of the scale varied between 3 to 6 µm, as seen in Figure 27. The oxide branches were Fe-Cr mixed spinel, with lower amounts of Ni and small amounts of Cs in them. No correlation between the elemental composition and the branch depth was found. The following elemental composition was found from 5 different points; 43-53 at.% O, 17-24 at.% Fe, 21-29 at.% Cr, 3-4 at.% Ni, 0.4-1 at.% Mo, 0.8-1.4 at.% Cs. Even though Mo peaks were identified and quantified, it was not possible to determine whether the source of Mo was the alloy or the Cs_2MoO_4.

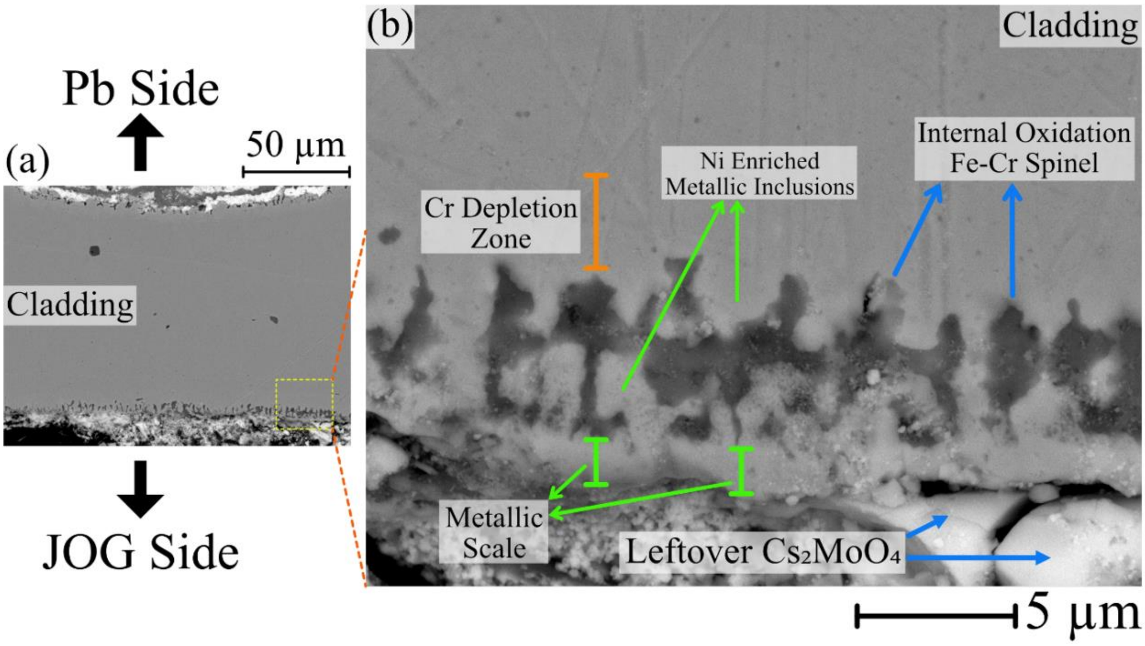

Figure 27: BSE image of 700 °C, 168 h exposure, JOG side. (a) Low magnification image of a drilled area with (b) marked, (b) Internal oxidation scale caused by Cs_2MoO_4.

The investigation of the metallic inclusions remaining between the branches revealed that their composition was akin to the original alloy. Cr was 10-12 at.%, while Fe and Ni were 66-71% and 16-17% (at %), respectively. Lower than 1 at.% Cs was also detected. Even though some Cr was lost from these metallic parts, the question of Cr and Fe supply to the oxide branches still remains. Therefore, the alloy beyond the internal oxidation scale was investigated. On Table 5, the results of EDX point analyses performed on the alloy adjacent to the internal oxidation branches can be seen. There was no correlation between the distance to the branches and the composition. The depletion of Cr in respect to initial cladding composition can be observed, with slight enrichment of Fe and Ni (see Table 2 for original composition). This is indicative of Cr supply (diffusion) from the alloy to internal oxides. Mn, Mo and Ti ratios are close to initial alloy, while Si is slightly lowered.

Table 5: Elemental composition of depleted alloy points (“Cr Depletion Zone” in Figure 27) in atomic percentage, with their respective distances from the internal oxidation scale. Taken with EDX point analysis at 25 kV, with JEOL.

Distance to Oxide Scale (µm)	Fe	Cr	Ni	Mo	Si	Mn	Ti
0.7	72.4	8.0	17.1	1.0	0.6	0.6	0.3
1.77	70.7	10.9	15.4	0.9	0.8	1.1	0.1
2.2	73.4	7.8	16.1	1.2	0.3	0.8	0.4
2.4	72.9	8.7	15.7	0.9	0.6	0.7	0.5
3.3	72.1	8.7	16.1	1.0	0.7	1.0	0.4

Another scale between the internal oxidation and Cs_2MoO_4 was found and marked in Figure 27. The contrast different on the BSE image indicates that this is a “sandwiched” metallic scale, which was further confirmed by the lack of O peak in EDX spectrums. Two point analyses were taken to reveal the following composition; 67 at.% Fe, 10-11 at.% Cr, 15-16 at.% Ni, 2-3 at.% Mo, 1-2 at.% Cs, 1-2 at.% Si, 1-2 at.% Mn. Even though this scale is in direct contact with Cs_2MoO_4, the composition is almost the same as the metallic inclusions between the internal oxidation branches.

5.3.3. 800 °C, 168 Hour Exposure

5.3.3.1. Overview of Drilled Areas

Overview images of 3 of the 4 drilled areas were investigated in order to examine the possible existence of a breach. Figure 28 shows SEM images, taken with backscatter electron detector, confirming the integrity of these areas.

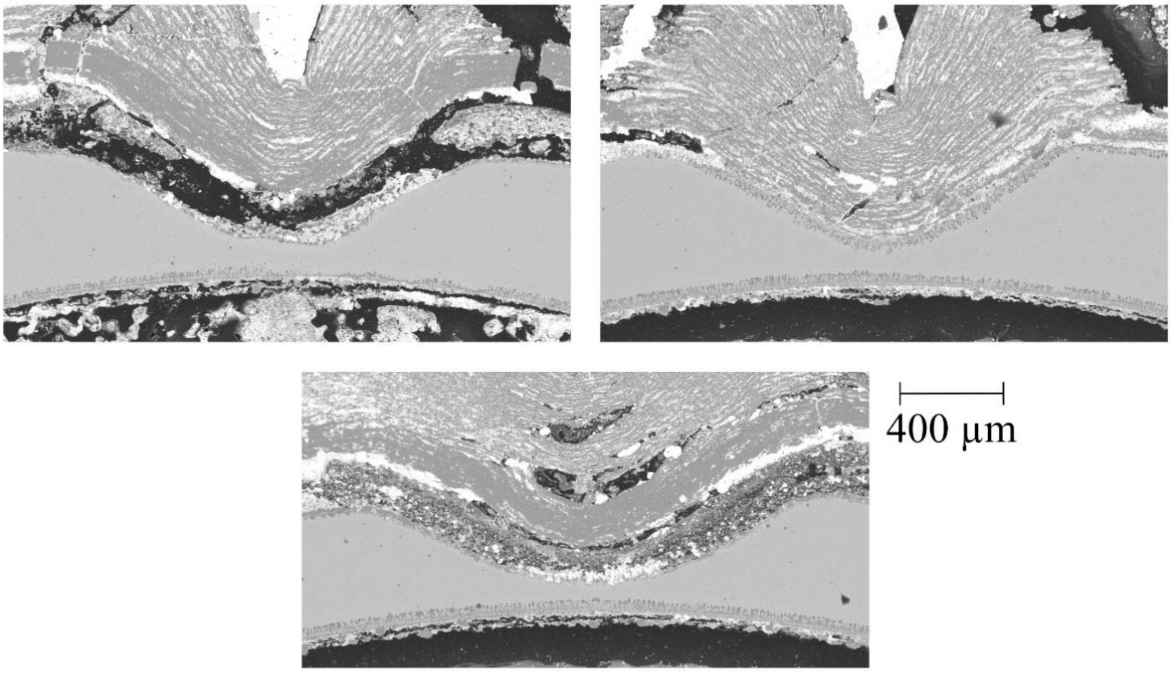

Figure 28: (a), (b), (c) BSE images of 3 out of 4 notches for the exposure at 800 °C - 168 h. Taken with JEOL at 25 kV. All images are on the same scale.

As seen in Figure 29, in the center of a drilled area, the corrosion zones of molten Pb and Cs_2MoO_4 came as close as 33 µm. Prior to exposure, the corrosive substances were ~170 µm apart (Figure 9). During exposure, a severe portion (~82%) of the alloy on drilled area was consumed, either getting leached, internally corroded, or lost to delamination on Pb-side. The darker colors in BSE imaging indicate a clear internal oxidation akin to free surfaces, which grows perpendicular to the circumference of the tube wall, in a branched structure.

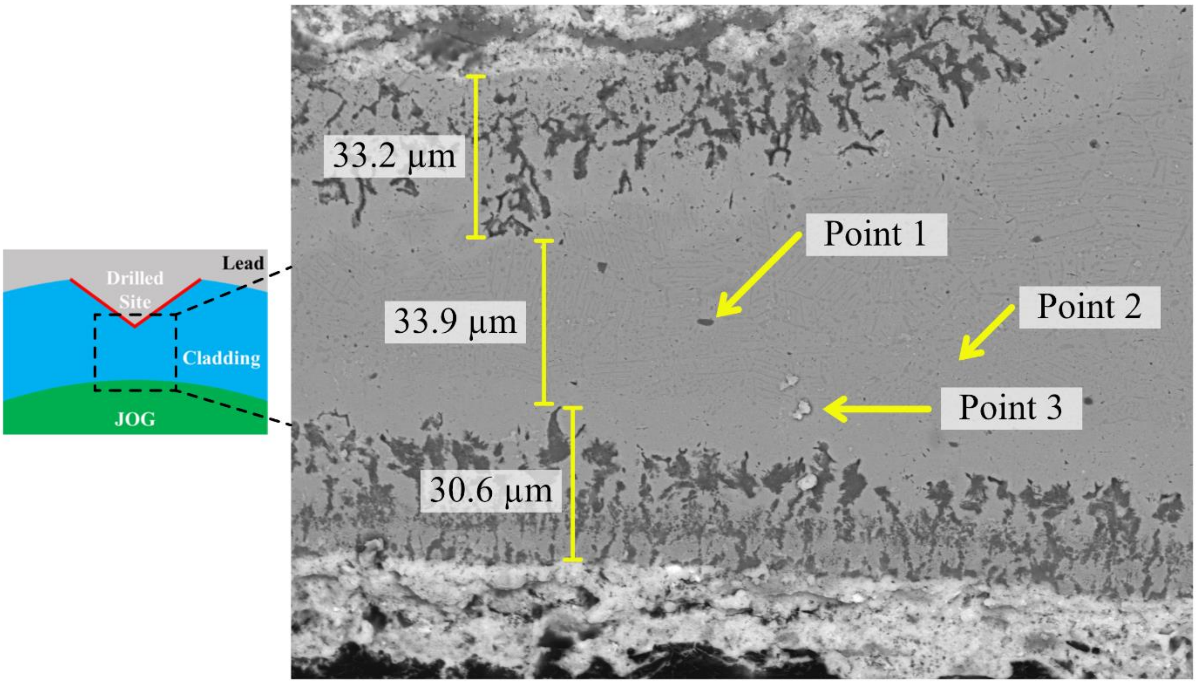

Figure 29: BSE image of a drilled area after 800 °C - 168 h exposure.

On Figure 29, three points of interest were investigated with EDX, at the center of the drilled area. Point 1 (~48 at.% C) was explored as a possible, characteristic Ti(C, N) precipitate of this cladding material [81]. However, the ~32 at.% Fe indicates a C-rich precipitate, most likely due to a manufacturing error during heat treatment step. The stretched defect shape appears to be an extrusion artifact of the cladding tube. This observation in itself is problematic for the performance of a cladding tube. No similar precipitate was observed, and this precipitate was not investigated further. Point 2 was used to cross-check the alloy composition, and no ingress of Mo or Cs was observed beyond corrosion scales. Point 3 showed Mo and Cs peaks with low amount of the elements themselves; with accompanying alloy component signals from underneath. The brighter-colored "smudge" on this point is likely due to Cs_2MoO_4 transport during the cross-section preparation (4.4).

Figure 30 shows an EDX map of the drilled area on Figure 29, with a focus of O, Fe, Cr, Ni and Pb. The effects of internal oxidation can be observed clearly on Cr map. Cr is one of the main components of the internal oxidation branches. Furthermore, Cr-depletion zone beneath the internal oxidation can be observed, on both Pb- and JOG-side. On the other hand, no depletion of Fe and Ni is observed on either side. While Ni enrichment was seen on Pb-side, consistent with the other exposure (600 °C and 700 °C).

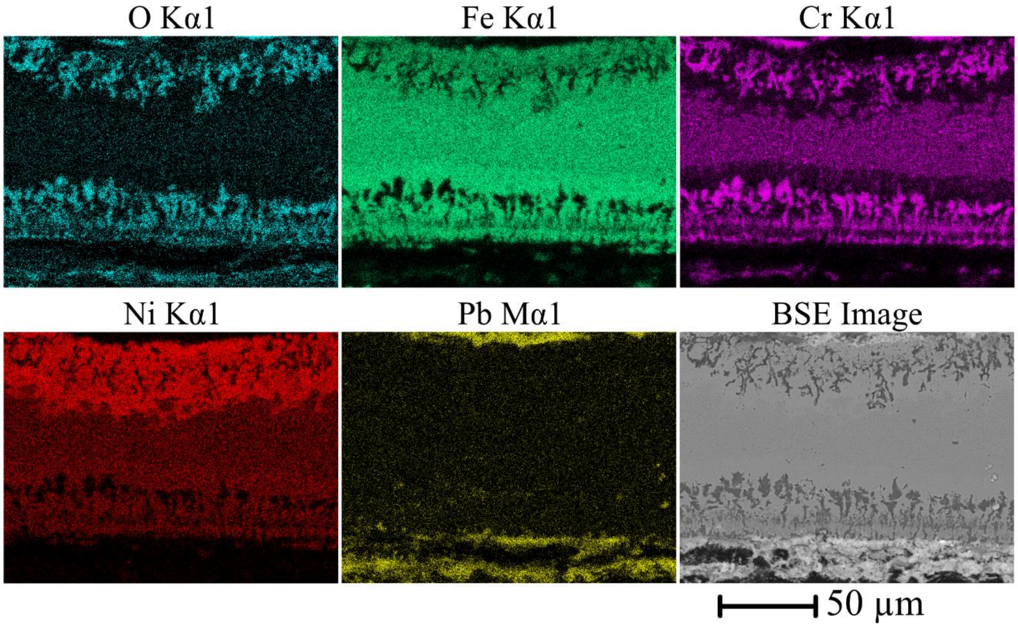

Figure 30: EDX maps from the center of the drilled site, exposure at 800 °C - 168h, taken with JEOL at 25 kV.

5.3.3.2. Delamination on Pb Side

The BSE images in Figure 28 features the severe delamination of oxide scales on the drilled areas, where multiple repeating oxide and Pb layers can be seen. The sensitivity of the BSE detector to the mean atomic number, and thereby electron rich elements of the phases has helped to differentiate between Pb-rich phases, the alloy, and corrosion products. Figure 31-a shows a clear distinction between Pb, alloy, corrosion products; and the molten Pb penetration routes, similar to the initiation of the delamination on 600 °C (Figure 19). A larger gap between the oxide layers and the cladding tube can be seen in Figure 31-b, where the contrast is darkest, comparable to some parts of the inner side of the cladding tube. These darker spots are epoxy that was filled during cross-section preparation (after exposure). Here the molten Pb has significantly impacted the adherence between the oxide layers and metal, which resulted in detached scales during cooling after exposure. The size of the gap and the fact that the gap is not filled with Pb suggests that this gap formed mostly during cooling and preparation.

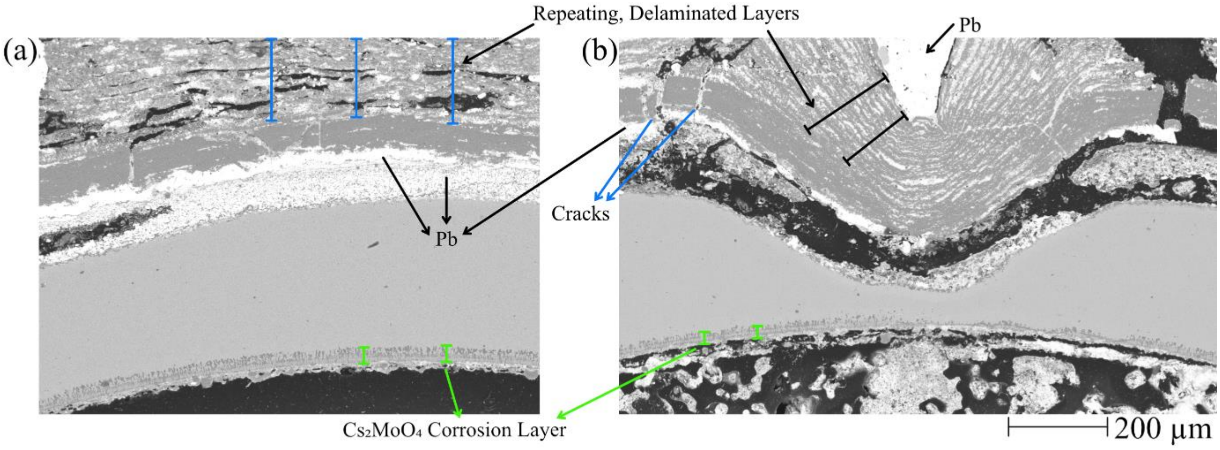

Figure 31: BSE images (same scale) for exposure at 800 °C - 168 h exposure, (a) free surface, (b) drilled area.

EDX mapping and several EDX point analysis were used on a part of Figure 31-a. The maps of Pb, Fe and O (in Figure 32) confirm that the "Repeating, Delaminated Layers" are a mixture of molten Pb and Fe-oxide layers. Underneath these layers, a Fe and O rich layer was seen, with a thickness between 53 to 73 µm. This layer was cracked and then wetted by molten Pb. The layer's composition was as follows; 49-54 at.% O, 41-42 at.% Fe, 3-8 at.% Cr. Beneath this FeO layer are darker spots mixed with solidified Pb. The composition of the darker spots is 52-62 at.% O, 7-9 at.% Fe, 24-32 at.% Cr, 2-3 at.% Pb, and ~3 at.% Mn. The analysis of these spots indicates a possible mixed spinel phase. Further EDX point analysis were used on brighter spots to confirm the existence of Pb, which showed 4.5 at.% Cs, likely due to Cs species smearing during cross-section preparation. No breach was observed at this temperature; which eliminates the possibility of Cs transport across a crack from Cs_2MoO_4-side during exposure. A chemical diffusion path through the compact alloy is not viable. However, due to the softness of Pb and Cs species, smearing residues are more likely to be found on Pb surfaces.

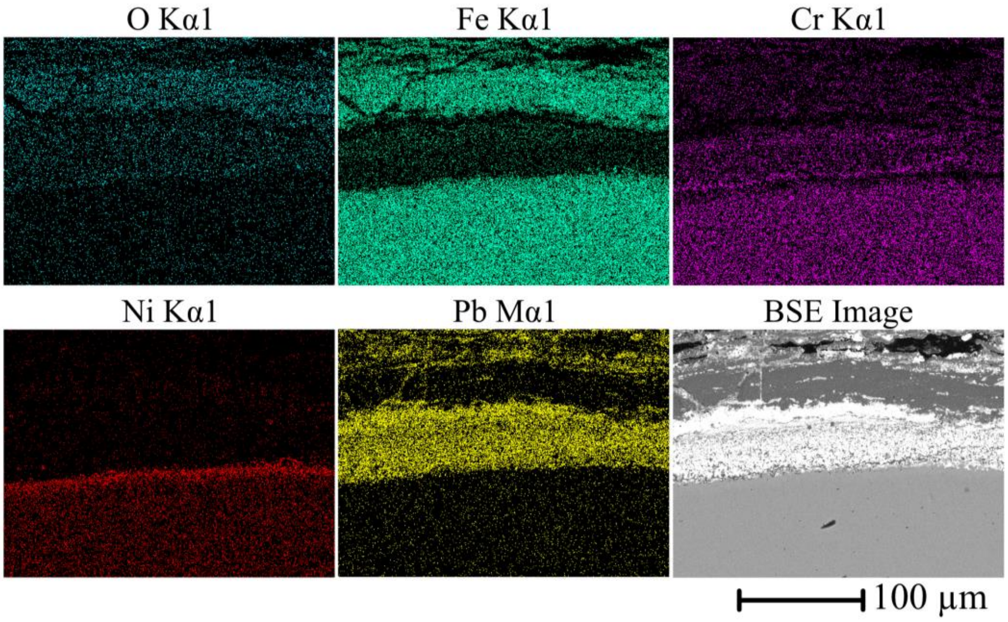

Figure 32: EDX maps from free surface, from Pb-side, exposure at 800 °C - 168 h, taken with JEOL at 25 kV.

At drilled areas and free surfaces, similar delamination and corrosion layers were observed. Further attention was given to the interface between alloy and the delaminated layers in this area on Figure 33, where the delaminated layers have managed to adhere to the alloy during cooling, allowing a rare opportunity for an investigation. Even though the exact structural information cannot be obtained, elemental composition revealed a Fe- and O-based phase with 1-2 at.% Mn, and varying amounts of Cr. The atomic percentage of Cr was ~19% in the Fe-oxide layer closest to the internal oxidation; even though it was separated (5-10 µm) from the alloy by Pb. However, ~25 µm away from the alloy, this percentage dropped to almost half.

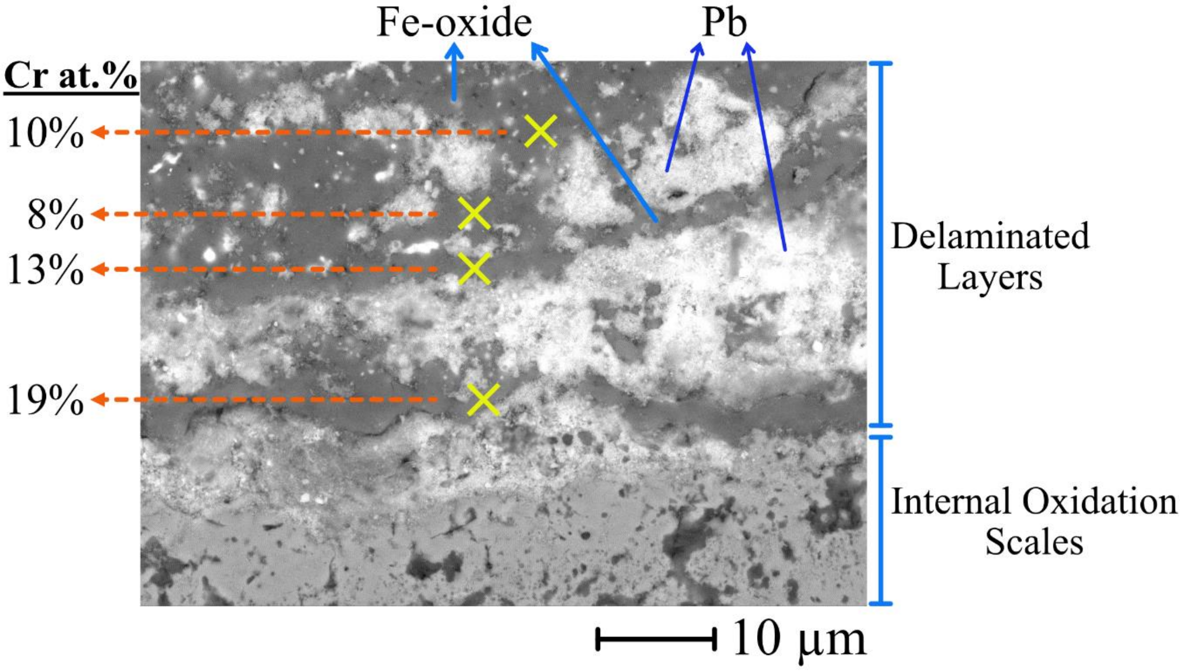

Figure 33: BSE image and EDX point analysis of 800 °C - 168 h exposure, from center of a drilled area. Point analysis focused on Cr content of oxide layer component of delamination layers.

5.3.3.3. Internal Oxidation by Molten Pb

A free surface (min 600 µm away from the drilled areas) can be seen in Figure 34. On Figure 34-a, the previously discussed delaminated layers are observed again. The morphology is comparable to Figure 28 and Figure 31; 5-10 µm thick layers of stacked Fe-oxide and Pb, with a lower layer of thicker Fe-oxide that is more intact compared its upper counterparts. The delaminated layers have detached during cooling, leaving a 130-145 µm gap, which was later filled by embedding material (“Epoxy Filling”, Figure 34-a). The horizontal long white streak between the alloy and the delaminated layers is due to the charging effect on large epoxy surface; which was a phenomenon seen on similar areas across all the samples. Right below the “Epoxy Filling” are the internal oxidation branches growing into the alloy, with a penetration depth of 22 to 32 µm, as seen in Figure 34-b & -c. The major growth of the branch-like internal oxidation happens perpendicular to the circumference of the cladding cross-section, while the parts of the branches that are furthest from the molten Pb are thicker, akin to 600 °C and 700 °C. There are remnants of solidified Pb on the molten Pb/alloy interface (blue arrows on Figure 34-c) but the penetration of Pb into the alloy has been limited, suggested by the lack of brighter spots and lack of EDX signals. The oxygen percentage of the oxidation branches varied from 46 to 54 at.%, while Fe (6-15 at.%), Ni (4-11 at.%) and Cr (22-29 at.%) were identified as main components of internal oxidation; which is most likely a mixed spinel. The remaining metallic grains between the branches were found to be a Fe-Ni solid solution that contained 40-48 at.% Fe and 40-54 at.% Ni (2.5-8 at.% Cr and 0.7-1.4 at.% Mo, as minor components). This is consistent with the results of the EDX map in Figure 30, where a Ni-enrichment was seen on the Pb-side. The Fe-Ni solid solution signifies that the internal oxidation is not a continuous scale, but instead branches are the main path of the oxygen ingress into the alloy.

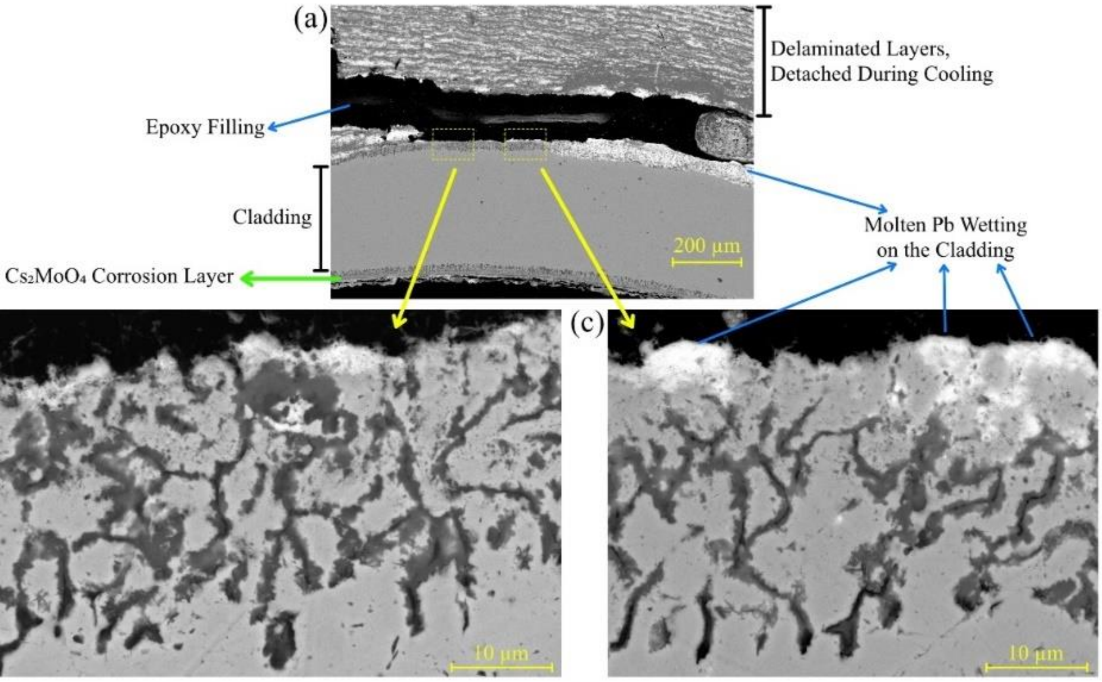

Figure 34: BSE image for exposure at 800 °C - 168 h exposure, from the Pb-side on a free surface.

Another set of analysis was conducted on one of the drilled areas (Figure 30), with the aim of defining similarities and differences to free surfaces. The results indicate that the effect of drilling on branch depth and chemical composition is negligible. The comparable morphology of the internal oxidation branches can be seen on Figure 35 (drilled area), and Figure 34 (free surface). Internal oxidation ingress has high O percentages, with varying amounts of Fe, Ni and Cr as main components. Unfortunately, the central regions of the branches (with a darker contrast) could not be investigated due to EDX limitations on spatial resolution (4.7); instead, the branches were investigated as a whole. A mixed spinel scale can be identified with the following main components: (in at.%) 45-64% O, 9-12% Fe, 15-28% Cr, 5-13% Ni, 0.5-3% Mn. Pb has not managed to ingress into the alloy. These suggest that branches are the main ingress route for O diffusion. Fe-Ni (respectively in at.%; 49-57% and 39-42%) solid solution can be observed between the branches, with varying (3-9 at.%) amounts of Cr [82], agreeing with Ni enrichment on Figure 30.

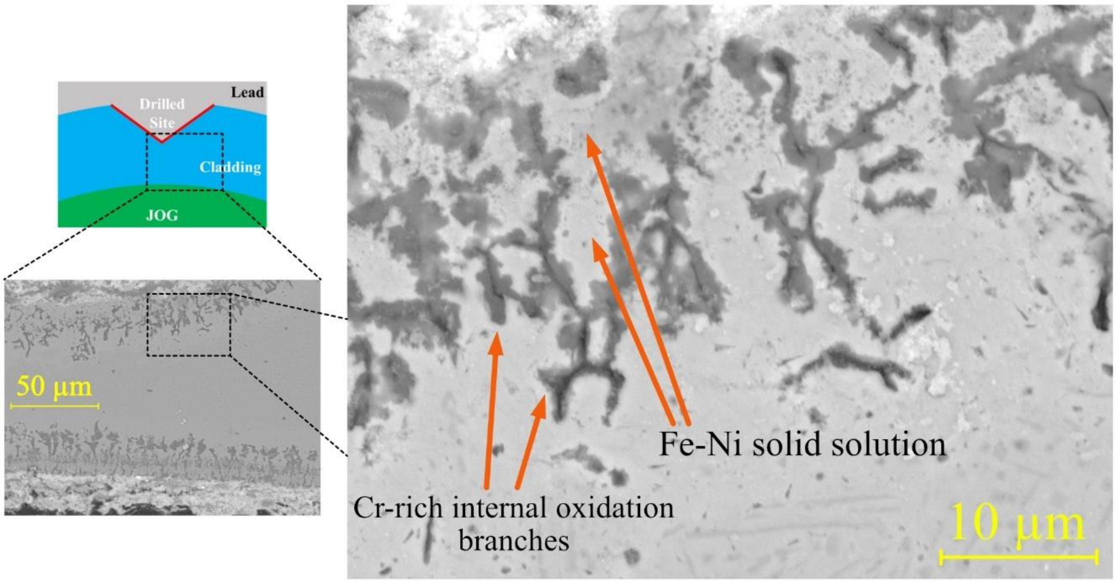

Figure 35: EDX point analysis (at.%), focusing on Pb-side near the center of the drilled area, exposure at 800 °C - 168h, taken with JEOL at 25 kV.

5.3.3.4. Corrosion on Cs_2MoO_4 Side

The JOG-side of this exposure was not influenced by molten Pb or the mechanical alterations, allowing for an independent investigation. A high-magnification image of internal oxidation by Cs_2MoO_4 is on Figure 36, where two different oxidation products are marked. $(Cr, M)_2O_3$ internal oxides were observed with varying amounts of M being Fe (4-9 at.%), Mn (2-5 at.%), and Ni (0.6-2 at.%). In addition, an Fe-rich (43-48 at.% O, 30-32 at.% Fe, 12-14 at.% Cr, 7 at.% Ni, <1 at.% Mo) spinel was observed; even though the grain morphology, contrast and depth are similar. This spinel phase was detected also on the immediate interface of the alloy and Cs_2MoO_4, but the EDX spectra was affected by the Cs and Mo signals, and the quantification was not considered. However, the qualification was pointing towards a similar spinel phase with higher Cr content.

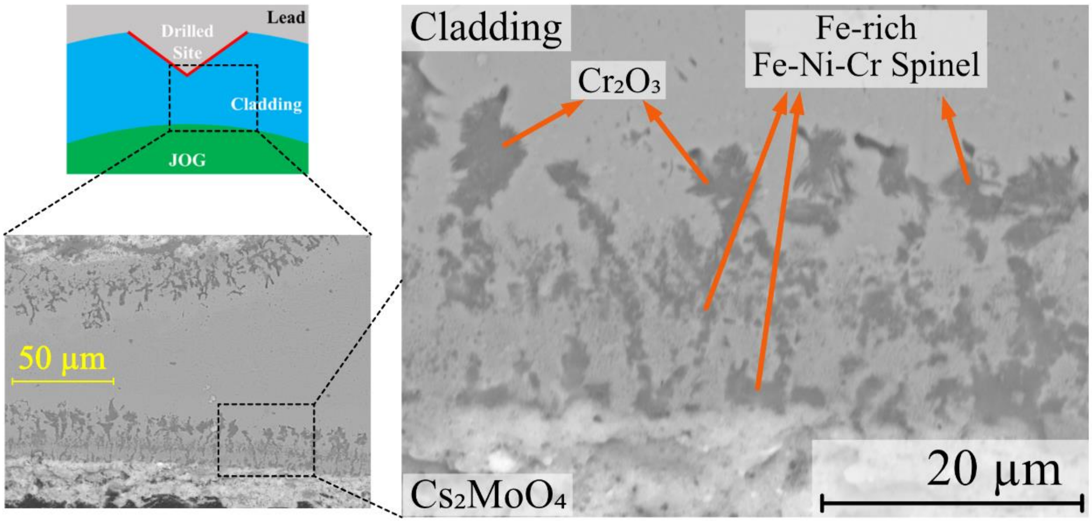

Figure 36: BSE images of the JOG-side of exposure at 800 °C - 168h, taken with JEOL at 25 kV.

5.3.4. 900 °C, 168 Hour Exposure

5.3.4.1. Overview of the Drilled Areas

Both environments' contributions to scale growth and alloy dissolution changes when exposure temperature approaches to the melting temperature of Cs_2MoO_4 at ≈950 °C [83]. The cladding tube exposed to 900 °C suffered multiple cladding breaches at the pre-thinned drilled areas. The breaches were documented by optical microscopy and SEM imaging, which can be seen on Figure 37. While most breaches did not cause observable mass transport between molten Pb and Cs_2MoO_4, one breach (Figure 37-d) was more violent than the rest. The cross-sections do not allow for an exact interpretation of mass transport. However, the broken pieces of cladding at the center of the drilled areas have been pushed towards the JOG-side of the exposure, indicating a push from molten Pb to the inside of JOG housing.

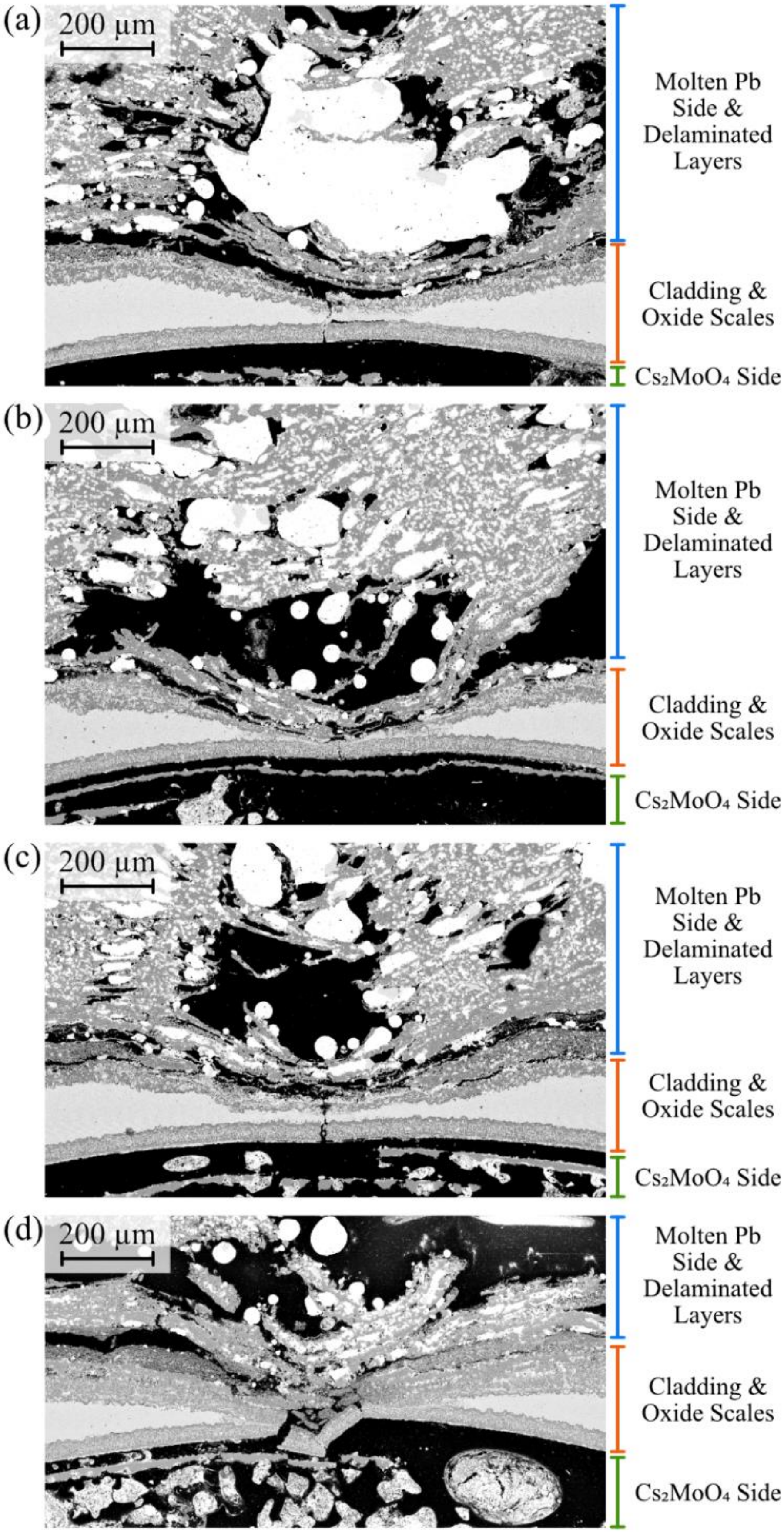

Figure 37: BSE images for drilled areas of 900 °C, 168 h exposure.

The delamination around drilled areas was too heterogeneous to recognize a repeating layer. The centers of these areas hosted big pools of molten Pb, which can be identified by the contrast difference between epoxy (darkest), oxide layers, alloy, and the Pb (as the brightest layer). The delaminated oxide layers were thinner closer to the alloy, in comparison to their counterparts further away from the alloy. The elemental composition of these delaminated layers closer to the center of drilled area and the Pb-pools in between them hold valuable information on the qualification of simulated fission product release.

The chemistry at the center of the drilled areas can provide information on the initialization of the breaches. Figure 37-a already showed that Pb side is more likely to be consumed before Cs_2MoO_4 side. On the other hand, the interaction of the internal oxidation scales by Pb and Cs_2MoO_4 is likely to be the initiation of the crack, as they would be the thinnest part and one of the most brittle parts of the cladding. Figure 38 shows the interaction of these internal oxidation scales. On the location marked blue in Figure 38-b, these internal oxides came in contact, as it can be observed by the darker-contrasted oxidation branches that are in direct contact with both sides.

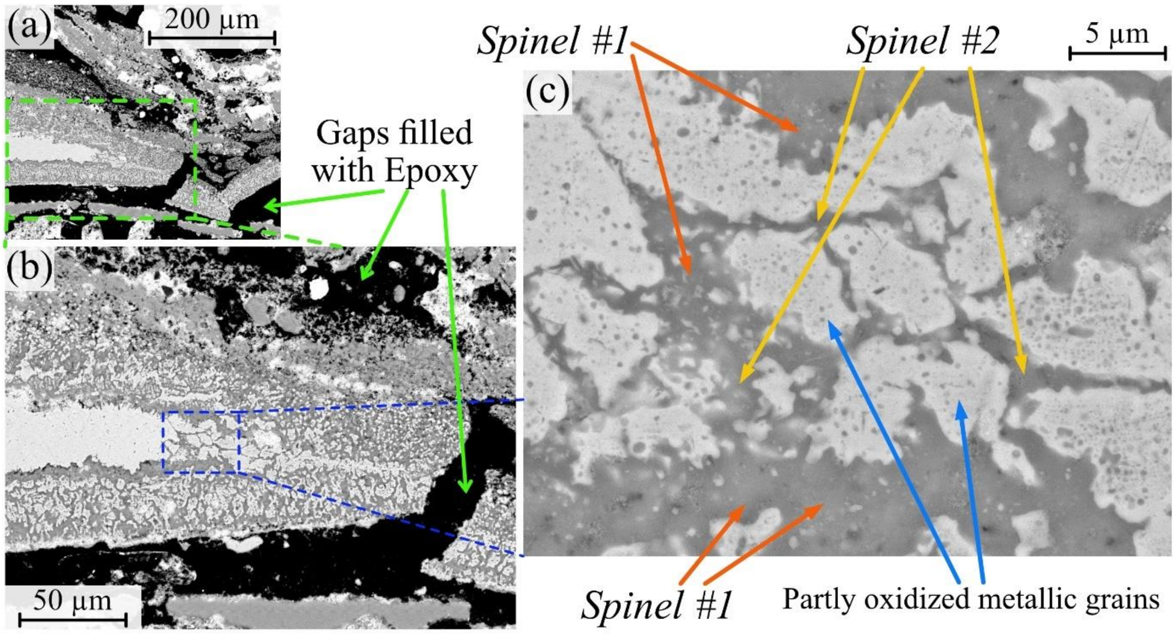

Figure 38: (a) Low magnification and (b) high magnification BSE image of violent breach that occurred on 900 °C, 168 h exposure. (c) Higher magnification image and the points of EDX analyses, detailed compositions on Table 6.

On the internal oxidation, two spinel phases with different compositions were detected. The comparison of their compositions can be seen in Table 6 as *Spinel #1* and *#2*. These spinel grains are differentiated by their Fe content, as big differences are seen; while Cr percentage is similar. Even though the analyses were done from different locations, no correlation between Fe/Cr ratio was detected. However, the Cr-rich spinel does not host Ni as the Ni percentage was mostly in impurity or background level. The same can be said about Cs, while Mo percentage is closer to the original alloy levels. On the other hand, Ni enriched metallic grains are seen here, just as they were in other exposures; showing similar Fe and Cr percentage as well.

Table 6: Elemental composition of breach tip (Figure 38-c) observed on 900 °C, 168 h exposure.

Grain Type	**Element in Atomic Percentage**								
	O	**Fe**	**Cr**	**Ni**	**Ti**	**Mo**	**Cs**	**Si**	**Mn**
Spinel #1	57.7	11.8	25.9	0.3	0.1	0.8	0.4	1.3	1.6
	55.6	14.3	25.5	2.8	0.2	0.4	0.1	0.3	0.9
	59.7	12.2	21.1	0.6	0.2	1.2	1.2	2.2	1.6
	57.2	13.2	21.4	0.5	0.4	0.7	1.3	3.9	1.4
Spinel #2	52.4	20.9	20.1	3.7	0.3	0.6	0.2	0.5	1.3
	53.7	23.5	14.5	5.9	0.4	0.6	0	0.3	1.1
	47.3	25.3	20.3	5.1	0.2	0.4	0.1	0.2	1.1
Metallic	-	67.1	4.6	26.4	0.3	1.5	-	0.0	0.1
	-	66.7	5.2	26.4	0	1.3	-	0.3	0.2
	-	66.5	4.4	27.2	0.3	0.8	-	0.4	0.3

5.3.4.2. Delamination on Pb Side

As in all conducted exposures, delamination is the major contributing factor to the cladding thickness loss. Similar to exposures of lower temperature (600 °C, 700 °C, 800 °C), repeating layers of molten Pb and oxide layers were observed around the cladding tube. Also similar to other exposures, the delamination investigation was conducted away from the drilled areas, as seen in Figure 39. The biggest difference was the irregularity of the repeating layers. This would be expected as the temperature increases. Even though layers of molten Pb could be seen less than 100 µm away from the cladding tube, the layers of oxide and Pb become much more mixed as the distance from the cladding increases. On Figure 39, the gaps filled with epoxy can be observed, confirming the inhomogeneity in the thermal shrinkage during cooling. The elemental compositions of the delaminated layers are in agreement with other exposures. These layers exhibit a Fe-oxide structure (main components; 53-62 at.% O, 29-41 at.% Fe, 2-10 at.% Cr). The compositions were confirmed with EDX point analysis taken from different layers. No correlation between the distance from the cladding tube and the elemental composition was seen.

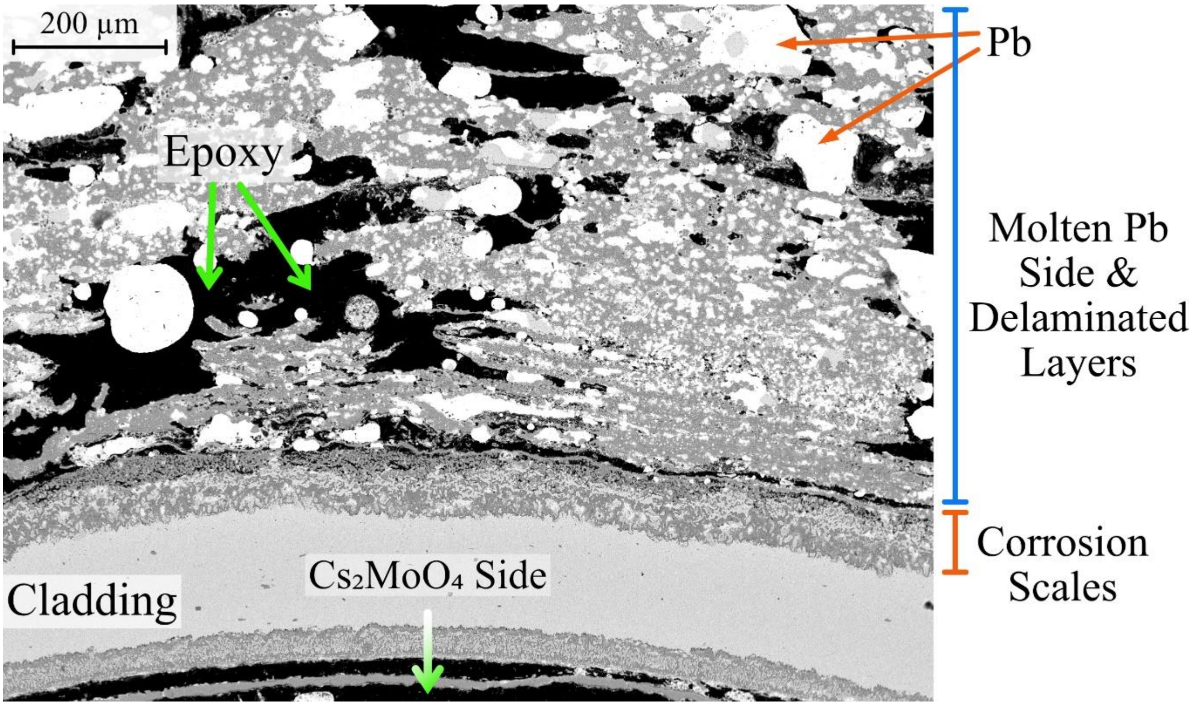

Figure 39: BSE image of a free surface of 900 °C, 168 h exposure; showing delaminated layers and corrosion caused by either environments (molten Pb or Cs_2MoO_4).

5.3.4.3. Internal Oxidation by Molten Pb

In order to understand the breaching characteristics more deeply, the contribution of molten Pb and Cs_2MoO_4 should be investigated separately. Due to the severe de-alloying (of either Fe, Cr or Ni) occurring around the drilled areas, some internal oxidation phases were not able to form. Instead, free surfaces were investigated to analyze the internal oxidation caused by the dissolved oxygen in molten Pb. An overview of the investigated location can be seen in Figure 40, which is from the same area as Figure 39. The outermost scale is growing on the cladding without significant detachment. However, the scale is detaching in itself. i.e., opening gaps. This scale was identified to be a Fe-Cr spinel scale (~60 at.% O, 15-20 at.% Fe, 15-20 at.% Cr), which is similar in composition to the spinel in the inner scale (55-60 at.% O, 17 at.% Fe, 17-22 at.% Cr). The outer and inner spinel here are close in Fe/Cr/O ratios, but the difference is the morphology. The inner spinel is comparable to other exposures, both with the branch-like morphology and the Ni enriched metallic inclusions between the branches. Although, the Ni percentage was slightly lower (~65 at.% Fe, ~30 at.% Ni, ~5 at.% Cr). The metallic inclusions are partly oxidized by spots that are smaller than 1 µm in size, making the spots' analysis impossible with these characterization parameters. Furthermore, the oxygen peaks were not clear in the EDX spectrums and were omitted from the quantification as a result. These small spots of oxidation were not seen on lower temperature exposures, but they are a feature of both the 900 °C (168 h) and 1000 °C (52 h, to be presented later) capsule exposures. Another metallic scale, which is more continuous, was located between the outer and inner spinel scales. The composition of this scale was close to the metallic inclusions.

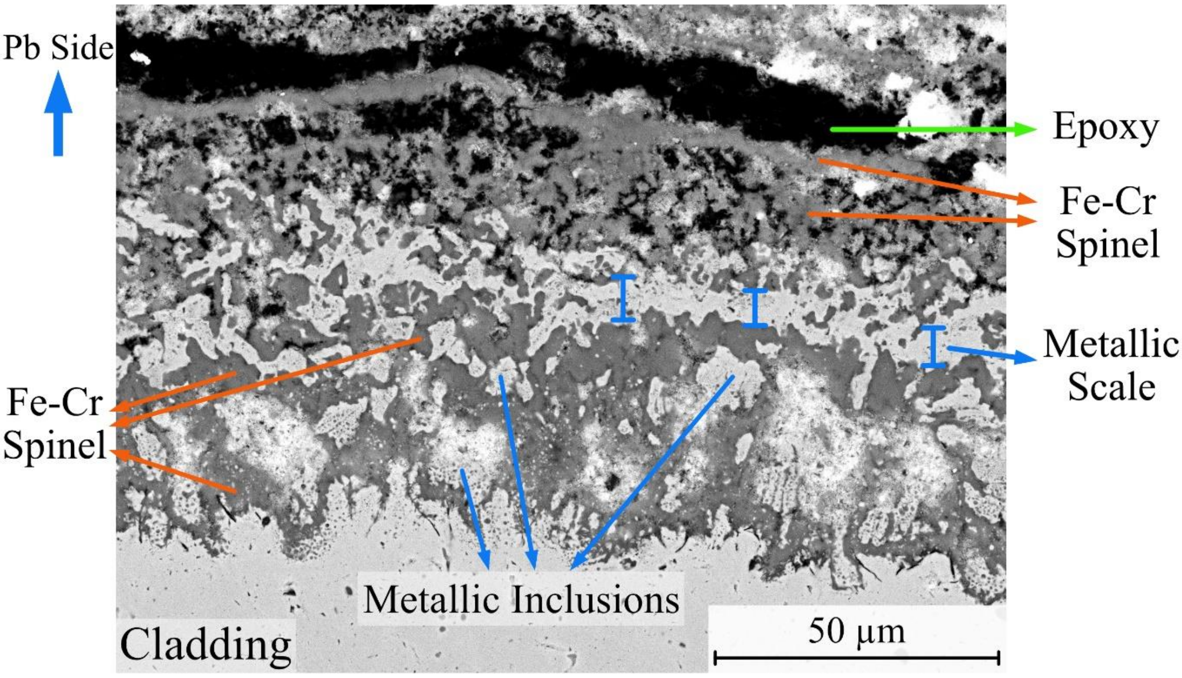

Figure 40: BSE image of the internal oxidation caused by molten Pb, taken from a free surface, exposure at 900 °C, 168 h.

5.3.4.4. Delamination on JOG Side

The exposure at this temperature shows the first instances of delamination caused by Cs_2MoO_4. The lower section of Figure 41 shows the delamination caused by Cs_2MoO_4. Delamination by molten Pb was seen and reported many times on other temperature levels, including 900 °C. Compared to molten Pb, this delamination did not have multiple repeating layers, but instead only 2 layers; locally even only single layers were seen around the cladding cross-section. This suggests a different and less violent mechanism of delamination than in comparison to molten Pb; while making it difficult to pinpoint the said mechanism. These two layers were measured to have a wide range of thickness, with inner and outer layer being 6.8 to 17.7 µm and 2.9 to 9.4 µm, respectively.

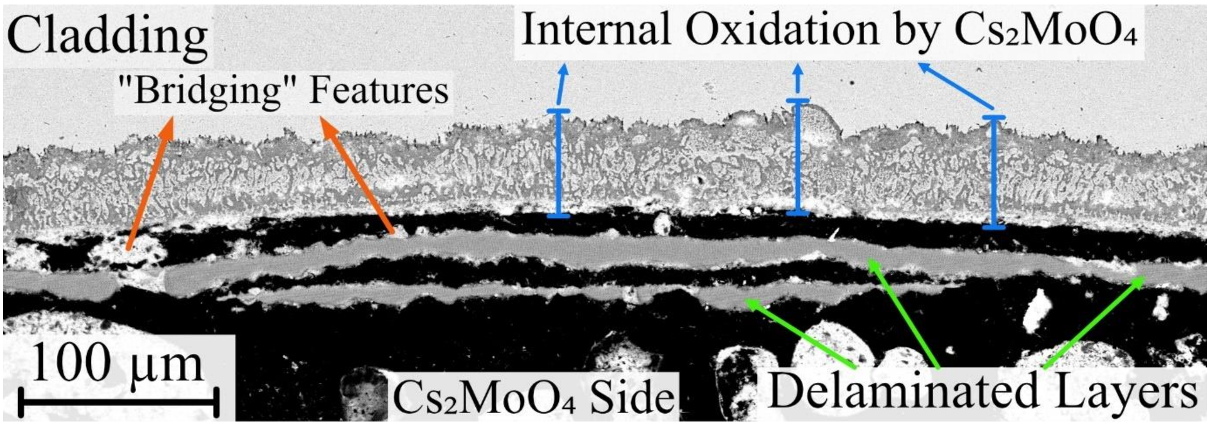

Figure 41: BSE image of internal oxidation and delamination caused by Cs_2MoO_4, exposure at 900 °C, 168 h.

Between the delaminated layers and the internal oxidation scales, brighter and round shaped features were observed. On this regard, the delamination process shares a similarity to the molten Pb. However, these features were localized and were not observed to be continuous. Upon closer inspection, these features were found to have many darker spots scattered on them. These small spots were smaller than 1 µm in size, making their individual investigation not possible with these analysis settings. Regardless, two different EDX analysis from one of these round features yielded the composition seen in Table 7. The high oxygen content of the EDX point analyses correlates with the contrast in BSE image. Furthermore, the Pb ingress into the cladding assembly is also confirmed as Pb signals were clear and present.

Table 7: Elemental composition of bright “bridging” features next to delamination layers, taken from two different location at 25 kV, with JEOL.

at.%	O	Fe	Cr	Ni	Pb	Mo	Cs	Si	Mn
Point 1	68	7	1.8	1	6	8	2	6	0.2
Point 2	59	9	2	1	7	10	4	8	0.3

The delaminated layers were investigated with EDX point analyses too, taking measurements from 9 different points on different layers. As seen in Table 8, the layers were Fe-oxide phases with low amounts of Cr and Mn in them. During the EDX measurement, Si peaks corresponding to ~0.3 at.% were found, but later omitted; as the quantifiable peaks were not consistent.

Table 8: Elemental composition of delaminated layers caused by Cs_2MoO_4, taken from 9 different points and averaged, EDX taken at 25 kV, with JEOL.

Elemental Composition in Atomic %			
O	**Fe**	**Cr**	**Mn**
50.9	45.2	0.7	3.3

5.3.4.5. Corrosion by Cs_2MoO_4

The internal corrosion by Cs_2MoO_4 was investigated at a free surface, far from the drilled areas, as seen in Figure 42. No outer scale was observed, but an internal oxidation scale with different components can be seen. Between the epoxy and the internal oxidation scale, there is a heterogeneous scale which is slightly brighter colored compared to alloy. This scale was the leftover Cs_2MoO_4 powder mixed with the internal oxidation scale, as identified (by EDX) with Fe, Cr, Ni, Si peaks accompanying Cs and Mo peaks. Pb peaks were also seen, suggesting either Pb smearing during cross-section preparation or Pb ingress into the JOG housing. This heterogeneous scale was not involved either in the investigation or the following discussions as it was determined as a preparation artifact; a consequence of no use of additional cleaning of JOG housing. The other components of the corrosion scale can be separated into 3; intergranular oxidation, the metallic inclusions with intragranular oxidation spots and the continuous oxidized scale adjacent to the alloy.

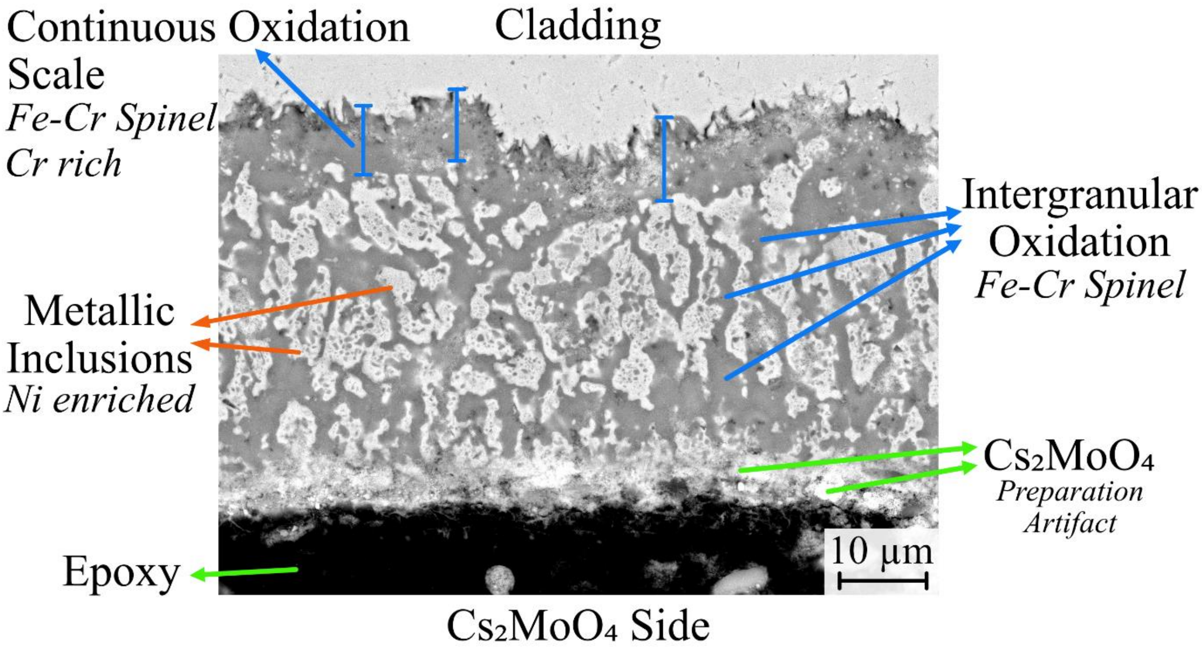

Figure 42: BSE image for exposure at 900 °C - 168 h exposure, from the Cs_2MoO_4 on a free surface.

The morphology of the intergranular oxidation is akin to other exposures, while the oxides themselves are thicker. In these grain boundaries , a spinel phase is observed where Fe and Cr amounts (50-56 at.% O, 20-21 at.% Fe, 16-20 at.% Cr) are similar, alongside ~2 at.% Ni and ~0.5 at.% Cs. The composition of spinel changes when investigating the continuous oxidation scale adjacent to the alloy. Here, a spinel scale is observed again, where the Cr is almost twice as Fe (58-61 at.% O, 11-12 at.% Fe, 20-24 at.% Cr) with higher Cs (0.3-0.9 at.%) and impurity level Ni (0.5 at.%). This would be the expected outcome as Cr supply would be plentiful adjacent to the alloy.

The metallic inclusions between the branches have been mostly oxidized by smaller spots of <1 µm in size, this was also reported earlier on the Pb-side corrosion fronts. The metallic inclusions were investigated by omitting the oxygen peaks from quantification. Two grains were analyzed to reveal the following composition; 63-65 at.% Fe, 8-10 at.% Cr, 23 at.% Ni. The similarities to the internal oxidation by molten Pb are seen again, with a Ni enriched metallic scale remaining between oxidation branches.

5.3.5. 1000 °C, 52 Hour Exposure

5.3.5.1. Overview of the Drilled Areas

The 52 h exposure at 1000 °C suffered from comparatively broad cladding breaches, and even complete loss of drilled area centers. Optical microscopy has been sufficient to confirm the cladding failure of at least three drilled areas. In Figure 43, the breakthroughs at the drilled areas are shown, and show clearly that molten Pb has pressed inwards; although, more severely than after the longer 900 °C exposure.

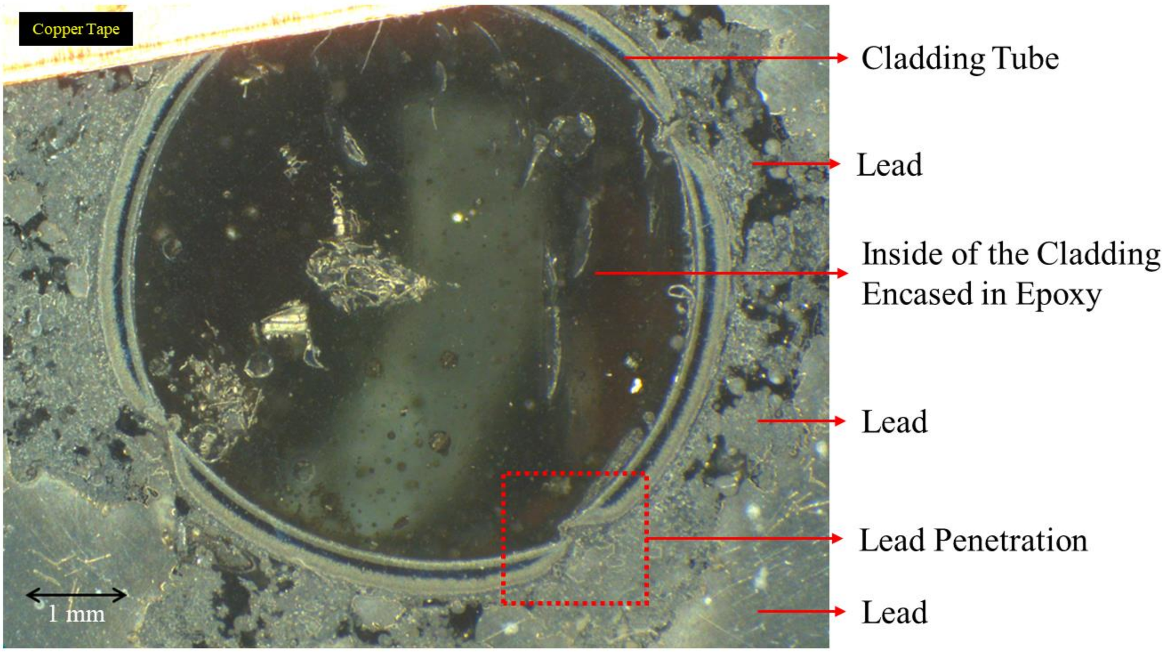

Figure 43: Optical microscopy image of a cross-section of the cladding tube after 52 h exposure at 1000 °C.

Figure 44 confirms what is seen on the optical microscopy image (Figure 43); a complete breach of the drilled area, total consumption of the center, and thinned cladding tips extruded inwards. The stress from the molten Pb side was enough to push the thin cladding tips inwards to the JOG housing side.

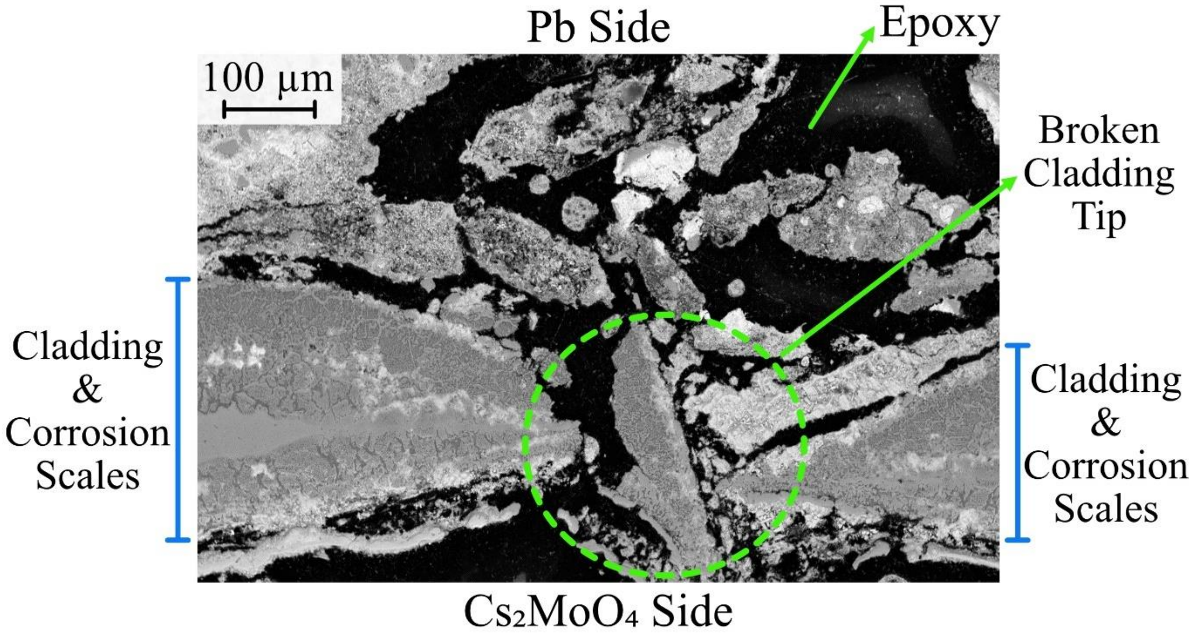

Figure 44: BSE image of one of the cladding breaches observed at drilled areas, for the exposure at 1000 °C, 52 h.

5.3.5.2. Delamination on Pb Side

The delamination on Pb side was severe enough to cause a thickness loss of ~40%, and enough to cause significant breaches at drilled sites. Oxide scale delamination observed after exposure at 1000 °C for 52 h is akin to 900 °C as (unlike to lower temperature exposures) it is heterogeneous and lacks orderly repeating layers of Fe oxide and Pb, which appears rather chaotic here. This is an expected outcome due to the temperature of this exposure, even though the duration is only 52 h. Figure 45 shows a five-image compilation to reflect on the severity of the delamination at this temperature. The stacked image ranges 1842±5 μm vertically. It starts from the internal oxidation scale at the bottom, and the top image ends with the molten Pb pool. The Fe-oxide based delaminated layers can be seen again, fragmented, with small amounts of Cr dissolved inside.

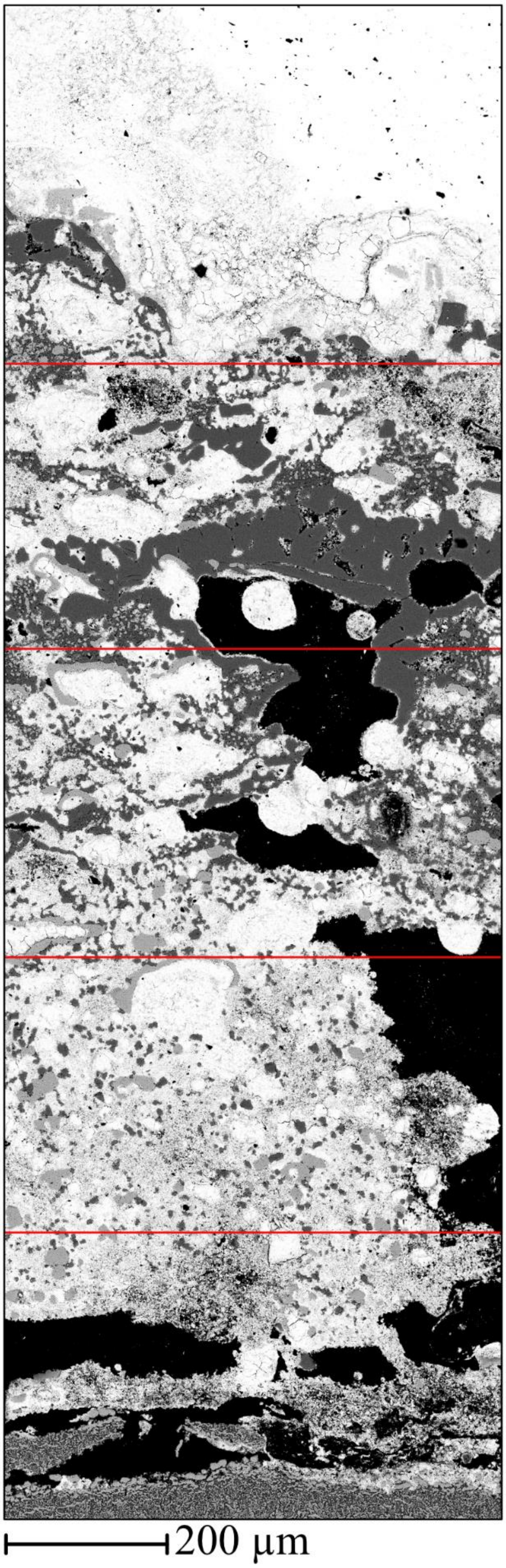

Figure 45: The five compiled images show the delamination on Pb side, exposure at 1000 °C and 52 h. The red lines represent transition to a new image.

A piece of the internal oxidation scale was broken off by the molten Pb and was investigated to better understand the initial stages of the delamination. The low and high magnification images can be seen in Figure 46. The broken piece had the same grains as the internal oxidation scale. Also, the broken piece and the oxidation scale had a brighter contrasted phase between them, which was confirmed to be Pb by EDX. The broken piece was a mixture of thin metallic-remaining grains and a Fe-rich spinel (54 at.% O, 26 at.% Fe, 15 at.% Cr, 3 at.% Ni). Metallic grains were Ni enriched pieces (71 at.% Fe, 8 at.% Cr, 20 at.% Ni) of the alloy, akin to other exposures. The detached metallic pieces just above the internal oxidation scale were also quantified and revealed a similar composition; (76 at.% Fe, 1 at.% Cr, 22 at.% Ni).

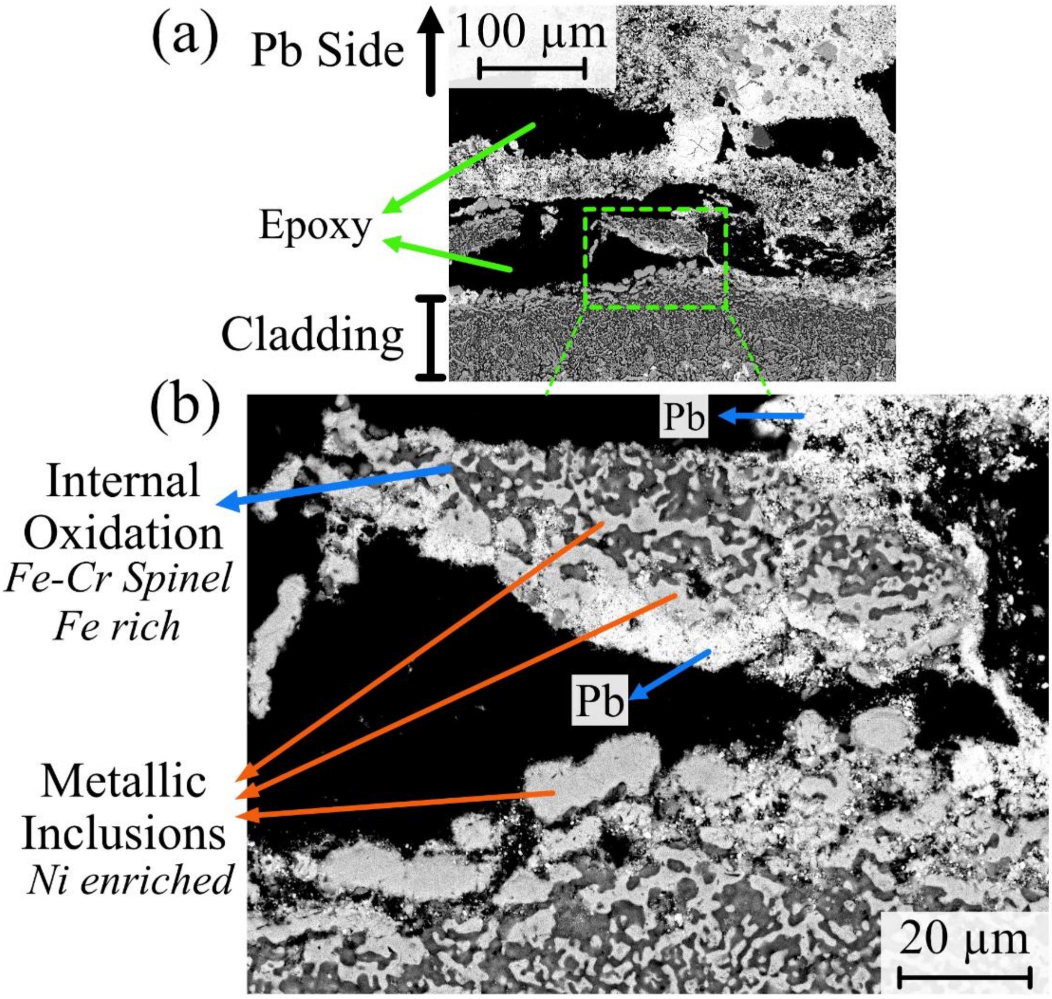

Figure 46: BSE image of delaminated and broken of piece from Pb side of the exposure at 1000 °C, 168 h.

5.3.5.3. Internal Oxidation by Molten Pb

On this exposure, the internal oxidation scale was ~130 µm thick. The internal oxidation scale was split into two main components, the outer and the inner scales. The outer scale is a more homogeneous and more oxidized component, as can be seen in Figure 47. Even though there are metallic parts remaining, they are too small to be investigated with these analysis parameters. The grains of the outer scale are significantly smaller compared to the inner scale’s grains. On the interface of the inner and outer scale, molten Pb has penetrated into mainly the grain boundaries, as seen on Pb map of Figure 47. The penetration can also be seen as the brighter spots, thanks to the contrast difference generated by the BSE detector. If the duration of the exposure was longer, the molten Pb is likely to delaminate this layer, causing further thickness loss. The inner most oxide scale, closest to the metal-oxide interface, on the other hand, is thicker than the intergranular oxides above. Beneath that, chromium is significantly depleted. However, Pb has already reached locally underneath, indicating an upcoming faster corrosion progress, given more exposure time. All the grains are surrounded by 1-5 μm thick grain boundaries, which have not been observed on exposures with lower temperatures. The grains themselves are also filled with spots of oxidation, identified by their darker contrast.

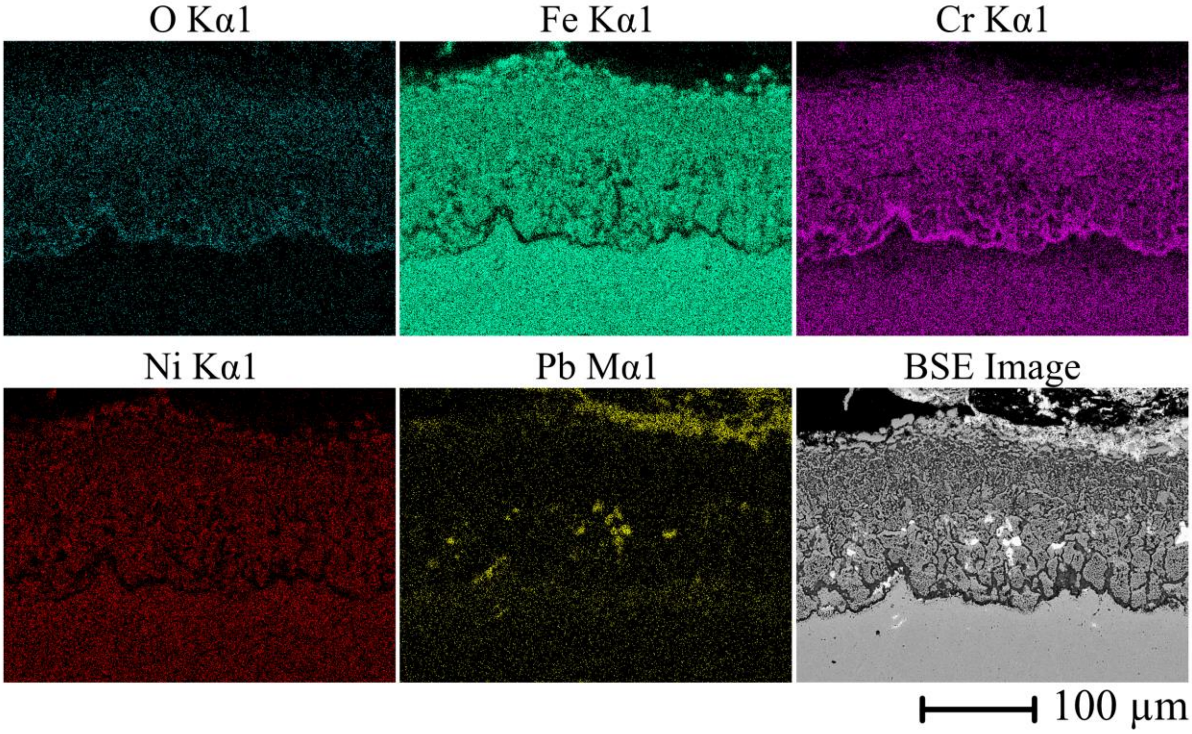

Figure 47: BSE image of Pb side internal oxidation on free surface, exposure at 1000 °C and 52 h.

The morphological differences of outer and inner scale were not reflected in the chemical composition. On these scales, 3 different features were examined in detail; oxide grains/boundaries, metallic remaining inclusions and the oxide layer right next to the alloy. A minimum of 3 points were selected and analyzed for all the features, and the averages of these compositions can be seen on Table 9. The oxide grains/boundaries are Fe-Cr spinel with low amounts of Ni. However, the oxide closest to the alloy is much richer in Cr, likely due to Cr supply from the alloy. The higher Cr content can also be confirmed from the Cr map of Figure 47. The metallic phases are in agreement with the other exposures and internal oxidation scales where Ni enrichment is seen.

Table 9: Elemental composition of Pb side internal oxidation scale components of exposure at 1000 °C, 52 h.

Grain Type	**Elements in Atomic Percentage**									
	O	**Fe**	**Cr**	**Ni**	**Pb**	**Ti**	**Mo**	**Cs**	**Si**	**Mn**
Oxides	55.6	19.6	17.2	1.7	0.1	0.3	0.6	1.1	2.7	1.3
Oxide by the Alloy	61.9	10.2	20.9	1.0	0.2	0.6	0.4	0.9	2.0	2.2
Metallic	-	71.1	4.8	22.4	-	0.2	1.1	0.3	0.8	0.4

5.3.5.4. Delamination on JOG Side

The delamination on the JOG side of the cladding tube was irregular as well (similar to 900 °C). While on some areas the layer was detached, it was still attached to the internal oxidation scale on other areas. The delaminated layer was found to be 4-8 µm in thickness, as seen in Figure 48. The layer is brighter in contrast compared to the alloy itself. This would indicate that the mean atomic number of the delaminated layer is actually higher than the alloy. The EDX measurement taken from various parts of this layer has confirmed this difference in contrast as following average (4 measurements) elemental composition was revealed; 21-33 at.% O, 27-32 at.% Fe, 4-5 at.% Ni, 36-42 at.% Mo. Peaks corresponding to less than 1 at% Si and Cs were omitted as the qualification of the peaks was not consistent on every analyses.

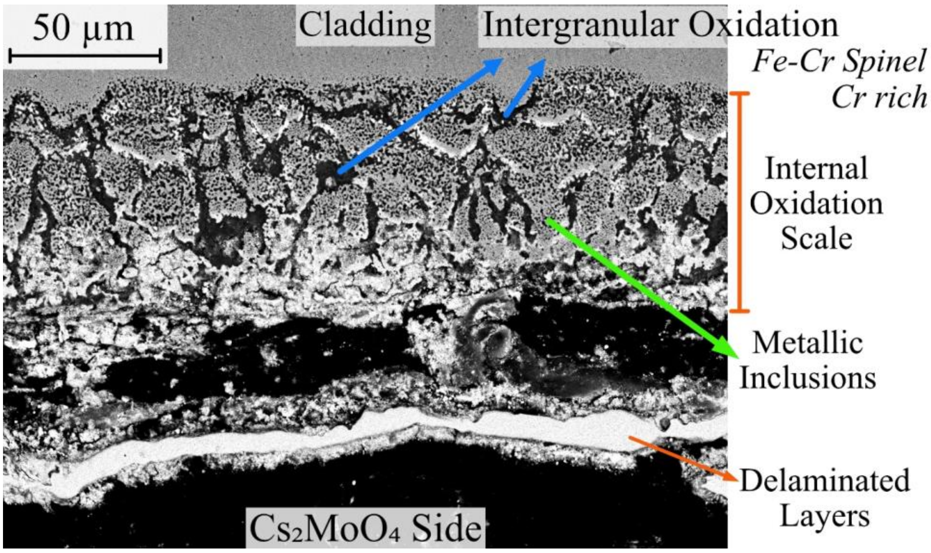

Figure 48: BSE image of JOG side internal oxidation and delamination on a free surface, exposure at 1000 °C and 52 h.

5.3.5.5. Corrosion by Cs_2MoO_4

Internal oxidation is the dominant mechanism of corrosion here. A single scale internal oxidation can be observed on Figure 48. The scale is made up of metallic grains that do not change shape or size as their distance increases from the Cs_2MoO_4 housing and are also filled with spots of oxidation. The spots are so prevalent that no completely metallic grain has remained in the whole scale. The metallic grains are surrounded by ~1 µm thick boundaries that mainly grow perpendicular to the cladding/Cs_2MoO_4 interface. These oxidized boundaries are the main oxides of the scale. The oxides do not change composition depending on the depth, and they are a Cr-rich spinel with the following elemental composition of the main components; 60 at.% O, 10 at.% Fe, 21 at.% Cr, 0.9 at.% Ni, 0.8 at.% Mo, 1.3 at.% Cs. While 3.5 at.% Si was detected, the standard deviation was too high, and Si was ruled out as a preparation artifact. In contact with the oxides and metallic grains, there are brighter colored lines, which are Mo and Pb that are diffusing into the alloy. Unfortunately, the quantification of these spots is not reliable with these analysis parameters. Although no Pb should be on this side of the cladding pre-exposure, this exposure suffered from comparatively broad cladding breach, which resulted in Pb ingress into the Cs_2MoO_4 housing.

The corrosion process changes behavior at the interface between alloy and corrosion scale. The grains did not have time to form, but instead the spots of oxidation are growing in a uniform thickness, in respect to the internal oxidation scale thickness. As the grain boundaries are not formed yet, it can be surmised that the spots are the main mechanism of internal oxidation growth, while the grain boundaries grow later as a result.

5.4. Confirmation Experiments

Confirmation experiments were conducted with a much simpler setup compared to capsule experiments to identify the JOG-cladding interaction exclusively. A flattened coupon of the same cladding tube was exposed to Cs_2MoO_4 on one side, under flowing Ar gas, for 168 h and the specified temperatures. This section will present the SEM, EDX and XRD results together. The results will be compared to the capsule exposure experiments in the Discussion section.

600 °C exposure showed localized single or double scale corrosion process. Figure 49 shows two different scales at further locations from each other. While Figure 49-a shows a more homogeneous scale with 0.7-2.4 µm thickness, Figure 49-b shows a heterogeneous scale with 2.6-8 µm thickness. The internal oxidation by Cs_2MoO_4 was a mixture of these scales, with different penetration depths, but similar compositions. 5 EDX point analyses was conducted on the internal oxidation layer on Figure 49-b resulting in the following average composition of main components; 67 at.% O, 20.5 at.% Fe, 4 at.% Cr, 4 at.% Ni. Additional point analyses in the internal oxidation scale (further from the alloy) showed lower Ni percentages. This effect was not observed consistently, and no further attention was given. However, additional analyses can be conducted in the future, in order to determine the oxidation kinetics of Cr and Ni, in regard to the scale thickness.

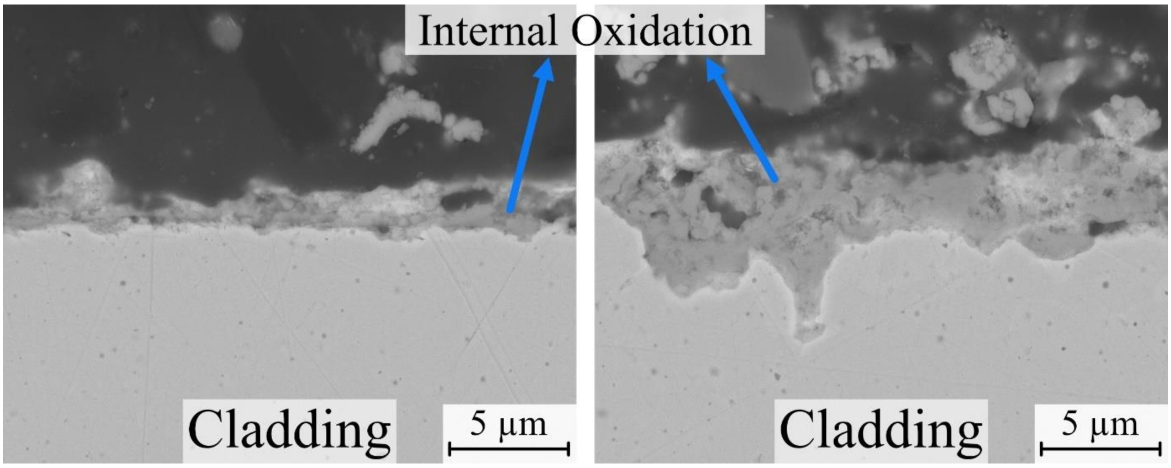

Figure 49: (a) and (b) BSE images of 600 °C (168 h) confirmation experiment's internal oxidation scales from two different locations.

In addition to the internal oxidation scale, an outward growing scale was also observed in Figure 50. This scale was not consistent throughout the surface and the layers were heterogeneous in regard to their morphology. The composition was found to be 68-74 at% O, 20-28 at.% Fe, 1.8-2.6 at.% Cr, 0.3-0.5 at.% Mn, with an inconsistent qualification of Ni.

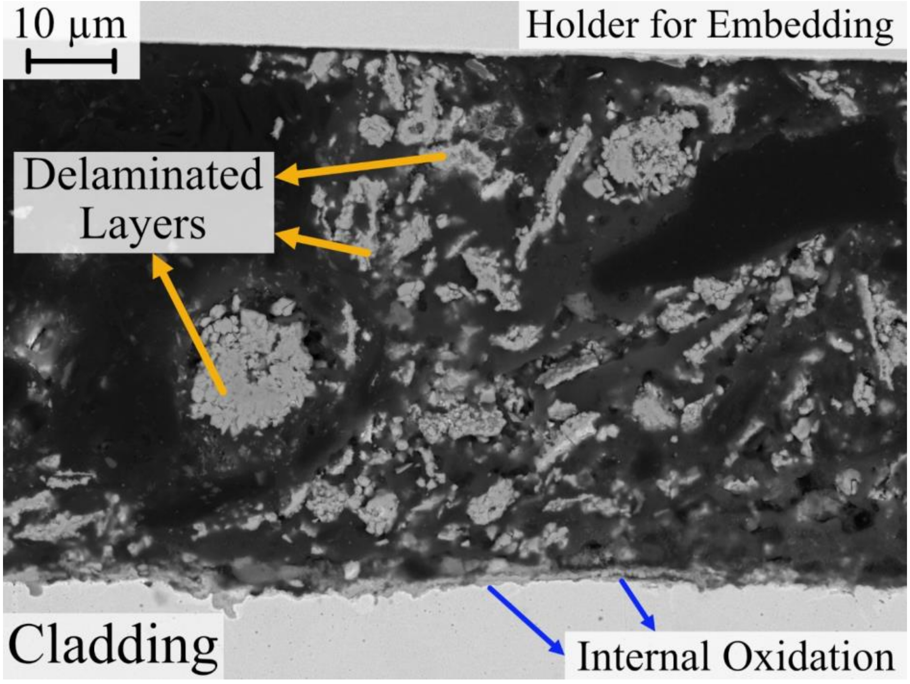

Figure 50: BSE image of 600 °C (168 h) confirmation experiment's delaminated layer, with the alloy in the bottom side and the perpendicular holder for embedding on the top side.

700 °C exposure showed an even more heterogeneous corrosion process compared to 600 °C. Internal oxidation was again the main process, but the scales were locally different, both in morphology and in thickness. Figure 51 shows 3 different locations that exhibit different scales. Here the thickness was 0.5-4.8 μm for (a), 0.3-1.3 μm for (b), 0.7-1.8 μm for (c). The composition of internal oxidation was similar throughout the coupon. On these scales, spinel structure with 60 at.% O, 10-15 at.% Fe, 10-20 at.% Cr and 2-10 at.% Mn was observed. The Cr and Mn ratios decreased for scales that were detached or further from alloy, while the Fe ratio was increased to ~25 at.% in the same areas, indicating a Fe-rich spinel was more

dominant of the outer scales. Closer and deeper into the alloy, the Mn ratio dropped to ~4-5 at.%, while Cr and Fe had closer ratios in the spinel; 15 at.% and 15-20 at.%, respectively.

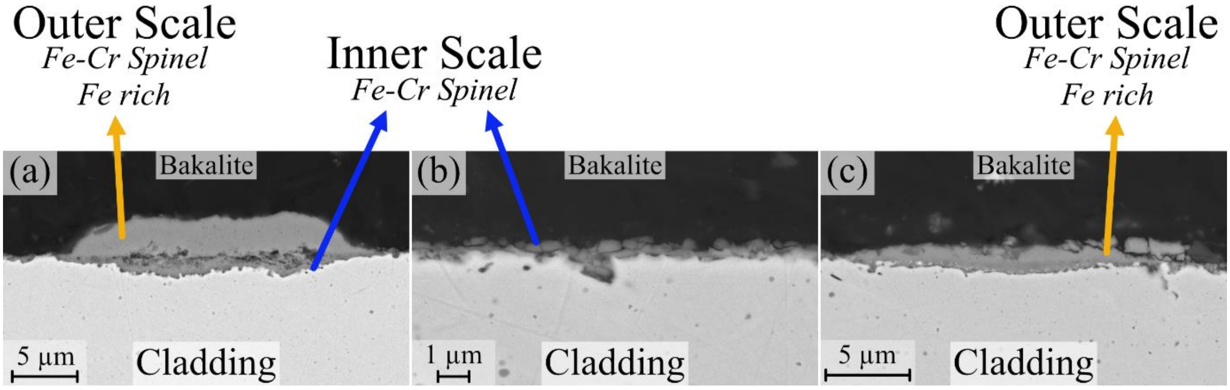

Figure 51: (a), (b), (c) BSE images of different internal oxidation scales observed on 700 °C (168 h) confirmation experiment.

800 °C exposure showed a two scale oxidation process, where an outer and inner scale with different compositions were observed. The inner scales' morphology was similar on different locations of the coupon surface, as seen in Figure 52. However, the outer scale was detached or adhered on different locations, similar to the localized corrosion processes observed on 600 °C and 700 °C. On adhered surfaces, it was difficult to differentiate inner and outer scales through the contrast difference, as the mean average atomic numbers are close, and further increase of the contrast decreased the overall image quality. Instead; considering the initial alloy as the so-called inner/outer interface, chemical analysis was used to discern the scales. The inner scale was a spinel scale with Cr-rich $M(II)M(III)_2O_4$ [M(III)=Fe, Cr; M(II)=Ni, Mn] composition (in at.%, Cr=15.4-25.1 and Fe=7.3-13). The Cr richness was also confirmed by Cr depleted alloy, adjacent to the inner scales. On the other hand, the outer scale was found to be a Fe-oxide scale with high Cr variation (1.8 to 8 at.%). The Fe (26.1-36.4 at.%) and O (58.5-64.2 at.%) percentages were more stable throughout the coupon surface. Apart from one exception, all the analysis showed less than 2 at.% Mn and Ni.

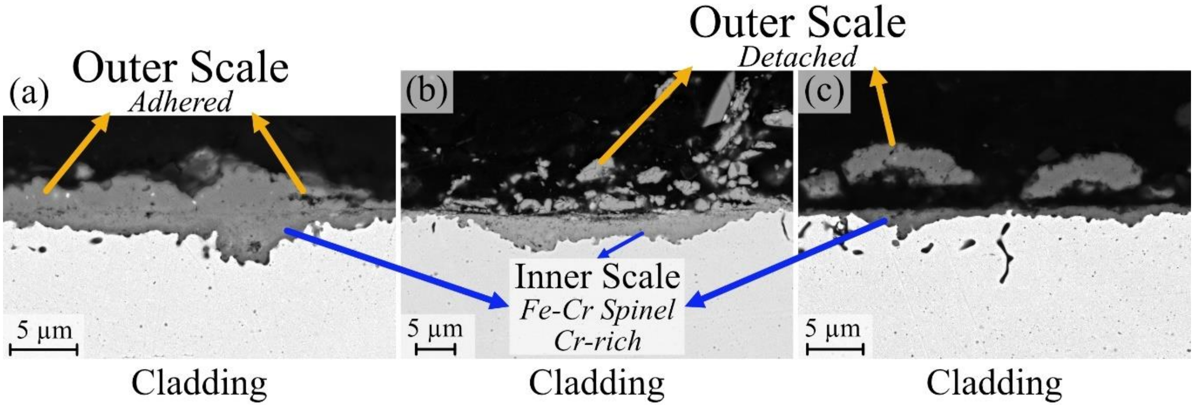

Figure 52: (a), (b), (c) BSE images of outer and inner scale on the coupon exposed to Cs_2MoO_4 at 800 °C for 168 h.

The two scale corrosion process was also seen on 900 °C exposure. Unfortunately, the Cs_2MoO_4 that remained on the exposure surface has caused problems during cross-section imaging, as seen in Figure 53. The inner scale was mostly unaffected; while on most of the cross-section, the outer scale was completely covered by Cs_2MoO_4. The white substance seen on Figure 53-a is a result of this; as well as the while streaks and pools, between the grey colored phases on Figure 53-b. Several steps of cleaning were employed; but eventually, these Cs_2MoO_4 that appeared were ruled as preparation artifacts, and separate images were taken for the morphological and elemental analysis of the outer scale.

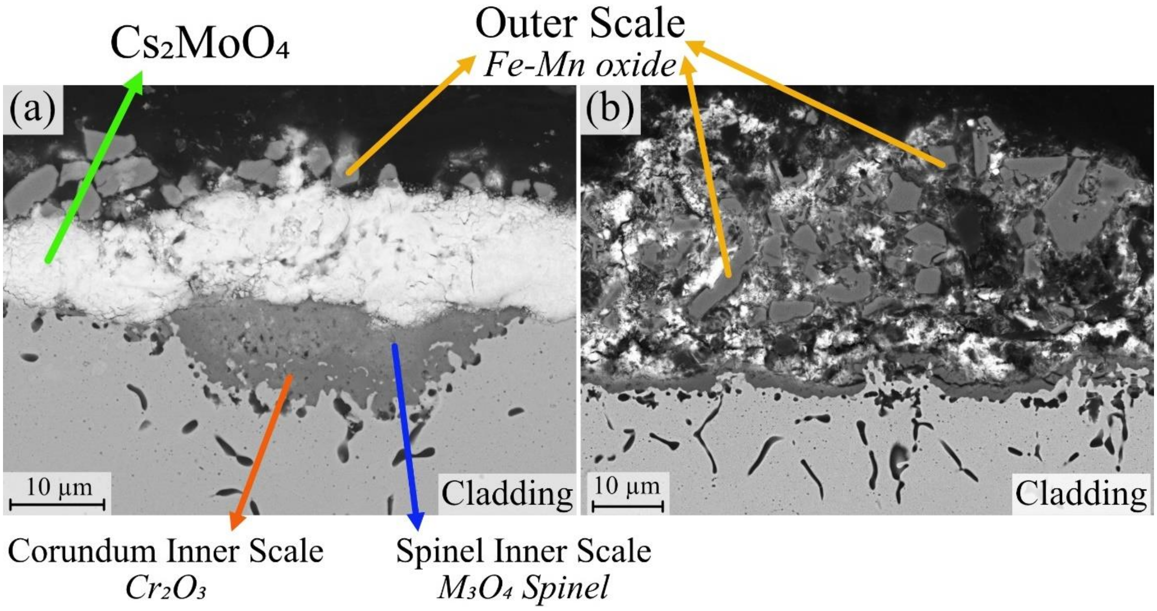

Figure 53: (a), (b) BSE image of outer and inner scale on the coupon exposed to Cs2MoO4 at 900 °C for 168 h.

The outer scale was a Fe-oxide scale that has grown heterogeneously and detached from the surface. The composition was similar to the outer scale of 600 °C confirmation experiment; 65 at.% O, 20 at.% Fe, 2 at.% Cr, 11 at.% Mn, 1 at.% Ni. This elemental composition suggests a mixed oxide of Fe and Mn. However, the elemental composition cannot give information about the oxidation state of Fe (II or III). The Cr and Ni percentages were not enough to effect the structure in a meaningful way.

The inner scale here was more complicated as 2 distinct phases were found on same inner scales. In order to eliminate an analysis error or contamination, this process was confirmed on multiple inner scales. A Cr_2O_3 (corundum) phase with 8-11 at.% Mn (62-66 at.% O, 21-24 at.% Cr, Fe & Ni <2 at.%) was detected, alongside a M_3O_4 spinel phase (O 60-63 at.%; M=Fe 5.9 at.%; Cr 15-17 at.%; Ni 7 at.%; Mn 5-7 at.%). The areas of these phases were also different but adjacent. On the well-like shape of the inner scale, the shallower center (in contact with the outer scale) was the spinel phase, while the outer sides of the "well" (deeper parts) was the corundum phase with Mn additions. Phase analysis will be used to confirm whether this corundum-like chemical composition was actually spinel or not. The internal attack of the alloy grain structure beneath the scales implies that all formed scales are nonprotective.

The edge of the coupon had a slightly different inner and outer scale formation. Due to the shape of the edge, oxidation mechanisms can be different than "flat" surfaces. Here this was seen majorly in outer scale as seen in the following elemental composition in atomic percentages; 65% O, 32% Fe, 1% Cr, 0.9% Ni, 1% Mn. In this outer scale, Mn is only present as an impurity element, suggesting a FeO scale. On the inner scale, a Fe-Cr spinel was observed with a slightly Cr-rich composition (12 at.% Fe, 17 at.% Cr, 3 at.% Ni), where Ni was not influencing the crystal structure, confirmed by XRD experiments.

All the coupons were analyzed by XRD analysis too. Figure 54 show the patterns with their respective peaks marked. The transition from Fe_2O_3 to spinel scales can be seen from 600 °C to 700 °C. The leftover Cs_2MoO_4 was present in all the spectra, while the structure turns into literature-reported β-Cs_2MoO_4 [62]. This transition is expected to happen below 600 °C but the peaks of β-Cs_2MoO_4 fit better for 800 °C and 900 °C.

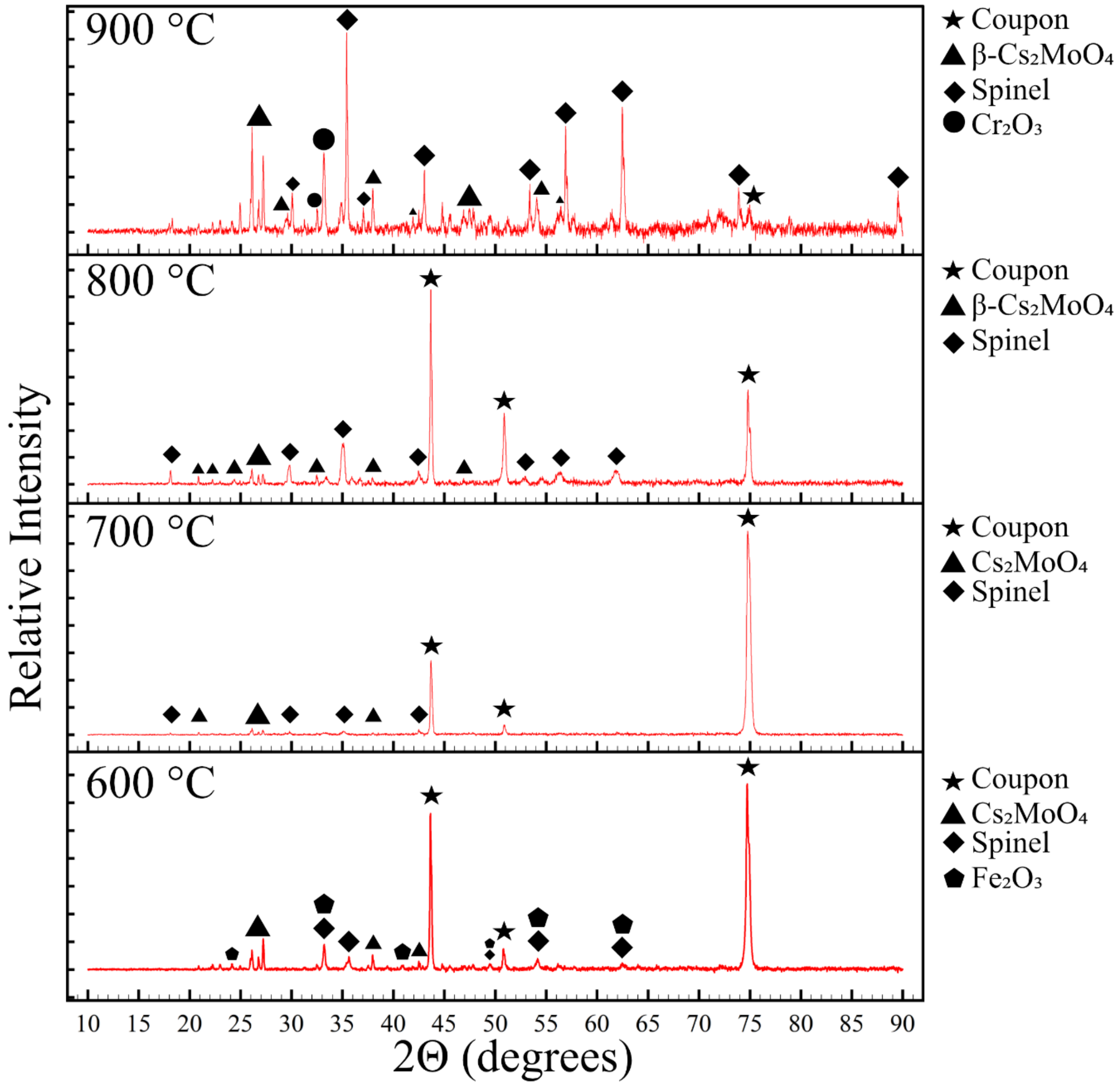

Figure 54: XRD patterns of all the confirmation experiments, exposures to Cs_2MoO_4 (600, 700, 800 and 900 °C; 168 h, under flowing Ar gas). "Coupon" peaks denote the unexposed steel.

6. Discussion

6.1. Thinning Effect in a Kinetic Context

The thickness loss reported in previous chapter 5.2 is severe enough to be a concern in case of an extended overheating situation during reactor operation. The collected temperature dependent material loss data will be discussed via a temperature-dependent Arrhenius approach. This interpretation is useful for the material assessment for both hosting tube and cladding tube, and therefore they were discussed separately.

6.1.1. Hosting Tube

The capsule integrity has been a crucial part of this study besides the cladding itself since it consists of alloy 316 which is quiet similar alloy to 15-15Ti. Due to molten Pb's vapor pressure at the LFR accident conditions, a leak is undesirable. The temperature limit of the exposure capsule was established to be between 900 °C and 1000 °C as the capsule fully dissolved and oxidized and swelled three times its size at 1000 °C, after 168 h exposure. The visual inspection of the capsules exposed at 600 °C - 900 °C does not indicate a structural failure, but the durability of exposures above 800 °C is questionable beyond 168 h. One week at such high accident temperature conditions, is hopefully not necessary to be considered for future reactors since nominal operational temperature of the molten Pb is of the order of ≈500 °C, 100 °C lower than the lowest experimental conditions of this study. Overheating countering measures would need to be active in a significantly shorter timeframe.

Main body of the capsule is composed of hosting tube and its respective capsules. Due to the thickness and complexity of the caps, hosting tube stands out as the weak link in the structural integrity of the capsule. In particular, the assembly point of Swagelok™ caps with the hosting tube would be a weakest point as it is under tension due to assembly of hosting tube and its respective caps. As such, additional attention was given to the investigation of the corrosion on the hosting tube, which is in contact with the same molten Pb as the cladding tube. Optical microscopy revealed that the hosting tubes had suffered a loss in their thicknesses, which was brought into kinetic context. In Table 4, the remaining tube thicknesses are listed, difference to original 2 cm. An Arrhenius approach was used, the rate constant "k" was hereby used in form of the thickness loss "X"; where "X" is the sum of alloy loss by delamination, dissolution and oxidation. The original Arrhenius Equation 8, where E_A is the activation energy, T is the temperature in Kelvin, R is the gas constant (8.314 $J/mol.K$), and A is the pre-exponential factor was thereby used instead as stated in Equation 9, treating the activation energy term as constant C. Ln X was plotted against $1/\mathrm{T}$ and trendlines were fitted to get fitting values (R^2) in Figure 55.

$$ln\,k \;=\; \frac{E_A}{R} \times \frac{1}{T} \;+\; ln\,A \tag{8}$$

$$ln\,X \;=\; C \times \frac{1}{T} \;+\; ln\,A \tag{9}$$

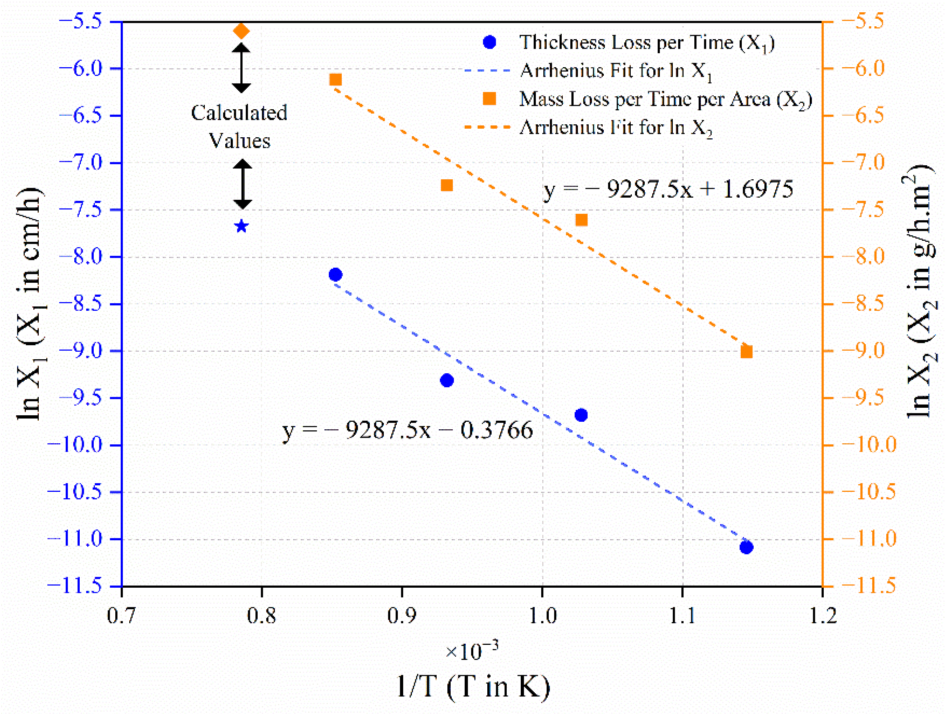

Figure 55: Thickness loss of hosting tube plotted and approximated via an Arrhenius fit.

Only 168 h exposures were used as data points. Left y-axis (blue) shows the logarithm of thickness loss *X* normalized against time, as opposed to 168 h, right y-axis (orange) instead shows the loss of material as normalized to per area and converted to grams per volume. Here the density was taken as given in Swagelok™ catalogs [74]. The plot shows that thickness loss on hosting tube is a good fit into Arrhenius equation to explain the relationship between temperature and material loss. This relationship can be used as an approximation into behavior of reactor vessels under elevated temperature conditions. Although the fittings are good, the calculated value (0.78 mm per 168 h) for 1000 °C (168 h) exposure does not explain the catastrophic failure observed in Figure 15. This inconsistency can be explained by the fact that our Arrhenius approach only accounts for the chemical reactions and does not consider mechanical stresses on the capsule. Especially, the assembly areas between hosting tube and its caps have been discussed before. An accelerated corrosion on this area can cause a failure earlier than the chemically predicted point, causing the whole capsule to fail catastrophically. These are in addition to the reported corrosion behavior of alloy 316 in high temperature air, which the hosting tube was subjected to from outside [80, 84].

Corrosion layers shown in Figure 16 is accounted for as-lost material in Arrhenius plots. For the transition from 600 °C to 700 °C, the internal oxidation disappeared, heterogeneous lamellar outer oxide scales have been observed. Similar to the total thickness loss, higher temperature exposures show a higher range of layer thickness, meaning a more heterogeneous behavior. In the case of reactor operation; this heterogenous behavior is expected to make in-pile measurements more difficult and possibly even unreliable in some cases. As such, the maximum and minimum values become more important. Internal oxidation increases again at temperatures ≥900 °C. The stability and diffusion kinetics of the oxide layers formed on the outer rim would directly affect these internal layers. The higher temperature allowed oxygen to diffuse faster, however the information about leached out metallic components requires an extremely difficult chemical analysis. The amount of Pb is much higher compared to the alloy components, which decreases the concentration drastically, making the analysis impractical.

6.1.2. Cladding Tube

The cladding tube thinning is a more complicated process compared to hosting tube thinning. Cladding tubes were exposed to a double atmosphere corrosion process where molten Pb and Cs_2MoO_4 were acting together from opposite sides of the cladding. Moreover, the corrosive nature of the reactants actually increased the thickness during the exposure at 600 °C for some locations. For consistency, the minimum thickness values were used instead in Table 10, and Equation 10 was formulated as a result. The exposure at 900 °C has a wide range of thickness loss (close to ±100 µm at some spots), bringing the corrosion process into a heterogeneous context. The severity of the thinning increased with temperature, as expected. Even though the difference between loss of thickness between 800 °C (168 h) and 1000 °C (52 h) are similar, 1000 °C has less discrepancy between its maximum and minimum value. This indicates that the heterogeneous thinning would be a result of long exposure. Using these datapoints with all their inherent insecurities, one arrives at a surprisingly well-fitting temperature at which total consumption of the cladding tube would be expected after 168 h (Table 10), with its visualization in Figure 56.

Table 10: Temperature dependent thickness loss of the cladding tube fitted into an Arrhenius plot. Underlined values were calculated from X = 450 µm value using Equation 10.

T in °C	T in K	1/T	X in µm	ln X
600	873.15	0.001145	14.6	2.681
700	973.15	0.001028	162.7	5.092
800	1073.15	0.000932	191.8	5.256
900	1173.15	0.000852	257.7	5.552
928.09	1201.24	0.000833	**450**	6.109

$$ln\,X = -9358.53 \times \frac{1}{T} + 13.9 \tag{10}$$

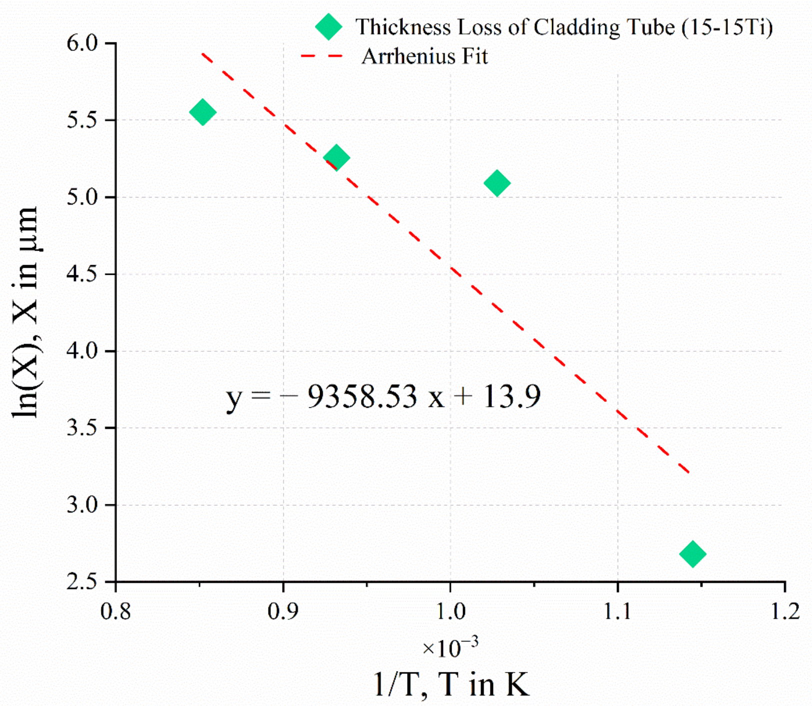

Figure 56: Visualization of Table 10. Thickness loss of cladding tube plotted and approximated with Arrhenius.

6.2. Temperature Dependency of Internal Oxidation by Molten Pb

On the Pb-side of the cladding tube, oxygen dissolved in molten Pb was the main oxidative species. The reaction between this oxygen and components of the 15-15Ti are the corrosion products of this process as well as alloy constituents dissolved into the melt. On all capsule exposures, an internal oxidation scale was observed. While most of the exposures (700, 800, 900, 1000 °C) showed similar processes, 600 °C was slightly different. The chemical composition and their reactions will be presented in this section. A broad comparison of the corrosion process can be seen on Table 11.

Table 11: An overview of the internal oxidation scales of all the capsule exposures.

Temperature (°C)	Double Scale	Double Scale Type	Inner Scale Thickness (µm)	Morphology	Metallic Inclusions
600	Yes	Outer/Inner	6-14	Continuous layer	Small grains
700	No	-	3-7	Intergranular	Grains; Ni-rich, Cr-deficient
800	No	-	22-32	Intergranular	Grains; Ni-rich, Cr-deficient
900	Yes	Both inner	64-87	Semi-continuous layers	Intragranular Oxidation
1000	Yes	Both inner	~130	Semi-continuous layers	Intragranular Oxidation

At 600 °C, an outer scale of Fe-oxide and inner spinel scale was seen. The spinel scale was also hosting intergranular oxidation paths (darker colored lines in Figure 21), and smaller grains of metallic inclusions. The processes at 700 °C and 800 °C were similar, the only important difference was the depth of the inner scales. On both, intergranular attacks were spinel phases, with metallic grains that were Ni enriched. At 900 °C and 1000 °C, the semi-continuous layers were similar in morphology to intergranular attacks (on 700 °C and 800 °C), with thicker oxide paths, which resembled a layer. The chemistry was similar to a spinel phase, and Ni enriched metallic inclusions were present. Here the metallic inclusions were much smaller; also, they hosted small "spots" of intragranular oxidation, most likely oxides of Cr, Mn, Ti and Si, as they would be the first to oxidize [67].

The biggest similarity between the different capsule exposures was the existence of the spinel phase. On all the exposures, an oxide mixture of Fe, Cr, Ni was found. According to the Ellingham diagram [67]; Cr(III)- and Ni(II)-oxides are the most stable oxides of the respective transition metals. While the Fe can be in Fe(II) or Fe(III) oxidation states; which is impossible to differentiate through EDX analysis alone. Here the interpretation of the results and the comparison to literature studies can help determine chemistry. As such, many studies have reported the existence of spinel scale on corrosion by heavy liquid metals on similar steels [6, 8, 85].

It is logical to start from elements with known states, Cr and Ni. The Ni signals on the EDX spectra taken from oxide layers were clear; qualification and quantification for Ni is consistent. However, the problem here lies in the thermodynamic stability of Ni metal. According to the Ellingham diagram [67], out of the main components of the 15-15Ti steel, Ni is the most noble alloy constituents, regardless of the temperature range in this study. Due to the absence of exact measurements of the oxygen content within the melt, Ni might very well remain in metallic form as also indicated by the nickel signal in Pb (Figure 25). The interaction volume of the EDX method could easily pick up background signals from metallic grains, partly due to the high accelerating voltage (25 kV) used in this study. As a result, Ni is unlikely to be a stable spinel constituent and leaches easily into the melt. This is further supported on the spinel of 900 °C and 1000 °C, in which Ni is disappearing; where simultaneously the oxide paths are getting much thicker, decreasing the probability of the interaction between the electron beam and metallic grains below. The solubility of metallic Ni is high [86], and the abundance of Ni enriched inclusions opens a path of molten Pb into the alloy. The Ni is dissolved in molten Pb, which is difficult to detect and quantify. If we assume that 20 mm long cladding tube (density of 7.704 g/cm^3 from Table 2) is all but dissolved in molten Pb, this will equal to 0.41 g of Ni in 76.26 g of molten Pb (average from Table 3). The ratio is 0.019 at.% of Ni in molten Pb, which is impossible to reliably detect in our setup.

The spinel compositions were calculated according to the known Fe-Cr spinel formula of $Fe(Fe_xCr_{1-x})_2O_4$, whose result can be seen on Table 12. The quantification of the whole spectra was used; and Fe to Cr ratios were calculated as they are, without removing Ni from the quantification. The "x" value was calculated from the spinel formula of $Fe(Fe_xCr_{1-x})_2O_4$. Apart from the 800 °C exposure, all the spinel phases were fitting into the $Fe(Fe_xCr_{1-x})_2O_4$

formula; however, the “x” value of less than zero suggests formation of Cr_2O_3 and Fe oxidizing into Fe_2O_3 state.

Table 12: Spinel compositions [$Fe(Fe_xCr_{1-x})_2O_4$] of internal oxidation scales seen on the Pb side of cladding tubes on capsule exposures.

Temperature	Fe to Cr Ratio	x
600	1.2 - 2.31	$0.32<x<0.55$
700	1.53 - 1.75	$0.41<x<0.45$
800	0.21 - 0.64	$-0.23<x<0.08$
900	0.57 - 2.38	$0.05<x<0.56$
1000	0.63 - 1.44	$0.08<x<0.38$

6.3. Delamination by Molten Pb

Delamination was recognized as the main process of thickness loss and the subsequent cladding breach. As such, the comparison of delamination between different temperatures is important to define. Moreover, the stagnant molten Pb allows for the exploration of delaminated layers. A flowing molten Pb system (e.g., an actual reactor) could easily erode the layers. Our setup’s disadvantage of non-flowing Pb can help us observe and identify the delamination phenomenon better for future studies.

On all the temperatures, delamination showed itself as repeating layers of Fe-oxide (with <10 at.% Cr) and Pb. The composition of Pb could not be measured consistently, as any element dissolved in molten Pb would be too little to quantify. The amount of Pb and the high solubility of alloy components (Cr, Ni) in molten Pb means that the measurements are not reliable [71, 86]. On the other hand, the Fe-oxide layers were more stable, which allowed for extensive analysis of the composition. The composition of Fe-oxide part of the delamination layers were consistent and similar on all the temperature. An oxygen percentage of 52-68 at.% was observed on all the exposure, along with 27-42 at.% Fe and 2-10 at.% Cr.

The morphology was not as consistent as the composition. While the repeating layers were present, their shape and thickness were different. Here, three different groups (in regard to temperature) of behavior were observed; 600 °C, 700/800 °C, 900/1000 °C.

The exposure at 600 °C represents the most likely scenario for an accident, as the expected temperature at hot zone of the ALFRED core is ~450 °C, which is only 150 °C lower than this exposure. Moreover, the advanced iterations of ALFRED aim to go up to ~600 °C in hot zones of the reactor core [3, 5]. The delamination at 600 °C was limited to drilled areas, which helps us glimpse into the initial stages of the process. It is known that outer growing oxides on a convex surface would be under tensile stress [41]. This can cause cracks as the oxide grows, which molten Pb wets as the stress on the oxide scale increases. On the free surfaces of the 600 °C capsule exposure, the stress on the oxide scales was not enough to cause a crack. However, the change between convex and concave oxide scale growth at the edges of drilled areas are high stress points, causing unevenly growing oxide scales. The free surfaces under tensile stress oxide scale growth meets the drilled areas, where oxide scales grow under compressive stress. As a consequence of two of these sides meeting, the edges of the drilled areas became the ingress point for entry of the molten Pb through cracks (Figure 57). The drilled areas are a good representation of pre-damage, which can be interpreted as in-situ mechanical damage to the cladding tube due to fretting, wear or irradiation. Considering the time scale at this exposure (168 h), the severity of 600 °C is not extremely alarming on the unaltered (e.g., uncoated, no pre-oxidation) cladding tube. Moreover, the native oxide scale that grew due to dissolved oxygen actually helps prevent more severe wetting by the molten Pb, but does not stop it completely [87]. The mechanisms of the delamination change drastically as the temperature increases.

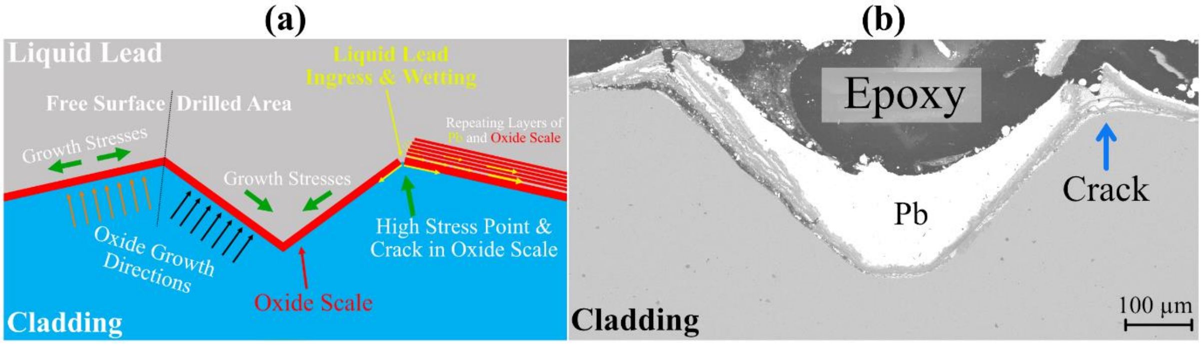

Figure 57: Delamination around drilled area in capsule exposure at 600 °C and 168 h, (a) schematic, (b) BSE image.

At 600 °C, the free surfaces were not delaminated, yet, as the oxide growth was not fast enough to cause a crack in the scales. However, at 700 °C and 800 °C, the scale was growing fast enough to cause cracks and the eventual wetting by molten Pb. This causes the oxide scale and the alloy to separate, forming repeating layers of delamination. On Figure 57-b, we can only observe 2-4 layers to separate, while 700 °C and 800 °C capsule exposures showed much severe repeating layers. Several SEM images have confirmed this (Figure 23, Figure 24, Figure 28, Figure 31). The delamination was much more severe on drilled areas, similar to the presence of delamination at 600 °C. This, again, relates to the growth stress concentration on the drilled areas and their edges. It is logical to assume that any pre-damaged location is prone to delamination if molten Pb can wet the surface.

The wetting behavior of molten Pb is what separates 900 °C and 1000 °C from the others, as the Pb morphology on the delaminated areas is drastically different than the lower temperature capsule exposures. Here, the formation of Pb droplets can be observed, as the molten Pb’s viscosity increases with the temperature. The solubility limits and the diffusion of Fe, Cr and Ni are also increasing, causing more heterogeneous delamination, where repeating layers are difficult to form. Figure 45 is good example of this where Fe-oxide (darker spots) are scattered as non-layered pieces in the Pb pool. These pieces are accompanied by droplets of Pb, neighboring empty places (which were later filled with epoxy) and growing as circular areas on the cross-section, instead of layers.

As presented before, the Fe-oxide components of delaminated layers were similar on all the capsule exposures. However, the initialization and maturing of delamination was difficult to establish. In the future, time-dependent exposures can help us explain the mechanism better. For the present data set, some rare occurrences of the process were found and investigated as points-of-interest. Firstly, the cross-section of capsule exposure at 800 °C (168 h, Figure 33) shows us the rapid decrease of Cr content of the delaminated layer. The delaminated layers further from the alloy were all much lower in Cr content (<10 at.%), while the delaminated layer close to the alloy showed a Cr content (~19 at.%) akin to the previously reported internal spinel scale. This suggests a delamination of the spinel scale (spinel was reported as the main internal oxidation mechanism). Figure 31-a and Figure 34 further supports this idea as the molten Pb was found inside the internal oxidation scale. Furthermore, Figure 31-a presents a layer of Pb mixed with the Cr-rich spinel layer, with the detached Fe-oxide layer above it. A detaching spinel scale was found on Figure 40, which is from a free surface of 900 °C (168 h) capsule exposure. Another rare occurrence was granted by the shorter exposure time (52 h) of 1000 °C capsule exposure, on Figure 46, where several spinel scale pieces were *caught* completely detached from their internal locations, with molten Pb residing in-between the spinel pieces and the cladding. The broken spinel pieces and the internal oxidation scale were in the same morphology and comparable spinel composition. The detached spinel pieces were more Fe-rich, while the internal spinel was in 1:1=Fe:Cr. The compositional difference (lower Cr %) can easily be accounted to the higher of solubility Cr in molten Pb, compared to Fe [70, 71]. Furthermore, the solubility of Ni is also high in molten Pb [86], which would explain the absence of the Ni-enriched metallic leftovers between the repeating delaminating layers.

6.4. Cs_2MoO_4 Corrosion

On the corrosion front of inner side of the cladding, Cs_2MoO_4 alone was the main corrosive specie. Even though breaching was observed on 900 °C and 1000 °C capsule exposures, the influence of breach was not observed on the free surfaces. Sometimes Pb peaks were seen but in no quantity that can change the corrosion process. While discussing the Cs_2MoO_4 corrosion, the results of the capsule exposures will be compared to confirmation exposures. Here the 1000 °C coupon exposure could not be completed and will be included in future studies of this thesis. On the other temperature levels, results and interpretation will be supported by the XRD analysis. Due to the geometry of the capsule exposure samples, XRD analysis could not be performed, but the confirmation exposures were instead used to gain the appropriate phases data. This will be especially important for the interpretation of spinel phases whose EDX data alone fails to explain the complete chemistry.

The scales at **600 °C** coupon confirmation and capsule were similar in phase but not in constituents. Capsule and coupon surfaces both showed a double scale (outer and inner oxidation). The capsule exposure had an outer scale with Fe:O=1:1 ratio, while the inner scale indicated a spinel structure. However, (similar to Pb corrosion) the spinel scale presented Ni enriched grains that were on the O-deficient locations, suggesting that the spinel is actually a Fe-Cr spinel phase. With no substance to dissolve the Ni, the grains have remained intact as a major part of the inner scale. The coupon exposure also showed a spinel structure but with much lower Cr (4 at.%) and Ni (4 at.%), along with 20.5 at.% Fe. While this did not particularly indicate a spinel structure, the XRD results revealed a spinel structure, which also correlates with the capsule exposure. The outer scale was in ~Fe:O=1:3 ratio. Fe_2O_3 peaks were seen mixed with the spinel peaks, identifying the Fe-oxide scale. Both inner scales were in similar thicknesses (3-8 µm for capsule and 1-8 µm for coupon).

The spinel scale observed on **700 °C** capsule was calculated for the $Fe(Fe_xCr_{1-x})_2O_4$ formula, where a $0.06<x<0.25$ range was found. On the other hand, the inner scale of coupon on the same temperature had the range of $0.05<x<0.84$. As “x” increases, the spinel phase is getting closer Fe_3O_4 compositions, meaning that more Fe(II) oxidized to Fe(III). Further from the alloy, Fe-rich spinel was more dominant; which aligns with the fact that Fe atoms are more mobile [88], while Cr atoms preferentially occupies inner scale’s cationic sites. A similar situation was seen on other scales where Fe-oxide based scales were growing out of the alloy. Thermodynamically, it is more difficult to oxidize Fe to (III) state. Even though the corrosive environments are the same, the convex shape of the cladding in capsule exposures limit the oxygen diffusion, making flat surface of the coupon a so-called “more oxidizing” environment. Eventually this could enable the transition to more Fe-rich spinel (Fe_3O_4).

800 °C capsule and coupon exposure were confirming each other on the inner scale. The capsule exhibited a Fe-rich spinel mixed with local Cr_2O_3 grains. The intergranular oxidation on capsule at 800 °C turned into a continuous scale on the coupon surface; mirroring the transition on 700 °C. On Figure 52-c (coupon, confirmation experiments), darker colored oxidation paths resembling an intergranular corrosion is seen. These paths grow further into the alloy than the inner scales. This is likely to be the initial stages of an inner scale growth; which needs time dependent studies to confirm as the beginning of the scale formation. A big difference between the capsule and coupon was the outer scale. Capsule exposure did not show an outer growing scale. On the other hand, an outer scale consisting of Fe-oxide with low amounts of Cr, Ni and Mn was observed on the coupon. Since the O availability was limited on the convex surface, the scale would have difficult time growing outside; not resulting in (locally) detaching scales seen on the coupon. This is further supported by the fact that continuous scales were lacking on the capsule exposure. The higher mobility of Fe atoms through diffusion is supported here again. Fe is helping grow an outer scale while inner scales are Cr-rich, and even Cr_2O_3 grains have formed on the deeper parts of the capsule exposure.

At **900 °C**, capsule and coupon confirmation exposures were similar in chemical behavior of the corrosion scales. Although, morphological differences remain. Starting on the inner scale, both showed a spinel formation. The chemical compositions of the spinel scales were also changing in the same way. On the capsule exposure, the spinel scales were found to be a Fe-Cr spinel with varying Fe and Cr rich locations. On the intergranular oxidation paths $Fe(Fe_xCr_{1-x})_2O_4$ ($0.27<x<0.32$) phase was seen and this phase was changed to a more Cr-rich continuous layer right next to the alloy ($-0.03<x<0.17$). The calculation of “x” value here suggests that this continuous layer is a mixture of either Cr_2O_3 and Fe-Cr spinel, or Cr_2O_3 and Fe_2O_3. Here the EDX data was insufficient to determine the mixture. However, the confirmation experiments and their XRD has enabled us to define this mixture as corundum and Fe-Cr spinel. The inner scale of coupon exposure has a similar chemical distribution; where corundum was detected closer to the alloy, and Fe-Cr spinel was detected closer to the surface. Even though the morphology was different, this phase distribution has confirmed the similarities in corrosion progression. The XRD spectrum confirmed both the spinel and corundum peaks. Since the unexposed coupon's XRD peaks were also seen on the XRD spectrum, the penetration depth of the X-rays used were confirmed to be deeper than the corrosion scales. The similarities in the inner scale were also observed on the outer scales. Here the outer scale of capsule exposure was detached (or *delaminated*) and the coupon was locally detached. Both the chemical compositions were Fe-oxide based. While the capsule suggests a FeO scale, the increased Mn content of coupon exposure (3.3 to 11 at.%) suggest that more O can turn the scale into a spinel phases. However, more detailed analysis of the XRD spectrum will be conducted to discover the possibility of a Fe-Mn spinel in the outer scale.

6.5. Breaching Occurrence and Progression

A breach in an in-situ location would result in radioactive material and coolant (molten Pb or LBE) to interact, which could then circulate through the whole reactor cooling system. On the capsule exposure of this study, pre-damaged drilled areas were used to estimate the possible breaching locations. As presented on the capsule results of 900 °C and 1000 °C (5.3.4.1 and 5.3.5.1, respectively), the estimated locations were indeed the breaching locations. On the other hand, lower temperature exposures (600, 700, 800 °C) did not exhibit signs of breach. This should not be interpreted as these temperatures are safe from a possible cladding failure. On the contrary, the progression of the corrosion indicates that 600 °C, 700 °C and 800 °C are likely to suffer from breaching around the drilled areas if the exposure time is increased. However, the reactor safety countermeasures would be active long before the 168 h mark is reached.

In this regard, the future work of this thesis could involve an extended exposure of 600 °C or 700 °C, as they are more likely to occur as a "temperature spike" during operation. The 600 °C capsule exposure showed delamination only around drilled areas, which significantly limits the contribution of delamination of the breaching. As argued in the discussion about molten Pb corrosion, delamination of the free surfaces increases the steel/molten Pb interaction significantly; paving the way for more Ni dissolution and alloy components being lost into the molten Pb. Figure 37 (900 °C breach) and Figure 44 (1000 °C breach) are good examples where the centers of the drilled areas were breached, but the extreme thinning of the cladding tube was actually extended to the free surfaces. The loss of wall thickness would directly increase the effects of creep on the cladding tube, increasing the likelihood of a breach.

The thickness losses for 168 h exposures were already established in Table 10, considering the loss of thickness on the free surfaces. When this loss value was applied to the leftover thickness after drilling (~175 µm), it can be seen that they correlate with the breach at 900 °C. On the Cs_2MoO_4 side, the corrosion scales did not change between drilled areas and free surfaces, but the behavior of corrosion scales on the molten Pb side has changed. Mostly, the double scales have turned into single scales, due to the lack of available metallic components to oxidize. This would have a direct impact on the interaction between molten Pb and Cs_2MoO_4. The oxidation state of Mo would stay at (VI), which would have a higher oxidative effect on the Pb. Unfortunately, the characterization of Pb/Cs_2MoO_4 interaction is not complete yet. As explained before, the differentiation of Pb and Mo with EDX is difficult. Moreover, the qualification of oxygen was found to be contradicting the contrast provided by the BSE detector. An extensive investigation of the interaction products is one of the future works of this thesis. These results can directly feed into the accident condition assessments of LFRs, as the chemistry of radioactive material release can be understood better.

6.6. Relating the Corrosion Process to Irradiation Effects

The described corrosion observations become even more pronounced when discussing them in correlation to reactor operation conditions and tensile load on the fuel pins. Over a fuel pin lifetime, the harsh chemical environment would have the addition of a 100 to 150 dpa (displacement per atom) irradiation field, mainly caused by neutron irradiation [40, 89]. Especially in this study, our assumption considers a high burn-up situation where the residence time for the cladding would be long and even nearing its end of service, reaching thereby also highest accumulation of JOG species caused by burn-up.

Therefore, we consider the performance of the original cladding material with unaffected microstructure and total 450 µm thickness too optimistic for an accident situation with high JOG impact. The more conservative approximation of a highly pre-damaged material simulated by the loss of two thirds of its thickness, such as shown for drilled area locations is a more appropriate accident approach.

Even though the irradiation effect on corrosion was not experimentally investigated here, the cladding corrosion must be discussed with relation to irradiation when a high burn-up situation is assumed. The comparison of JOG-side corrosion between Figure 29 and Figure 37, i.e., between corrosion features after exposure at 800 °C and 900 °C, shows a clear correlation of internal oxidation depth, reaching into the cladding perpendicular to the surface and temperature. Corrosion studies on irradiated austenitic materials have reported that the dislocation movement is enhanced as the dpa value increases [90]. High dpa values correlate with high burn-up, which is known to result in JOG formation.

7. Conclusions

Different aspects of the cladding corrosion process were investigated and discussed. The focus was dual atmosphere corrosion, which created multiple corrosion fronts, requiring separate considerations. The summary of all the experimental work, results and discussion can be seen below.

A new capsule design was completed to investigate the interaction between molten Pb, cladding (Sandvik 15-15Ti steel) and JOG phases at elevated temperature conditions ($T \geq 600$ °C). The cladding of choice, 15-15Ti, was subjected to dual-atmosphere corrosion by molten Pb on the outside and Cs_2MoO_4 on the inside of the cladding tube. The limits for this capsule for 168 h experiments were found to be lower than 1000 °C. At this temperature, exposures with limited time scales can still be employed.

A notch geometry on the outer side of cladding tubes facing the molten Pb was used to accelerate corrosion and induce controlled breaches. The notch geometry was designed to be reproduceable. On select locations, it lowered the tube wall thickness to one third prior to exposure. With the help of notches and correct parameter selection, a controlled cladding failure scenario was created, tested, and investigated.

At the free surfaces of the cladding tube (non-notched surface), it was observed that the thickness of the cladding tube had changed during exposure. Only 600 °C showed an increase of 2% wall thickness, while the other exposures showed a thinning effect. The thinning after exposure at 700 °C and 800 °C was not as severe as at the two highest temperatures. The cladding material thinning at 900 °C and 1000 °C was severe enough to cause breaches at the location of the notches. Thickness loss was also observed on the hosting of the reaction capsule. Since the hosting and cladding are close in elemental composition, the thickness loss here was also investigated. The thickness losses on both tubes were used to create a kinetic model using an Arrhenius approach.

At both interfaces (cladding/Pb and cladding/Cs_2MoO_4) oxide scales and internal oxidation have been observed. For molten Pb corrosion; 600 °C showed a double oxide layer corrosion process. This turned into an intergranular attack for 700 °C and 800 °C. At 900 °C and 1000 °C, the intergranular attack got more severe, and the scales were semi-continuous. A spinel type oxidation was seen, with metallic inclusions in between them. The spinels were Fe- or Cr-rich, while metallic inclusions were always Ni-enriched and Cr-deficient.

On the Pb-side of the cladding tube, delamination was observed. Oxide layers that grew on the tube were penetrated by molten Pb during exposures. The molten Pb got in between oxide layers and the alloy, effectively causing decohesion of the oxide layers and exposing a new surface. The process repeated itself to create a series of layers of Pb and Fe-oxides.

Ongoing delamination of oxide scales by molten Pb was causing a more rapid metal loss compared to oxidation occurring on the JOG side. Hence, delamination was determined as the main contributor of thickness loss.

For Cs_2MoO_4 corrosion, a similar grouping of temperatures (in relation to molten Pb) were seen. Spinel type attack became severe as the temperature increased. Localized delamination was also seen by Cs_2MoO_4 at 900 °C and 1000 °C. However, the intensity of the corrosion attack was less severe on Cs_2MoO_4 side.

In capsule exposure at 900 °C (168 h) and 1000 °C (52 h), cladding breaches were observed at notch location. At 900 °C, the breaches were mostly fractures, and no significant mass transfer was observed, except for one notch. At 1000 °C, all 4 notches suffered breaches that caused severe deformation and observable mass transfer. On both exposures, the oxidation scales were also changed due to mass loss of cladding.

Confirmation experiments were done to assist in phase analysis. Corroborative results were identified but detailed information is still to be obtained.

8. Future Work

The detailed assessment and extent of chemical corrosion still requires experimentation and careful interpretation of the current set of data.

- The reaction capsule is designed to host molten LBE as well as molten Pb. One of the first steps will be to investigate the corrosion process with molten LBE. Here the temperature will also be different as elevated temperatures in a LBEFR are different than a LFR.
- Delamination progress is an important aspect and time dependent studies could be done on select temperature levels. For example, 24-48-72-96-120 hour exposures could help us explain delamination in more detail.
- The cladding breaches need a more detailed SEM-EDX campaign. A series of analysis will be made, alternating accelerating voltage between 5 kV and 30 kV. The aim is to qualify oxygen (i.e., existence of oxide phases) and to quantify Pb and Mo. These analysis will be compared with the thermodynamic calculations of this specific system (Pb-Mo-O) done by our project partners to get a better understanding of Cs_2MoO_4/Pb interaction.
- The XRD spectra of confirmation experiments requires further interpretation. The existence of spinel scales was already confirmed. However, the type of spinels is still to be determined. The lattice parameters will help us determine whether the spinels are Fe- or Cr-rich.
- During confirmation experiments, it is expected that the Mo(VI) would be reduced, but the reduced products were not yet found in the XRD spectra. Here, again, more interpretation is needed.
- Cs_2MoO_4 was selected as the relevant JOG phase in this part of study. However, Cs_2MoO_4 is not the only important JOG phase. Particularly, I and Te containing JOG phases are of high interest due to their importance in radiological safety measures. Future work is foreseen with other JOG phases replacing Cs_2MoO_4 on the inner side of cladding tube. Possible candidates include but are not limited to CsI, Cs_2Te and Cs_2TeO_4.

Acknowledgements

Firstly, sincerest thanks to my supervisor Prof. Teodora Retegan Vollmer for giving me the opportunity to set foot into the field of nuclear science and continuing to be my lighthouse on this journey. Big thanks to my dear co-supervisor Dr. Christine Geers for her endless patience and guidance, both in lab and in chemistry. I enjoy the fact that you challenge me every time we sit down for a discussion; even though my face says otherwise.

Thanks to everyone in the KK/IMÅ for creating this great group, for countless climbing sessions, after-works and adventures around Gothenburg. Also big thanks to everyone in OOMK for welcoming me, and never allowing me to feel like an outsider. I would also like to thank Torbjörn Jönsson from our workshop, for his ingenuity and help while building the reaction capsules.

I thank Fredrik for turning a simple office into a place of laughter and scholarly discussions about our ever-changing society. Special thanks to Elena for being an amazing friend and always being by my side. I am grateful and lucky to have Sinem and Semih as friends who are just a call away.

I would like to thank the European Commission and Euratom for funding the PASCAL project (ID: 945341) and, by extension, my PhD. The cooperation of all the PASCAL participants is greatly appreciated.

And lastly, I cannot thank enough my furthest but biggest supporters, my parents Dr. Ufuk Tarı and Prof. Dr. Ergin Tarı. Thanks for helping me get here.

Doğaç Tarı

May 2024, Gothenburg

References

[1] D. Buckthorpe, "Introduction to Generation IV nuclear reactors," in *Structural Materials for Generation IV Nuclear Reactors*: Elsevier, 2017, pp. 1-22.

[2] J. E. Kelly, "Generation IV International Forum: A decade of progress through international cooperation," *Progress in Nuclear Energy,* vol. 77, pp. 240-246, Nov 2014, doi: 10.1016/j.pnucene.2014.02.010.

[3] A. Alemberti *et al.*, "ALFRED reactor coolant system design," *Nuclear Engineering and Design,* vol. 370, p. 110884, Dec 15 2020, doi: 10.1016/j.nucengdes.2020.110884.

[4] H. A. Abderrahim, P. Baeten, D. De Bruyn, and R. Fernandez, "MYRRHA - A multi-purpose fast spectrum research reactor," *Energy Conversion and Management,* vol. 63, pp. 4-10, Nov 2012, doi: 10.1016/j.enconman.2012.02.025.

[5] M. Tarantino *et al.*, "Overview on Lead-Cooled Fast Reactor Design and Related Technologies Development in ENEA," *Energies,* vol. 14, no. 16, p. 5157, 2021. [Online]. Available: https://www.mdpi.com/1996-1073/14/16/5157.

[6] C. Schroer and J. Konys, "Quantification of the Long-Term Performance of Steels T91 and 316L in Oxygen-Containing Flowing Lead-Bismuth Eutectic at 550°C," *Journal of Engineering for Gas Turbines and Power,* vol. 132, no. 8, 2010, doi: 10.1115/1.4000364.

[7] "PASCAL - A Euratom H2020 Research Project." https://www.pascalworkspace.eu/ (accessed March 15, 2023).

[8] L. Košek, L. Rozumová, A. Hojná, C. Aparicio, M. Vronka, and J. Vít, "Mechanism of localized corrosion issues of austenitic steels exposed to flowing lead with 10−7 wt.% oxygen at 480°C up to 16,000 h," *Journal of Nuclear Materials,* vol. 572, p. 154045, 2022, doi: 10.1016/j.jnucmat.2022.154045.

[9] J. Zhang, "A review of steel corrosion by liquid lead and lead–bismuth," *Corrosion Science,* vol. 51, no. 6, pp. 1207-1227, 2009, doi: 10.1016/j.corsci.2009.03.013.

[10] K. Samuelsson, J.-C. Dumas, B. Sundman, J. Lamontagne, and C. Guéneau, "Simulation of the chemical state of high burnup (U, Pu) O2 fuel in fast reactors based on thermodynamic calculations," *Journal of Nuclear Materials,* vol. 532, p. 151969, 2020.

[11] T. Uwaba *et al.*, "Irradiation performance of fast reactor MOX fuel pins with ferritic/martensitic cladding irradiated to high burnups," *Journal of nuclear materials,* vol. 412, no. 3, pp. 294-300, 2011.

[12] T. Uwaba, M. Ito, and K. Maeda, "Diametral strain of fast reactor MOX fuel pins with austenitic stainless steel cladding irradiated to high burnup," *Journal of Nuclear Materials,* vol. 416, no. 3, pp. 350-357, 2011, doi: 10.1016/j.jnucmat.2011.06.033.

[13] L. Martinelli, D. J. Young, S. Gossé, and S. Bosonnet, "Corrosion of 316L in liquid tellurium at 551°C," *Corrosion Science,* vol. 151, pp. 35-43, 2019/05/01/ 2019, doi: https://doi.org/10.1016/j.corsci.2019.02.001.

[14] M. Tourasse, M. Boidron, and B. Pasquet, "Fission product behaviour in phenix fuel pins at high burnup," *Journal of Nuclear Materials,* vol. 188, pp. 49-57, 1992, doi: 10.1016/0022-3115(92)90453-r.

[15] K. Sasaki, T. Tanigaki, M. Matsuyama, K. Fukumoto, and M. Uno, "Cesium corrosion process in Fe–Cr steel," *Journal of nuclear materials,* vol. 441, no. 1-3, pp. 315-323, 2013.

[16] S. Ukai, Y. Yamazaki, N. Oono, and S. Hayashi, "Corrosion behavior of 9CrODS steel by simulated fission product cesium and tellurium," *Journal of nuclear materials,* vol. 440, no. 1-3, pp. 39-45, 2013.

[17] T. Haste, F. Payot, and P. D. W. Bottomley, "Transport and deposition in the Phebus FP circuit," *Annals of Nuclear Energy,* vol. 61, pp. 102-121, Nov 2013, doi: 10.1016/j.anucene.2012.10.032.

[18] C. R. d. F. Azevedo, "Selection of fuel cladding material for nuclear fission reactors," *Engineering Failure Analysis,* vol. 18, no. 8, pp. 1943-1962, 2011.

[19] I. L. Pioro and G. H. Rodriguez, "Generation IV International Forum (GIF)," in *Handbook of Generation IV Nuclear Reactors*: Elsevier, 2023, pp. 111-132.

[20] C. Broeders, E. Kiefhaber, and H. Wiese, "Burning transuranium isotopes in thermal and fast reactors," *Nuclear Engineering and Design,* vol. 202, no. 2-3, pp. 157-172, 2000.

[21] "Periodic Table of Elements - Plutonium." Merck. https://pse.merckgroup.com/periodic-table/element/94 (accessed 2024.03.30).

[22] T. L. Authen, "Advances in the Application and Understanding of the CHALMEX FS-13 Process," Chalmers Tekniska Hogskola (Sweden), 2022.

[23] C. Poinssot *et al.*, "Assessment of the environmental footprint of nuclear energy systems. Comparison between closed and open fuel cycles," *Energy,* vol. 69, pp. 199-211, 2014.

[24] J. Serp, C. Poinssot, and S. Bourg, "Assessment of the Anticipated Environmental Footprint of Future Nuclear Energy Systems. Evidence of the Beneficial Effect of Extensive Recycling," *Energies*, vol. 10, no. 9, p. 1445, 2017. [Online]. Available: https://www.mdpi.com/1996-1073/10/9/1445.

[25] G. Choppin, J.-O. Liljenzin, J. Rydberg, and C. Ekberg, "The Nuclear Fuel Cycle," in *Radiochemistry and Nuclear Chemistry*, 2013, pp. 685-751.

[26] D. Tenchine, "Some thermal hydraulic challenges in sodium cooled fast reactors," *Nuclear Engineering and Design*, vol. 240, no. 5, pp. 1195-1217, 2010.

[27] C. Fazio *et al.*, *Handbook on lead-bismuth eutectic alloy and lead properties, materials compatibility, thermal-hydraulics and technologies*, 2015 ed. Organisation for Economic Co-Operation and Development, 2015.

[28] "NATRIUM™ Reactor and Integrated Energy Storage." TerraPower. https://www.terrapower.com/our-work/natriumpower/ (accessed 2024.03.20).

[29] "Fast Neutron Reactors." World Nuclear Association. https://world-nuclear.org/information-library/current-and-future-generation/fast-neutron-reactors.aspx (accessed 2024.03.19).

[30] C. F. Smith and L. Cinotti, "Lead-cooled Fast Reactors (LFRs)," in *Handbook of Generation IV Nuclear Reactors*: Elsevier, 2023, pp. 195-230.

[31] J. Davies and F. Ewart, "The chemical effects of composition changes in irradiated oxide fuel materials," *Journal of nuclear materials*, vol. 41, no. 2, pp. 143-155, 1971.

[32] Y. Guerin, "Fuel Performance of Fast Spectrum Oxide Fuel," in *Comprehensive Nuclear Materials*, 2012, pp. 547-578.

[33] L. C. Walters, "Nuclear fuel: design and fabrication," 2004, doi: 10.1016/B0-12-176480-X/00295-3.

[34] E. Epifano *et al.*, "Investigation of the Cs(2)(Mo,Te)O(4) Solid Solution and Implications on the Joint Oxyde-Gaine System in Fast Neutron Reactors," *Inorg Chem*, vol. 59, no. 14, pp. 10172-10184, Jul 20 2020, doi: 10.1021/acs.inorgchem.0c01307.

[35] F. Cappia *et al.*, "Electron microscopy characterization of fast reactor MOX Joint Oxyde-Gaine (JOG)," *Journal of Nuclear Materials*, vol. 531, p. 151964, 2020/04/01/ 2020, doi: https://doi.org/10.1016/j.jnucmat.2019.151964.

[36] R. J. Parrish, K. E. Wright, A. J. Winston, C. McKinney, J. M. Harp, and A. Aitkaliyeva, "Characterization of solid fission products in 13.7% FIMA MOX fuel using electron microscopy techniques," *Journal of Nuclear Materials*, vol. 524, pp. 67-79, 2019.

[37] M. Teague, B. Gorman, J. King, D. Porter, and S. Hayes, "Microstructural characterization of high burn-up mixed oxide fast reactor fuel," *Journal of nuclear materials*, vol. 441, no. 1-3, pp. 267-273, 2013.

[38] T. Allen, J. Busby, M. Meyer, and D. Petti, "Materials challenges for nuclear systems," *Materials today*, vol. 13, no. 12, pp. 14-23, 2010.

[39] R. B. Rebak, "Improved and Innovative Accident-Tolerant Nuclear Fuel Materials Considered for Retrofitting Light Water Reactors—A Review," *Corrosion and Materials Degradation*, vol. 4, no. 3, pp. 466-487, 2023. [Online]. Available: https://www.mdpi.com/2624-5558/4/3/24.

[40] J. L. Séran and M. Le Flem, "Irradiation-resistant austenitic steels as core materials for Generation IV nuclear reactors," in *Structural Materials for Generation IV Nuclear Reactors*, 2017, pp. 285-328.

[41] M. Schütze, D. R. Holmes, and R. B. Waterhouse, *Protective oxide scales and their breakdown*. John Wiley & Sons, 1997.

[42] J.-B. Vogt and I. Proriol Serre, "A Review of the Surface Modifications for Corrosion Mitigation of Steels in Lead and LBE," *Coatings*, vol. 11, no. 1, 2021, doi: 10.3390/coatings11010053.

[43] J. Henry and S. A. Maloy, "Irradiation-resistant ferritic and martensitic steels as core materials for Generation IV nuclear reactors," in *Structural Materials for Generation IV Nuclear Reactors*, 2017, pp. 329-355.

[44] J. S. Zhang and N. Li, "Review of the studies on fundamental issues in LBE corrosion," (in English), *Journal of Nuclear Materials*, vol. 373, no. 1-3, pp. 351-377, Feb 15 2008, doi: 10.1016/j.jnucmat.2007.06.019.

[45] S. Bassini, A. Antonelli, I. Di Piazza, and M. Tarantino, "Oxygen sensors for Heavy Liquid Metal coolants: Calibration and assessment of the minimum reading temperature," (in English), *Journal of Nuclear Materials*, vol. 486, pp. 197-205, Apr 2017, doi: 10.1016/j.jnucmat.2017.01.031.

[46] K. Rosseel, J. Lim, A. Marino, K. Gladinez, B. Gonzalez-Prieto, and A. Aerts, "HELIOS3: A stirred bubble column for oxygen addition or reduction in lead-bismuth eutectic," (in English), *Nuclear Engineering and Design*, vol. 365, p. 110716, Aug 15 2020, doi: 10.1016/j.nucengdes.2020.110716.

[47] M. Yurechko, C. Schroer, A. Skrypnik, O. Wedemeyer, V. Tsisar, and J. Konys, "Steel T91 subjected to static stress in lead-bismuth eutectic at 450-550 degrees C and low oxygen concentration," *Journal of Nuclear Materials*, vol. 512, pp. 423-439, Dec 15 2018, doi: 10.1016/j.jnucmat.2018.09.056.

[48] *Cr-Pb Binary Phase Diagram 0-100 at.% Pb: Datasheet from "PAULING FILE Multinaries Edition – 2022" in SpringerMaterials (https://materials.springer.com/isp/phase-diagram/docs/c_0900789)*, Springer-Verlag Berlin Heidelberg & Material Phases Data System (MPDS), Switzerland & National Institute for Materials Science (NIMS), Japan. [Online]. Available: https://materials.springer.com/isp/phase-diagram/docs/c_0900789

[49] C. Schroer, O. Wedemeyer, J. Novotny, A. Skrypnik, and J. Konys, "Selective leaching of nickel and chromium from Type 316 austenitic steel in oxygen-containing lead–bismuth eutectic (LBE)," *Corrosion Science,* vol. 84, pp. 113-124, 2014, doi: 10.1016/j.corsci.2014.03.016.

[50] E. Charalampopoulou *et al.*, "Early stages of dissolution corrosion in 316L and DIN 1.4970 austenitic stainless steels with and without anticorrosion coatings in static liquid lead-bismuth eutectic (LBE) at 500 C," *Materials Characterization,* vol. 178, p. 111234, 2021.

[51] L. Kosek, L. Rozumova, A. Hojna, and M. Pazderova, "Performance of 9Cr Ferritic-Martensitic Steels in Flowing Lead for 8000 h," *Journal of Nuclear Materials,* vol. 554, p. 153092, 2021.

[52] G. Müller, G. Schumacher, and F. Zimmermann, "Investigation on oxygen controlled liquid lead corrosion of surface treated steels," *Journal of Nuclear Materials,* vol. 278, no. 1, pp. 85-95, 2000, doi: 10.1016/s0022-3115(99)00211-1.

[53] A. Weisenburger *et al.*, "Long term corrosion on T91 and AISI1 316L steel in flowing lead alloy and corrosion protection barrier development: Experiments and models," *Journal of Nuclear Materials,* vol. 415, no. 3, pp. 260-269, Aug 31 2011, doi: 10.1016/j.jnucmat.2011.04.028.

[54] C. Fazio and F. Balbaud, "Corrosion phenomena induced by liquid metals in Generation IV reactors," in *Structural Materials for Generation IV Nuclear Reactors*, 2017, pp. 23-74.

[55] X. Gong, P. Marmy, and Y. Yin, "The role of oxide films in preventing liquid metal embrittlement of T91 steel exposed to liquid lead-bismuth eutectic," *Journal of Nuclear Materials,* vol. 509, pp. 401-407, 2018.

[56] K. Lambrinou, E. Charalampopoulou, T. Van der Donck, R. Delville, and N. Schryvers, "Dissolution corrosion of 316L austenitic stainless steels in contact with static liquid lead-bismuth eutectic (LBE) at 500 C (vol 490, pg 9, 2017)," *Journal of Nuclear Materials,* vol. 490, pp. 345-345, Jul 2017, doi: 10.1016/j.jnucmat.2017.04.025.

[57] A. Hojna, F. Di Gabriele, and J. Klecka, "Characteristics and Liquid Metal Embrittlement of the steel T91 in contact with Lead-Bismuth Eutectic," *Journal of Nuclear Materials*, vol. 472, pp. 163-170, Apr 15 2016, doi: 10.1016/j.jnucmat.2015.08.048.

[58] C. Schroer, Z. Voss, O. Wedemeyer, J. Novotny, and J. Konys, "Oxidation of steel T91 in flowing lead-bismuth eutectic (LBE) at 550 degrees C," *Journal of Nuclear Materials,* vol. 356, no. 1-3, pp. 189-197, Sep 15 2006, doi: 10.1016/j.jnucmat.2006.05.009.

[59] J. Klecka, F. Di Gabriele, and A. Hojna, "Mechanical properties of the steel T91 in contact with lead," *Nuclear Engineering and Design,* vol. 283, pp. 131-138, Mar 2015, doi: 10.1016/j.nucengdes.2014.10.004.

[60] G. Wallez, P. E. Raison, A. L. Smith, N. Clavier, and N. Dacheux, "High-temperature behavior of dicesium molybdate Cs2MoO4: Implications for fast neutron reactors," *Journal of Solid State Chemistry,* vol. 215, pp. 225-230, 2014, doi: 10.1016/j.jssc.2014.04.003.

[61] A. van Hattem *et al.*, "Structural Studies and Thermal Analysis in the Cs(2)MoO(4)-PbMoO(4) System with Elucidation of beta-Cs(2)Pb(MoO(4))(2)," *Inorg Chem,* vol. 62, no. 18, pp. 6981-6992, May 8 2023, doi: 10.1021/acs.inorgchem.3c00241.

[62] A. L. Smith, J. Vlieland, M. C. Pignié, M. Abbink, G. Mikaelian, and P. Benigni, "New insights into the Cs-Mo-O system: Experimental studies of the Cs2MoO4-MoO3 pseudo-binary system," *Thermochimica Acta,* vol. 696, 2021, doi: 10.1016/j.tca.2020.178825.

[63] A. L. Smith *et al.*, "Structural and thermodynamic study of dicesium molybdate Cs2Mo2O7: Implications for fast neutron reactors," *Journal of Solid State Chemistry,* vol. 253, pp. 89-102, 2017, doi: 10.1016/j.jssc.2017.05.032.

[64] J. Buckley *et al.*, "Fuel-Clad Interactions: Uranium Nitride and Uranium Dioxide with FeCrAl and Ti-Modified Stainless Steel," *Journal of Nuclear Materials,* p. 154903, 2024/01/06/ 2024, doi: https://doi.org/10.1016/j.jnucmat.2024.154903.

[65] D. Féron, "Overview of nuclear materials and nuclear corrosion science and engineering," in *Nuclear Corrosion Science and Engineering*: Elsevier, 2012, pp. 31-56.

[66] M. Terada, M. Saiki, I. Costa, and A. F. Padilha, "Microstructure and intergranular corrosion of the austenitic stainless steel 1.4970," *Journal of Nuclear Materials,* vol. 358, no. 1, pp. 40-46, 2006.

[67] H. J. Ellingham, "Reducibility of oxides and sulphides in metallurgical processes," *J. Soc. Chem. Ind,* vol. 63, no. 5, pp. 125-160, 1944.

[68] C. Wagner, "Beitrag zur theorie des anlaufvorgangs," *Zeitschrift für physikalische Chemie,* vol. 21, no. 1, pp. 25-41, 1933.

[69] G. Müller, A. Heinzel, G. Schumacher, and A. Weisenburger, "Control of oxygen concentration in liquid lead and lead–bismuth," *Journal of Nuclear Materials,* vol. 321, no. 2-3, pp. 256-262, 2003.

[70] *Fe-Pb Binary Phase Diagram 99.2-100 at.% Pb: Datasheet from "PAULING FILE Multinaries Edition – 2022" in SpringerMaterials (https://materials.springer.com/isp/phase-diagram/docs/c_0903876)*, Springer-Verlag Berlin Heidelberg & Material Phases Data System (MPDS), Switzerland & National Institute for Materials Science (NIMS), Japan. [Online]. Available: https://materials.springer.com/isp/phase-diagram/docs/c_0903876

[71] *Cr-Pb Binary Phase Diagram 0-100 at.% Pb: Datasheet from "PAULING FILE Multinaries Edition – 2022" in SpringerMaterials (https://materials.springer.com/isp/phase-diagram/docs/c_0906084)*, Springer-Verlag Berlin Heidelberg & Material Phases Data System (MPDS), Switzerland & National Institute for Materials Science (NIMS), Japan. [Online]. Available: https://materials.springer.com/isp/phase-diagram/docs/c_0906084

[72] *Ni-Pb Binary Phase Diagram 0-100 at.% Pb: Datasheet from "PAULING FILE Multinaries Edition – 2022" in SpringerMaterials (https://materials.springer.com/isp/phase-diagram/docs/c_0905795)*, Springer-Verlag Berlin Heidelberg & Material Phases Data System (MPDS), Switzerland & National Institute for Materials Science (NIMS), Japan. [Online]. Available: https://materials.springer.com/isp/phase-diagram/docs/c_0905795

[73] R. Delville, E. Stergar, and M. Verwerft, "Results of a New Production of Nuclear-Grade 1.4970 '15-15Ti'Stainless Steel Fuel Cladding Tubes for GEN IV Reactors," in *International Conference on Nuclear Engineering*, 2014, vol. 45899: American Society of Mechanical Engineers.

[74] "Stainless Steel Seamless Tubing and Tube Support Systems." Swagelok Company. https://www.swagelok.com/downloads/webcatalogs/en/ms-01-181.pdf (accessed June 19, 2023).

[75] D. Tarı, T. Retegan Vollmer, and C. Geers, "Reaction Capsule Design for Interaction of Heavy Liquid Metal Coolant, Fuel Cladding, and Simulated JOG Phase at Accident Conditions," *Journal of Nuclear Engineering,* vol. 5, no. 1, pp. 57-73, 2024. [Online]. Available: https://www.mdpi.com/2673-4362/5/1/5.

[76] J.-F. Vigier, K. Popa, V. Tyrpekl, S. Gardeur, D. Freis, and J. Somers, "Interaction study between MOX fuel and eutectic lead–bismuth coolant," *Journal of Nuclear Materials,* vol. 467, pp. 840-847, Dec 2015, doi: 10.1016/j.jnucmat.2015.10.056.

[77] L. B. N. Laboratory, *X-ray Data Booklet*. 2001.

[78] Y. N. Picard, "Scanning Electron Microscopy," in *Materials Characterization*, vol. 10: ASM International, 2019, p. 0.

[79] J. I. Goldstein *et al.*, "Electron Beam–Specimen Interactions," in *Scanning Electron Microscopy and X-ray Microanalysis: Third Edition*. Boston, MA: Springer US, 2003, pp. 61-98.

[80] X. Huang *et al.*, "Oxidation behavior of 316L austenitic stainless steel in high temperature air with long-term exposure," *Materials Research Express,* vol. 7, no. 6, p. 066517, Jun 2020, doi: 10.1088/2053-1591/ab96fa.

[81] R. Delville, E. Stergar, and M. Verwerft, "Results of a New Production of Nuclear-Grade 1.4970 '15-15Ti' Stainless Steel Fuel Cladding Tubes for GEN IV Reactors," in *22nd International Conference on Nuclear Engineering*, 2014, vol. Volume 1: Plant Operations, Maintenance, Engineering, Modifications, Life Cycle and Balance of Plant; Nuclear Fuel and Materials; Plant Systems, Structures and Components; Codes, Standards, Licensing and Regulatory Issues, doi: 10.1115/icone22-30781.

[82] *Cr-Fe-Ni Isothermal Section of Ternary Phase Diagram: Datasheet from "PAULING FILE Multinaries Edition – 2022" in SpringerMaterials (https://materials.springer.com/isp/phase-diagram/docs/c_0925651)*, Springer-Verlag Berlin Heidelberg & Material Phases Data System (MPDS), Switzerland & National Institute for Materials Science (NIMS), Japan. [Online]. Available: https://materials.springer.com/isp/phase-diagram/docs/c_0925651

[83] A. L. Smith *et al.*, "Thermodynamic modelling assessment of the ternary system Cs-Mo-O," *Calphad-Computer Coupling of Phase Diagrams and Thermochemistry,* vol. 75, Dec 2021, doi: 10.1016/j.calphad.2021.102350.

[84] W. J. Nowak, "Effect of Surface Roughness on Oxidation Resistance of Stainless Steel AISI 316Ti During Exposure at High Temperature," *Journal of Materials Engineering and Performance,* vol. 29, no. 12, pp. 8060-8069, Dec 2020, doi: 10.1007/s11665-020-05267-x.

[85] V. Tsisar, C. Schroer, O. Wedemeyer, A. Skrypnik, and J. Konys, "Corrosion behavior of austenitic steels 1.4970, 316L and 1.4571 in flowing LBE at 450 and 550 °C with 10−7mass% dissolved oxygen," *Journal of Nuclear Materials,* vol. 454, no. 1-3, pp. 332-342, 2014, doi: 10.1016/j.jnucmat.2014.08.024.

[86] *Ni-Pb Binary Phase Diagram 0-100 at.% Pb: Datasheet from "PAULING FILE Multinaries Edition – 2022" in SpringerMaterials (https://materials.springer.com/isp/phase-diagram/docs/c_0901767)*, Springer-Verlag Berlin Heidelberg & Material Phases Data System (MPDS), Switzerland & National

Institute for Materials Science (NIMS), Japan. [Online]. Available: https://materials.springer.com/isp/phase-diagram/docs/c_0901767

[87] X. Du *et al.*, "Influence of oxide scale on the wettability of LBE on T91 steel," *Fusion Engineering and Design*, vol. 125, pp. 378-383, 2017.

[88] B. Gillot, F. Jemmali, and A. Rousset, "Kinetics and mechanism of ferrous spinel oxidation studied by electrical conductivity and thermogravimetry," *Journal of materials science,* vol. 21, pp. 4436-4442, 1986.

[89] S. J. Zinkle and J. T. Busby, "Structural materials for fission & fusion energy," *Materials Today,* vol. 12, no. 11, pp. 12-19, 2009, doi: Doi 10.1016/S1369-7021(09)70294-9.

[90] E. Wakai *et al.*, "Irradiation damages of structural materials under different irradiation environments," *Journal of Nuclear Materials,* vol. 543, p. 152503, Jan 2021, doi: 10.1016/j.jnucmat.2020.152503.